Springer Proceedings in Physics 177

Paulo A. Ribeiro
Maria Raposo *Editors*

Photoptics 2014

Proceedings of the 2nd International Conference on Photonics, Optics and Laser Technology

Revised Selected Papers

Springer

Springer Proceedings in Physics

Volume 177

More information about this series at http://www.springer.com/series/361

Paulo A. Ribeiro · Maria Raposo
Editors

Photoptics 2014

Proceedings of the 2nd International Conference on Photonics, Optics and Laser Technology

Revised Selected Papers

Springer

Editors

Paulo A. Ribeiro	Maria Raposo
Faculdade de Ciências e Tecnologia	Faculdade de Ciências e Tecnologia
Universidade Nova de Lisboa	Universidade Nova de Lisboa
Caparica	Caparica
Portugal	Portugal

ISSN 0930-8989 ISSN 1867-4941 (electronic)
Springer Proceedings in Physics
ISBN 978-3-319-27319-8 ISBN 978-3-319-27321-1 (eBook)
DOI 10.1007/978-3-319-27321-1

Library of Congress Control Number: 2015958853

Printed on acid-free paper

This Springer imprint is published by SpringerNature
The registered company is Springer International Publishing AG Switzerland

Preface

This revised selected paper series Springer Proceedings in Physics Springer volume contains the papers of the 2nd International Conference on Photonics, Optics and Laser Technology (PHOTOPTICS) held in Lisbon, Portugal, sponsored by the Institute for Systems and Technologies of Information, Control and Communication (INSTICC). PHOTOPTICS 2014 was held in cooperation with the Sociedade Portuguesa de Física (SPF), Sociedade Portuguesa Interdisciplinar do Laser Medico (SPILM), Sociedade Portuguesa de Materiais (SPM), European Materials Research Society (E-MRS), Sociedade Anatómica Portuguesa (SAP), European Optical Society (EOS), European Physical Society (EPS), and Fundação para a Ciência e Tecnologia (FCT). It was held in collaboration with the Center of Physics and Technological Research (CEFITEC) and Faculdade de Ciências e Tecnologia-Universidade Nova de Lisboa (FCT-UNL) and technically sponsored by the Photonics21 platform. The Sociedad Española de Láser Médico Quirúrgico was an institutional partner, and the Science and Technology Events (SCITEVENTS) was the logistics partner. PHOTOPTICS 2014 featured five prominent keynote speakers which addressed cutting-edge topics worth to be emphasized. These were "Photon Wave Fronts—Frontiers in Photonics," by David Andrews, University of East Anglia, UK; "Multifunctional Nanoscale Oxide Conductors and Semiconductors," by Elvira Fortunato, CENIMAT/I3N/FCT/UNL, Portugal; "Circumventing the Diffraction Limit—Fluorescence Optical Microscopy at the Nanoscale," by Alberto Diaspro, Istituto Italiano di Tecnologia, Italy; "Dielectric Waveguide Amplifiers and Lasers," by Markus Pollnau, University of Twente, The Netherlands; and "Biomedical Cells as Bits—Diagnostics Inspired by Data Communication Techniques," by Bahram Jalali, UCLA, USA. High-quality presentations also took place in all main conference fields which covered theoretical, applied, and experimental issues. These include new materials for optics and photonics; optical fibers spontaneous emission and optical fiber nanoprobes; new optical devices, systems, and procedures; nonlinearity and distortion studies in data transmission; optical signal optimization; filtering and precise phase measurements; interferometry applied to holographic encryption; high power lasers and quantum dot lasers; and theoretical models such as universal polariton modeling of damage induced by laser, Monte Carlo inverse modeling toward optical tissue properties evaluation, charge carries dynamics in diamond, propagation and amplification of short and intense pulses in plasma channels, direct capture in quantum dot lasers under optical feedback, and performance evaluation of amplified spontaneous emission noise-impaired direct detection in optical systems. The conference and the papers in this Springer Proceedings in Physics volume reflect a growing effort to increase the dissemination of new results among researchers and professionals related to Photonics, Optics and Laser Technology. The PHOTOPTICS 2014 has built on successes of the previous conference that took place at Barcelona, Spain.

PHOTOPTICS 2014 received 82 submissions, of which 11 % were presented as full papers. Additionally, 16 % were short oral presentations and 16 % presented as posters. To evaluate each submission, a double-blind paper evaluation method was used: each paper was reviewed by at least two experts from the International Program Committee in a double-blind review process, and most papers had three reviews or more.

The best papers of the conference were invited, after corrections and extensions, to appear in this post-conference Springer Proceedings in Physics book.

Paulo A. Ribeiro
Maria Raposo

Organization

Conference Chair

Paulo A. Ribeiro, CEFITEC/FCT/UNL, Portugal

Program Chair

Maria Raposo, CEFITEC/FCT/UNL, Portugal

Organizing Committee

Helder Coelhas, INSTICC, Portugal
Ana Guerreiro, INSTICC, Portugal
André Lista, INSTICC, Portugal
Andreia Moita, INSTICC, Portugal
Raquel Pedrosa, INSTICC, Portugal
Vitor Pedrosa, INSTICC, Portugal
Cláudia Pinto, INSTICC, Portugal
Susana Ribeiro, INSTICC, Portugal
Mara Silva, INSTICC, Portugal
José Varela, INSTICC, Portugal
Pedro Varela, INSTICC, Portugal

Program Committee

Manuel Abreu, Laboratory of Optics, Lasers and Systems (LOLS), Faculdade de Ciências da Universidade de Lisboa, Portugal
Hugo Águas, CENIMAT:I3N, Portugal
Gandhi Alagappan, Institute of High Performance Computing, Agency for Science, Technology and Research (A-STAR), Singapore
Cid Bartolomeu De Araújo, Departamento de Física, Universidade Federal de Pernambuco, Brazil
Andrea Armani, University of Southern California, USA
Jhon Fredy Martinez Avila, Universidade Federal de Sergipe, Brazil

Morten Bache, Technical University of Denmark, Denmark
Carlos Baleizão, Centro de Química-Física Molecular, Instituto Superior Técnico, Portugal
Pedro Barquinha, Departamento de Ciência dos Materiais, Faculdade de Ciências e Tecnologia, Universidade Nova de Lisboa, Portugal
Almut Beige, University of Leeds, UK
Antonella Bogoni, CNIT, Italy
Ekaterina Borisova, Institute of Electronics—Bulgarian Academy of Sciences, Bulgaria
Remy Braive, Laboratory for Photonics and Nanostructures/CNRS, France
Gilberto Brambilla, Optoelectronics Research Centre, University of Southampton, UK
Valeriy Brazhnyy, Centro de Física da Universidade do Porto, Portugal
Tom Brown, University of St Andrews, UK
Alexandre Cabral, Laboratory of Optics, Lasers and Systems (LOLS), Faculdade de Ciências da Universidade de Lisboa, Portugal
Enrique Castro Camus, Centro de Investigaciones en Optica A.C., Mexico
John Canning, University of Sydney, Australia
Adolfo Cartaxo, Instituto de Telecomunicações, Instituto Superior Técnico, Portugal
Calvin C.K. Chan, The Chinese University of Hong Kong, Hong Kong
Yu Chen, University of Maryland at College Park, USA
João Coelho, Faculdade de Ciências da Universidade de Lisboa, Portugal
Olinda Conde, University of Lisbon, Laser Surface Processing Laboratory, Portugal
François Courvoisier, FEMTO-ST CNRS, Université de Franche-Comté, France
Helder Crespo, FCUP, Portugal
Daoxin Dai, Zhejiang University, China
Yujie J. Ding, Lehigh University, USA
Alexandre Dmitriev, Chalmers University of Technology, Sweden
Jonathan Doylend, Intel Corporation, USA
Robert Ferguson, National Physical Laboratory, UK
Mário F.S. Ferreira, University of Aveiro, Portugal
Orlando Frazão, INESC Porto, Portugal
James G. Fujimoto, Massachusetts Institute of Technology, USA
Marco Gianinetto, Politecnico di Milano, Italy
Adam Gibson, University College London, UK
John Girkin, Department of Physics, Biophysical Sciences Institute, Durham University, UK
Norbert Grote, Fraunhofer Heinrich Hertz Institute, Germany
Bob Guenther, Duke University, USA
Vasco Guerra, Departamento de Física Instituto Superior Técnico, Portugal
David J. Hagan, University of Central Florida, USA
José Manuel Henriques, SPILM—Portuguese Medical Laser Society, Portugal
Peter Horak, University of Southampton, UK
Weisheng Hu, Shanghai Jiao Tong University, China

Bormin Huang, University of Wisconsin-Madison, USA
Nicolae Hurduc, Gheorghe Asachi Technical University of Iasi, Romania
Phil Jones, Optical Tweezers Group, University College London, UK
José Joatan Rodrigues Jr., Universidade Federal de Sergipe, Brazil
Magnus Karlsson, Chalmers University of Technology, Sweden
Young-Jin Kim, Korea Advanced Institute of Science and Technology, Republic of Korea
Stefan Kirstein, Humboldt-Universitaet zu Berlin, Germany
Cristina Kurachi, Instituto de Física de São Carlos, Universidade de São Paulo, Brazil
Jesper Lægsgaard, Technical University of Denmark, Denmark
Wei Lee, National Chiao Tung University, Taiwan
Ofer Levi, University of Toronto, Canada
Dawei Liang, FCT/UNL, Portugal
Milton S.F. Lima, Instituto de Estudos Avancados, Brazil
Yi-Hsin Lin, National Chiao Tung University, Taiwan
Zhaowei Liu, University of California—San Diego, USA
Robert Loce, Xerox Corporation, USA
Carmen Mas Machuca, Technische Universität München, Germany
Hervé Maillotte, Institut FEMTO-ST, France
Luis Gustavo Marcassa, Instituto de Física de São Carlos, Universidade de São Paulo, Brazil
Alexandre Marletta, Universidade Federal de Uberlândia, Brazil
Manuel Marques, FCUP, Portugal
Paulo Marques, FCUP/INESC Porto, Portugal
Nicolas Martin, FEMTO-ST, France
Francisco Medina, University of Seville, Spain
Andrea Melloni, Politecnico di Milano, Italy
Paulo Miranda, Instituto de Física de São Carlos, Universidade de São Paulo, Brazil
Mark Mirotznik, University of Delaware, USA
Andrew Moore, Heriot-Watt University, UK
Bill Munro, NTT Basic Res. Labs, Japan
Phyllis R. Nelson, California State Polytechnic University Pomona, USA
André Nicolet, Institut Fresnel, AIX Marseillle Université, CNRS, France
Ana Flávia Nogueira, Laboratório de Nanotecnologia e Energia Solar, Brazil
Eduardo Nunes-Pereira, University of Minho, Portugal
Pál Ormos, Biological Research Centre, Hungarian Academy of Sciences, Hungary
Jisha Chandroth Pannian, Centro de Física da Universidade do Porto, Portugal
Yong Keun Park, Department of Physics, KAIST, Republic of Korea
Lorenzo Pavesi, University of Trento, Italy
Johannes Pedarnig, Johannes Kepler University Linz, Austria
Luís Pereira, Faculdade de Ciências e Tecnologia, Universidade Nova de Lisboa, Portugal
Ricardo Torres La Porte, Centro de Laseres Pulsados, Spain

Fabien Quere, CEA—Commissariat à l’énergie atomique et aux énergies renouvelables, France
Roberta Ramponi, Politecnico di Milano, Campus Milano Leonardo, Italy
Maria Raposo, CEFITEC/FCT/UNL, Portugal
José Manuel Rebordão, FCUL, Portugal
Paulo A. Ribeiro, CEFITEC/FCT/UNL, Portugal
Alessandro Rizzi, Università di Milano, Italy
Luis Roso, Centro de Laseres Pulsados, Spain
Isabelle Sagnes, Laboratory for Photonics and Nanostructures/CNRS, France
Bouchta Sahraoui, University of Angers, UFR of Sciences, France
José Manuel Sánchez-Pena, Universidad Carlos III de Madrid, Spain
Elisa Sani, INO—Istituto Nazionale di Ottica, CNR, Italy, Italy
Luís Santos, Instituto Superior Técnico, Portugal
Manuel Pereira dos Santos, Centro de Física e Investigação Tecnológica, Faculdade de Ciências e Tecnologia, Universidade Nova de Lisboa, Portugal
David Schmool, Faculdade de Ciências da Universidade do Porto, Portugal
Carlos Serpa, Universidade de Coimbra, Portugal
Alan Shore, Bangor University, UK
Ronaldo Silva, Federal University of Sergipe, Brazil
Arun K. Somani, Iowa State University, USA
Feng Song, Nankai University, China
Iuliana Stoica, “Petru Poni” Institute of Macromolecular Chemistry, Romania
Xiao Wei Sun, South University of Science and Technology of China, China
João Manuel R.S. Tavares, FEUP—Faculdade de Engenharia da Universidade do Porto, Portugal
Roy Taylor, Imperial College London, UK
Ladislav Tichy, IMC ASCR, Czech Republic
Valery V. Tuchin, Saratov State University, Russian Federation
Eszter Udvary, Optical and Microwave Telecommunication laboratory, Budapest University of Technology and Economics (BME), Hungary
Naoya Wada, National Institute of Information and Communications Technology, Japan
Wanjun Wang, Louisiana State University, USA
Gregor Weihs, University of Innsbruck, Austria
Elaine Wong, University of Melbourne, Australia
Lech Wosinski, KTH—Royal Institute of Technology, Sweden
Shinji Yamashita, University of Tokyo, Japan
Anna Zawadzka, Institute of Physics, Faculty of Physics, Astronomy and Informatics Nicolaus Copernicus University, Poland
Chao Zhou, Lehigh University, USA
Lei Zhou, Fudan University, China

Auxiliary Reviewer

Mauricio Rico, Centro de láseres de Pulsados (CLPU), Spain

Invited Speakers

David Andrews, University of East Anglia, UK
Elvira Fortunato, CENIMAT/I3N/FCT/UNL, Portugal
Alberto Diaspro, Italian Institute of Technology, Italy
Markus Pollnau, University of Twente, The Netherlands
Bahram Jalali, UCLA, USA

Contents

Part I Optics

Part II Photonics

Part III Lasers

Contributors

Tiago M.F. Alves Department of Electrical and Computer Engineering, Instituto Superior Técnico, Optical Communications and Photonics Group, Instituto de Telecomunicações, Universidade de Lisboa, Lisbon, Portugal

Tibor Berceli Department of Broadband Infocommunications and Electromagnetic Theory, Budapest University of Technology and Economics, Budapest, Hungary

A.V. Bogatskaya Department of Physics, Lomonosov Moscow State University, Moscow, Russia; D.V. Skobeltsyn Institute of Nuclear Physics, Lomonosov Moscow State University, Moscow, Russia; P.N. Lebedev Physical Institute, RAS, Moscow, Russia

Luís G.C. Cancela Instituto de Telecomunicações, Lisbon, Portugal; Department of Information Science and Technology, Instituto Universitário de Lisboa (ISCTE-IUL), Lisbon, Portugal

Adolfo V.T. Cartaxo Department of Electrical and Computer Engineering, Instituto Superior Técnico, Optical Communications and Photonics Group, Instituto de Telecomunicações, Universidade de Lisboa, Lisbon, Portugal

Shenq-Tsong Chang National Applied Research Laboratories, Instrument Technology Research Center, Hsin-Chu, Taiwan

Pedro E.D. Cruz Department of Electrical and Computer Engineering, Instituto Superior Técnico, Optical Communications and Photonics Group, Instituto de Telecomunicações, Universidade de Lisboa, Lisbon, Portugal

Sttela D.V.F. da Rosa Brazilian Agricultural Research Corporation, Embrapa/Coffee Unit, Brasilia, DF, Brazil

Gilberto F. De Sá Departamento de Química Fundamental, Universidade Federal de Pernambuco, Recife, PE, Brazil

Yaping Dai Shanghai Institute of Laser Plasma, Jiading, Shanghai, China

Geert Deconinck ESAT/ELECTA, KU Leuven, Leuven, Belgium

Guy Durinck Light & Lighting Laboratory, KU Leuven, Ghent, Belgium

Gábor Fekete Department of Broadband Infocommunications and Electromagnetic Theory, Budapest University of Technology and Economics, Budapest, Hungary

Masayuki Fujita Institute for Laser Technology, Suita, Osaka, Japan; Institute of Laser Engineering, Osaka University, Suita, Osaka, Japan

Cristiano M. Gallep Applied Photonics Lab, School of Technology, University of Campinas, Limeira, SP, Brazil

Won-Taek Han School of Information and Communications/Department of Physics and Photon Science, Gwangju Institute of Science and Technology, Buk-gu, Gwangju, Republic of Korea

Peter Hanselaer Light & Lighting Laboratory, KU Leuven, Ghent, Belgium

Johan Hofkens Department of Chemistry, KU Leuven, Leuven, Belgium

Yen-Ru Huang Department of Electrical Engineering, Graduate Institute of Photonics and Optoelectronics, National Taiwan University, Taipei, Taiwan; Graduate Institute of Communication Engineering, National Taiwan University, Taipei, Taiwan

Yasukazu Izawa Institute for Laser Technology, Suita, Osaka, Japan; Institute of Laser Engineering, Osaka University, Suita, Osaka, Japan

Seongmook Jeong School of Information and Communications/Department of Physics and Photon Science, Gwangju Institute of Science and Technology, Buk-gu, Gwangju, Republic of Korea

Ernesto Jimenez-Villar Departamento de Química Fundamental, Universidade Federal de Pernambuco, Recife, PE, Brazil; Instituto de Ciencia Molecular, Universitat de València, Paterna, Valencia, Spain

Seongmin Ju School of Information and Communications/Department of Physics and Photon Science, Gwangju Institute of Science and Technology, Buk-gu, Gwangju, Republic of Korea

Hyun-Kyu Jung Nuclear Convergence Technology Development Department, Korea Atomic Energy Research Institute, Yuseong-gu, Daejeon, Republic of Korea

Makoto Kasaoka Kanden Engineering Corporation, Minato-ku, Osaka, Japan

Jong-Yeol Kim Nuclear Convergence Technology Development Department, Korea Atomic Energy Research Institute, Yuseong-gu, Daejeon, Republic of Korea

Youngwoong Kim School of Information and Communications/Department of Physics and Photon Science, Gwangju Institute of Science and Technology, Buk-gu, Gwangju, Republic of Korea

Nam-Ho Lee Nuclear Convergence Technology Development Department, Korea Atomic Energy Research Institute, Yuseong-gu, Daejeon, Republic of Korea

San-Liang Lee Department of Electronic Engineering, National Taiwan University of Science and Technology, Taipei, Taiwan

Sven Leyre Light & Lighting Laboratory, KU Leuven, Ghent, Belgium

Zhaoyang Li Shanghai Institute of Laser Plasma, Jiading, Shanghai, China

Wei-Cheng Lin National Applied Research Laboratories, Instrument Technology Research Center, Hsin-Chu, Taiwan

Mirian P. Maluf Brazilian Agricultural Research Corporation, Embrapa/Coffee Unit, Brasilia, DF, Brazil

Valdeci Mestre CCEA, Universidade Estadual da Paraíba, Patos, PB, Brazil

Yoshitomo Nagano Kanden Engineering Corporation, Minato-ku, Osaka, Japan

Lilian Padilha Brazilian Agricultural Research Corporation, Embrapa/Coffee Unit, Brasilia, DF, Brazil

João J.O. Pires Instituto de Telecomunicações, Lisbon, Portugal; Department of Electrical and Computer Engineering, Instituto Superior Técnico, Lisbon, Portugal

A.M. Popov Department of Physics, Lomonosov Moscow State University, Moscow, Russia; D.V. Skobeltsyn Institute of Nuclear Physics, Lomonosov Moscow State University, Moscow, Russia; P.N. Lebedev Physical Institute, RAS, Moscow, Russia

João L. Rebola Instituto de Telecomunicações, Lisbon, Portugal; Department of Information Science and Technology, Instituto Universitário de Lisboa (ISCTE-IUL), Lisbon, Portugal

Toshihiro Somekawa Institute for Laser Technology, Suita, Osaka, Japan

Hen-Wai Tsao Department of Electrical Engineering, Graduate Institute of Photonics and Optoelectronics, National Taiwan University, Taipei, Taiwan; Graduate Institute of Communication Engineering, National Taiwan University, Taipei, Taiwan

Makoto Tsubokawa Waseda University, Kitakyusyu, Japan

E.A. Volkova D.V. Skobeltsyn Institute of Nuclear Physics, Lomonosov Moscow State University, Moscow, Russia

Tao Wang Shanghai Institute of Laser Plasma, Jiading, Shanghai, China

Martijn Withouck Light & Lighting Laboratory, KU Leuven, Ghent, Belgium

Jingshown Wu Department of Electrical Engineering, Graduate Institute of Photonics and Optoelectronics, National Taiwan University, Taipei, Taiwan; Graduate Institute of Communication Engineering, National Taiwan University, Taipei, Taiwan

Guang Xu Shanghai Institute of Optics and Fine Mechanics, Jiading, Shanghai, China

Part I
Optics

Chapter 1
Distortions and Their Effect on Signal Transmission in Coherent-OFDM Systems

Gábor Fekete and Tibor Berceli

Abstract The next generation optical systems will use OFDM modulation. It requires highly linear transmitter or the signal will be distorted. However, the commonly used optical Mach-Zehnder Modulator characteristic is not linear. In this paper we examined the modulator caused signal distortions and its possible driving methods to minimize the signal degradation. We will show that the distortions can be eliminated with proper driving technique and it is not necessary to use a dedicate hardware to compensate the effect of nonlinearity. The dispersions and the nonlinearities of the optical fibers (e.g. polarization mode dispersion, four wave mixing) are investigated too. A simple method is presented which can reduce the polarization mode dispersion. The transmitter and the channel caused distortions are compared to each other. The results show that some distortions from the transmitter and some from the channel are not only in the same range, but their effect to the signal is also similar.

1.1 Introduction

The demand for faster and larger amount data transmission is continuously increasing, therefore the same higher modulation formats have been started to use in optics as ones are used in the electrical domain. The next generation optical systems will use the Orthogonal Frequency Division Multiplexing (OFDM) modulation [1–3], because of its flexibility. The main benefit of the OFDM is the easy distortions compensation methods. Many compensation techniques use post-compensation techniques, which is

---

G. Fekete (✉) · T. Berceli
Department of Broadband Infocommunications and Electromagnetic Theory, Budapest University of Technology and Economics, Egry József utca 18, Budapest 1111, Hungary
e-mail: gfekete@hvt.bme.hu; gabor.fekete@omt-lab.hu

T. Berceli
e-mail: berceli@mht.bme.hu

P.A. Ribeiro and M. Raposo (eds.), *Photoptics 2014*,
Springer Proceedings in Physics 177, DOI 10.1007/978-3-319-27321-1_1

done by DSP (Digital Signal Processing). It is a more compact methode than using a long dispersion compensation fiber. OFDM is a big success in the electrical domain because it is a spectrally efficient modulation form. This spectral efficiency will be also important in the future optical networks. However OFDM has drawbacks such as complex detection method, high sensitivity to nonlinearity and high PAPR (Peak to Average Power Ratio). OFDM transmitter has to be linear to avoid signal distortion, however, the commonly used optical Mach-Zehnder Modulator (MZM) is highly nonlinear [2]. Therefore, it is important to know the MZM caused distortion, then it can be compensated without a DSP. At the transmitter side not only the modulator but the laser noise also degrades the quality of transmission. In this paper these two distortion effects are examined in Sects. 1.3.1 and 1.3.2.

The distortions can come from the transmission channel too. The chromatic dispersion (CD) and the polarization mode dispersion (PMD) are the major limiting factors in the channel. CD is compensated traditionally by Dispersion Compensation Fiber (DCF) but it is not the same for each wavelength and always remains a small CD on the signal. OFDM modulation provides the facility to use DSP for CD compensation, if its effects are well known. The PMD comes from the different propagation speed of the two polarization planes in a fiber [4–6]. PMD is the mean value of the differential group delay of the polarization planes. To develop a PMD compensation method is not easy, because of the statistical nature of the PMD. For a long time its effect was neglected because other nonlinearities (e.g. chromatic dispersion) had much stronger distortion. The older optical fibers have 2 ps/km$^{1/2}$ PMD coefficient while the new fibers PMD coefficient is only 0.1 ps/km$^{1/2}$ [4]. That is due to the new manufacturing technologies which reduce the value of the PMD coefficient. PMD distortion could be decreased by replacing the old fibers having a higher PMD coefficient. However, that method cannot be applied, because it would cost thousand millions of US dollars. Another method would be the selection of the modulation format, which is less sensitive for the PMD or provides easy post-compensation method. OFDM modulation has this benefit because the DSP, which is used for CD compensation, can be used to eliminate the effect of PMD too. CD and PMD effects to the transmission are investigated in Sect. 1.3.3. The fiber nonlinearity caused signal distortion has to be taken into account, if the power density in the fiber is higher than 1 W. High PAPR can cause this kind of distortion. However, the MZM also will distort the signal if the PAPR is too high. VPI TransmissionMaker (VPI) software was used for our simulation examination. We investigate whether the modulator or the fiber caused distortion effect has stronger influence on the transmitted signal or they are in the same range.

1.2 Principle of OFDM

OFDM is a special class of multi carrier modulation. Using more than one carrier frequency for data transmission was the idea [7], [3]. The carrier frequencies are orthogonal to each other because it guarantees the smallest bandwidth for the modulated signal. The mathematical form of the OFDM signal is the following [1]:

$$s(t) = \sum_{i=-\infty}^{\infty} \sum_{k=1}^{N_{sc}} c_{ki} s_k(t - iT_s), \quad s_k(t) = \exp(j2\pi f_k t) \quad \text{if } 0 \le t \le T_s \tag{1.1}$$

N_{sc} is the number of the subcarriers, c_{ki} is the ith information symbol at the kth subcarrier, s_k is the waveform of the kth subcarrier, T_s is the symbol period, f_k is the frequency of the subcarrier. The optimum detector can be a matched filter or a correlator. The subchannels are orthogonal to each other if:

$$f_k - f_i = m\frac{1}{T_s}; \quad m = \in 1, 2, 3, \ldots \tag{1.2}$$

In any other cases, there will be interference between the subchannels, which decreases the quality of the transmission. The theoretical OFDM modulator and demodulator contain a lot of oscillators and filters. Each subcarrier has its own oscillator which transpose the signal to the proper frequency for transmission then a pass band filter is used to minimize the disturbance. At the end the modulated subcarriers are add together and the OFDM signal is ready. In practice it cannot work because of the frequency faults of the oscillators. Precise oscillators have to be used to minimize the interference, but these oscillators are extremely expensive. Therefore Inverse Discrete Fourier Transformation (IDFT) is used to create the OFDM signal in practice and Discrete Fourier Transformation (DFT) is used for OFDM demodulation. Figure 1.1 shows a typical OFDM transmitter. Data stream is split up N_{sc} parts by a serial-to-parallel converter, and the next block creates the transmitted symbols of the subcarrier from the bit sequence. OFDM modulation is made by the IDFT block. If the subcarriers are not orthogonal to each other (e.g. there is synchronization failure), ISI (Inter Symbol Interference) and ICI (Inter Carrier Interference) will appear in the demodulated signal. This can be avoided if Guard Interval (GI) is applied. It is also called as Cyclic Prefix (CP). A small time period from the end of symbol is copied down. This is the CP and it is placed at the beginning of the symbol. Until the time difference between the subcarriers is smaller than the GI there will not be ISI and ICI in the demodulated signal. After GI is added to the signal, its digital samples are converted into an analogue signal. The optical carrier is modulated by it. After the IDFT block the complex digital signal is separated into two parts: a real (or In phase) and an imaginary (or Quadrature phase) part. These are the I and Q arms of the QAM modulator. The structure of an OFDM demodulator is similar to Fig. 1.1 but the signal flow is reversed so there is a

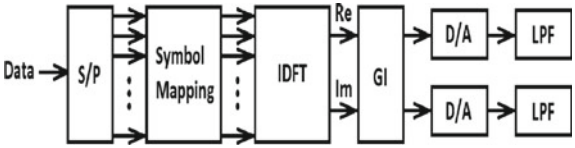

Fig. 1.1 Baseband OFDM transmitter. OFDM modulation is created by IDFT

DFT block instead of the IDFT and it is extended with a clock restore or synchronization block.

Transmitters and receivers have to have huge dynamic range if the PAPR is high. It is not possible to create a device which has large and linear dynamic range. Therefore the value of PAPR must be decreased by coding technique or clipping. The clipping method is usually used, which cuts off the level of the signal above a given value. However, this increases the noise level outside of the signal spectrum.

1.3 Simulation

Block diagram of our transmission is shown in Fig. 1.2 which is based on the proposed system in [8]. Pseudo random bit sequence with 80 Gbps data rate is used in the simulations. OFDM coder use 16-QAM modulation and creates separately the real (I) and imaginary (Q) parts of the OFDM signal. Here is no 90° phase shift between I and Q. The laser signal is modulated separately by I and Q signals. Mach-Zehnder Modulators (MZM) are applied which have sinusoidal transfer characteristic. They are biased at the quadrature point, where the transfer characteristic is linear. I and Q arms are summarized by an optical coupler. Its behaviour is similar to an electrical one. The input signal intensity from both input ports is halved at the output and it creates 90° phase shift between the input ports signals. It means that the necessary 90° phase shift is done by the coupler. So the optical I-Q modulator is built up by two MZMs and an optical coupler. After the coupler a standard Single Mode Fiber (SMF) is placed, when its distortion is examined. In the other cases it is left out from the network. Signal detection is based on the heterodyne detection method. There is a small frequency difference (f) between the laser on the transmitter side and the laser on the receiver side. It causes that the detected signal (at the output of photo diodes) is converted down at f frequency. This signal is demodulated by the OFDM decoder. The analyzer shows the constellation diagram of the detected signal. We supposed that the other elements in the system are ideal or do not make distortion.

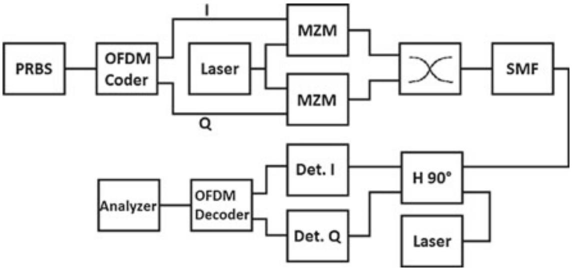

Fig. 1.2 Block scheme of the simulated CO-OFDM system in VPI

1.3.1 Distortion of Mach-Zehnder Modulator

Two arms of the MZMs can be driven independently from each other in VPI. The relation between the arms can be positive or negative. If it is positive then the sign of phase change is the same in both arms. In the other case the sign of the phase change is opposite. Figure 1.3 shows those cases when MZMs upper arm are driven. MZMs are biased with 0.5 V, which causes 90° phase shift (optimum point) in the controlled arm. Both MZM bias points are similarly changed. If the phase delay is less than 90°, the constellation is rotated clockwise (Fig. 1.3b). It is rotated the opposite way (Fig. 1.3a), when the phase shift is more than 90°. This rotation can be compensated by DSP after detection. Another way to eliminate this rotation is the differential driving of MZMs. In this case only the distance between constellation points will decrease when the bias changes (Fig. 1.4a). However, the standard deviation of constellation points is growing linearly (Table 1.1).

There is another MZM driving method when one MZM is driven in the upper arm and the other is driven in the lower arm with negative sign of phase changes. It does not cause any difference in the output light intensity but the electrical field is different. Between the electrical fields there is a 90° phase difference. The optical coupler which summarizes the I and Q signals (Fig. 1.2) also makes 90° phase shift between them. Its result is that if MZMs are biased at the optimum point, there will be no carrier in the transmitted spectrum. In this case we need an outside clock signal to demodulate the received signal which highly complicates the receiver. It can be avoided, if MZMs are not driven in the optimum point. Slightly shifted from the optimum the carrier will appear in the spectrum but the symbols will be closer to each other as Fig. 1.3 shows it. Figure 1.4b shows the received constellation when MZMs are driven asymmetrically (same bias point but the sign of the bias change is the opposite). This driving method minimizes the rotation of the constellation. The standard deviation of symbols does not increase outside from the optimum point of operation.

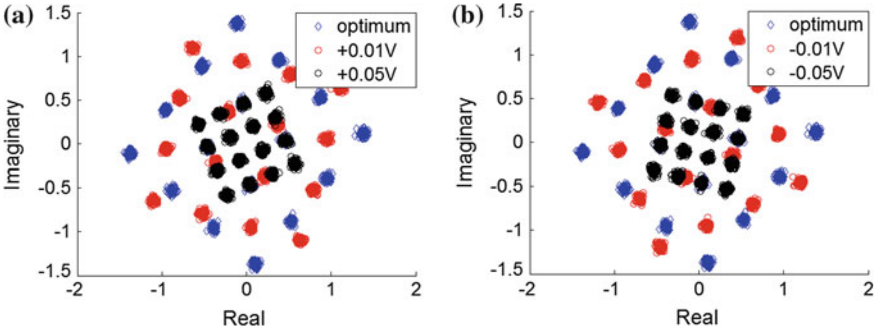

Fig. 1.3 **a** Constellation turns right, if the bias error is positive and it turns left, **b** when the bias changes negatively

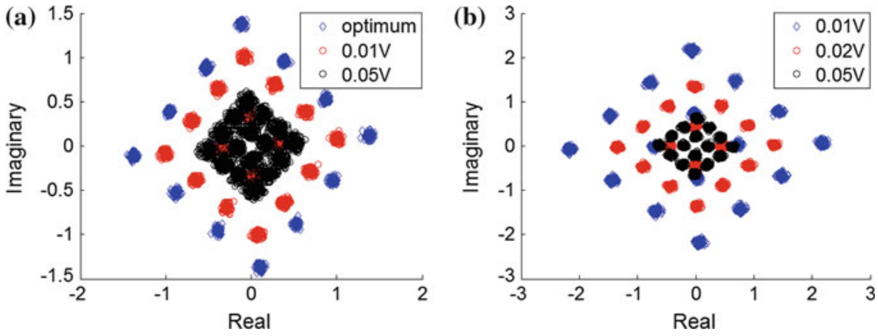

Fig. 1.4 Asymmetrically biased MZMs. **a** Both MZMs are biased at the same arm. **b** MZMs are biased at different arms and the phase change has opposite sign

Table 1.1 Rotation of the constellation

MZM's driving method	Bias (V)	Angle (°)	Deviation
At the same	Optimum	0	0.024
	+0.01	25	0.024
	+0.05	−26	0.024
	−0.01	−25	0.023
	−0.05	26	0.024
Differential	0.01	0.2	0.028
	0.05	1	0.048
Differential, phase change in the MZM's arm is opposite	0.01	0	0.037
	0.02	0.9	0.029
	0.05	3.6	0.025

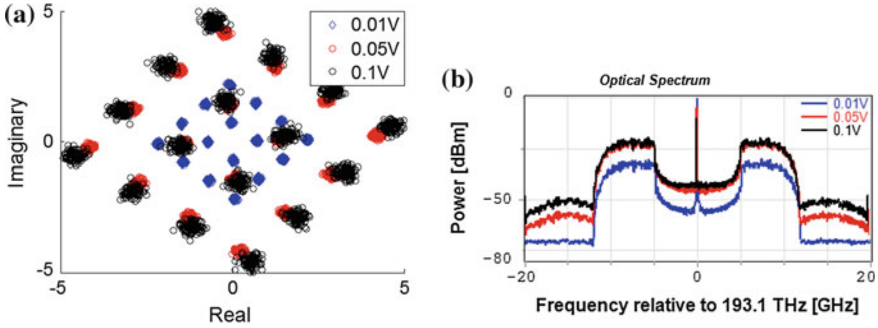

Fig. 1.5 **a** Larger drive amplitude increases the distance between symbols but, **b** outside of the OFDM spectrum the noise level also increases

Larger drive amplitude increases the distance between the symbols of the constellation (Fig. 1.5a) but it does not grow linearly. It has saturation because of the MZM sinusoidal characteristic. Large drive amplitude causes bigger standard deviation of the symbols too. The 0.05 and 0.1 V driving amplitudes are near to the saturation point because the distance between the symbols changed minimally but the standard deviation of the symbols is twice as big. Between the two constellations there is a 3.8° angle. The noise level also increases outside of the signal spectrum (Fig. 1.5b). It comes from the clipping and nonlinearities. This growing noise is harmful in WDM systems, because the channels have to be placed far from each other.

1.3.2 Phase Noise of the Lasers

The linewidth of the lasers is another important factor in the signal quality of optical OFDM systems. To examine the phase noise caused signal distortion the fiber is left out so the transmitter and the receiver are connected directly like in the MZM distortion examination. Linewidth of the lasers changes between 10 kHz and 0.1 GHz. Table 1.2 contains the calculated standard deviations of the constellation diagram. Data in the table have a special symmetry. The standard deviation is not depending on the side where a laser with large linewidth is used. The constellation has the same standard deviation if the transmitter laser linewidth is 10 kHz and the linewidth of the receiver side laser is 100 kHz or the laser linewidths are interchanged. This similarity is shown by Fig. 1.6. The benefit of this symmetry should be utilized. At the transmitter side it is beneficial to use a narrow linewidth laser while a cheaper laser with wider linewidth can be used in the receiver.This method offers a reduction in the price of the system which is good enough to tolerate the signal degradation level using this method. The linewidth of the lasers cannot be larger than 1 MHz if the goal is to reach the best signal transmission quality and the lowest system price. Although the standard deviation of the constellation does not change significantly, the larger laser linewidth increases the noise level. The noise increases with 7 dB when the laser linewidth is changed from 10 kHz to 1 MHz. This noise increase results in a larger standard deviation of the constellation.

If the linewidth of the lasers are larger than 10 MHz the points of the constellation cannot be separated. They will compose one point with huge deviation as

Table 1.2 Laser phase noise caused standard deviation of the constellation diagram

Tx laser linewidth	Rx laser linewidth				
	10 kHz	100 kHz	1 MHz	10 MHz	100 MHz
10 kHz	0.0367	0.039	0.0574	0.1444	0.3247
100 kHz	0.0391	0.0413	0.0589	0.1451	0.3232
1 MHz	0.0573	0.0589	0.0724	0.1513	0.3245
10 MHz	0.1442	0.1449	0.151	0.1993	0.3294
100 MHz	0.3207	0.3213	0.3192	0.329	0.3608

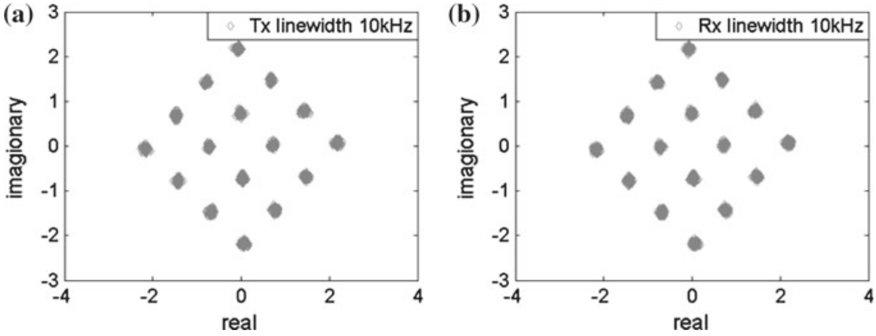

Fig. 1.6 Received constellations if **a** the transmitter laser linewidth is 10 kHz and the receiver side laser linewidth is 100 kHz. **b** The transmitter laser linewidth is 100 kHz and the receiver side laser linewidth is 10 kHz

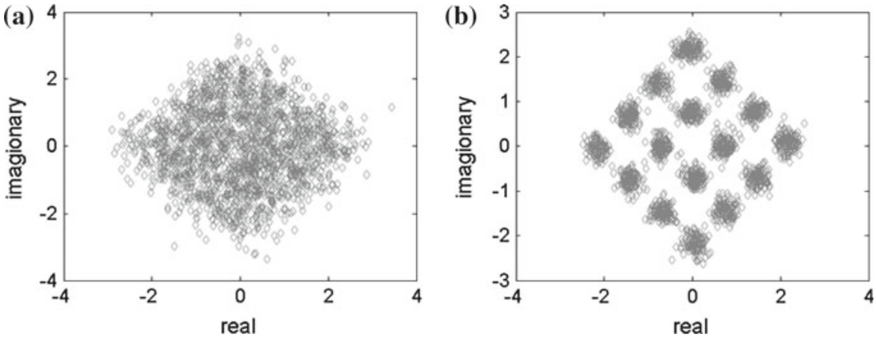

Fig. 1.7 **a** Received constellations if the lasers have larger linewidth than 10 MHz. **b** The constellation diagram if the transmitter laser linewidth is 10 kHz and the receiver side laser linewidth is 10 MHz

Fig. 1.7a shows. The critical laser linewidth is 10 MHz. It highly increases the deviation as it can be observed in Fig. 1.7b. The transmitter laser linewidth is only 10 kHz, but the large (10 MHz) linewidth of the down converting laser spreads the constellation points. If both lasers have 10 MHz linewidth the detected constellation is similar to the Fig. 1.10b. The simulation results show that the laser phase noise spreads the points of the constellation.

1.3.3 Dispersions of the Fiber

Signal shape mainly degrades by the fiber dispersion. Chromatic dispersion is the significant effect in SMF. It rotates the constellation and spreads the symbols (Fig. 1.8a). Constellation of the received signal will be a circle because of the

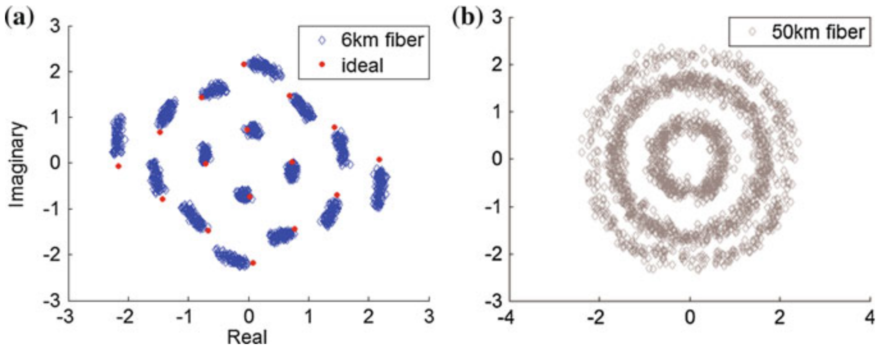

Fig. 1.8 **a** Dispersion spreads the symbols and rotates the constellation. **b** Constellation diagram after 50 km fiber, if dispersion is not compensated

dispersion (Fig. 1.8b). CD has much stronger effect on the transmitted signal than the MZM. 6 km fiber rotates the constellation with angle of 8°. It is twice larger than the rotation caused by differential driving of the MZM. Chromatic dispersion can be compensated by DSP or DCF. Doing it by DSP is much more comfortable because it can be done electronically besides doing other signal processing steps. Using of pilot tones this rotation can be calculated and the correction also can be done.

Polarization mode dispersion becomes critical at high speed. To show its effect the CD has to be negligible because CD has much stronger effect than PMD. Therefore in the simulation any other fiber nonlinearity was turn out except the PMD. Polarization mode dispersion comes from the different propagation time between the two polarization states. Because of it, we examined the PMD effect as the function of the polarization of the laser beams (transmitter and receiver). The usual lasers emit unpolarized beams so the emitted light contains both polarization components. In the simulations the unpolarized laser beams contained the same energy in the two polarization states. If the laser is polarized e.g. at 0° then only the X polarization plane contains energy in the laser beam. The unpolarized laser beam is the worst case in the aspect of the PMD. To simulate this case the degree of the laser polarization was set to 45°. Different fiber lengths (from 1 to 10,000 km) are investigated in the simulations. The PMD coefficient of the fiber is set to 2 and 0.1 ps/km$^{1/2}$ because these are the typical coefficient value for an old and a new fiber, respectively. The received constellation does not change significantly for 500 km as Fig. 1.9a shows. The size of the constellation does not change, however its standard deviation is increased (Table 1.3). The points of the constellation go to the centre and they rotate inverse clockwise as the fiber length was increased up to 10,000 km. Therefore some decision ranges overlap each other (Fig. 1.9).

PMD caused distortion should be smaller if polarized lasers are used, because in that case there is only one polarization in the fiber. However, the polarization state of the fiber changes randomly, so at the end of the fiber both polarizations will contain some signal components. The PMD caused polarization changes can result in 90°

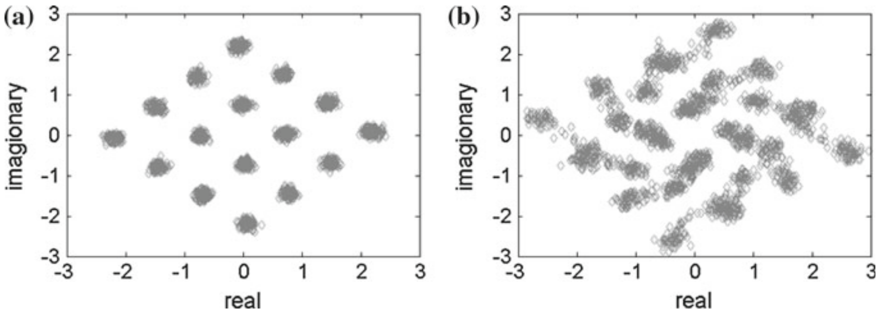

Fig. 1.9 Received constellations if the PMD coefficient is 0.1 ps/km$^{1/2}$. The lasers are unpolarized and the fiber length is **a** 500 km, and **b** 10,000 km

Table 1.3 Standard deviation of the constellation if the fiber PMD coefficient is 0.1 ps/km$^{1/2}$

Fiber length (km)	Transmitter/receiver laser polarization (°)			
	45/45	0/0	0/45	45/0
1	0.068	0.065	0.0521	0.1166
5	0.0566	0.0611	0.0539	0.1356
10	0.0671	0.2229	0.0765	0.0679
50	0.0551	0.0674	0.0542	0.716
100	0.0641	0.1085	0.1177	0.0778
500	0.0696	0.0782	0.1987	0.165
1000	0.1191	0.1059	0.3999	0.0708
5000	0.0951	0.1099	0.0793	0.0757

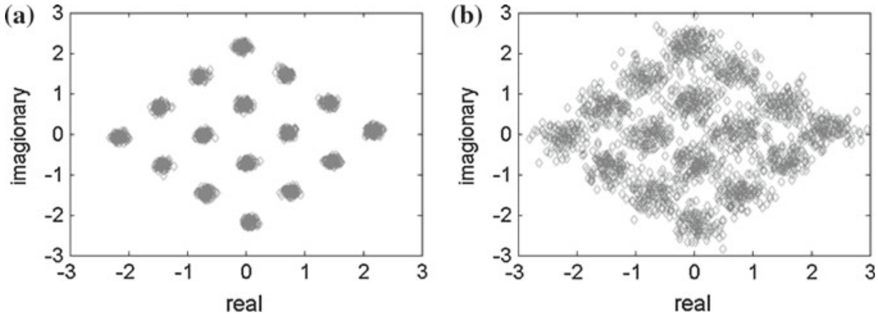

Fig. 1.10 Received constellations if the PMD coefficient is 0.1 ps/km$^{1/2}$. The lasers are polarized (0°) and the fiber length is **a** 5 km and **b** 10 km

polarization differences between the transmitter and the receiver signals. In that case the two signals are orthogonal to each other and the receiver cannot demodulate the received signal. Figure 1.10 shows the PMD caused signal distortion if the lasers are polarized at 0°. The detected constellation does not have any significant distortion

(Fig. 1.10a) if the fiber length is 5 km or 50 km. But the points spread largely if the distance is 10 km (Fig. 1.10b), because the polarization state of the received signal and the receiver laser is near to 90°. At this length the uncertainty of the decision is very high. The centre of the constellation points can be determined but the large spread increases the probability of wrong decision. The standard deviation of the constellations is not better than the deviation of the unpolarized system (Table 1.3). It is due to the polarization sensitivity of the detection method. At the receiver another laser is used to demodulate the signal which converted it down it to a lower frequency. If the polarization of the signals is orthogonal to each other only noise is detected by the analyzer. This polarization sensitivity is higher than in the case when the PMD caused smaller distortion on a polarized light.

In the previous simulations the PMD coefficient was set to 0.1 ps/km$^{1/2}$, which is close to the coefficient of the new fibers. However, most telecommunication fibers are older than 10 years, so their PMD coefficient is about 2 ps/km$^{1/2}$. Because of that, the simulations are repeated and this higher PMD value is set in the fiber parameters. Distortion can be observed on the constellation in case of a 5 km fiber length. Figure 1.11 shows the distorted constellation at 50 km fiber length. The points are spread and it looks like they are on a circle. This behavior is similar to the chromatic dispersion caused distortion. However, most of the constellation points split into two distinct parts. Chromatic dispersion caused distortion does not make this separation. It spreads the points into a circle (Fig. 1.8b). PMD caused distortion for longer fibers are similar to the case of the low PMD coefficient fiber. The points of the constellation move to the centre and are rotated. Using polarized (0°) light the effect of the PMD is similar to the case of the lower PMD coefficient. The polarization mismatch at the receiver increases the deviation of the constellation (Table 1.4).

PMD has smaller effect on the signal if the light is polarized, but our detection method cannot profit from this benefit if both lasers have the same polarization. There is a chance to improve the PMD insensitivity if polarization requirement of the fiber and the receiver is used at the same time. Therefore, the transmitter laser was polarized at 0° because PMD has smaller effect to a polarized light. To avoid the signal degradation from the polarization mismatch an unpolarized laser is used in the receiver. In the simulation the lower PMD coefficient is applied. This mixed polarization offers a better signal quality for short (less than 10 km) fiber length

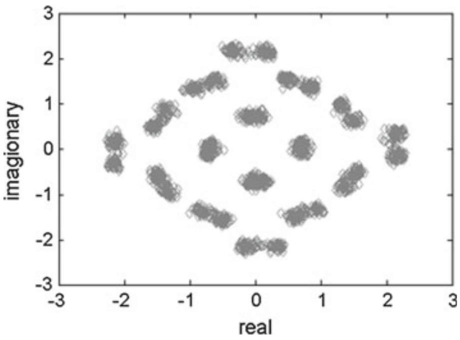

Fig. 1.11 Received constellations if the PMD coefficient is 2 ps/km$^{1/2}$, the lasers are unpolarized and the fiber length is 50 km

Table 1.4 Standard deviation of the constellation if the fiber PMD coefficient is 2 ps/km$^{1/2}$

Fiber length (km)	Transmitter/receiver laser polarization (°)			
	45/45	0/0	0/45	45/0
1	0.0771	0.0822	0.0652	0.1573
5	0.1046	0.15	0.0665	0.231
10	0.1362	0.3212	0.1675	0.1463
50	0.1289	0.1649	0.0603	0.1663
100	0.1829	0.2627	0.2837	0.209
500	0.2556	0.2544	0.4753	0.4274

than the unpolarized lasers (Table 1.3). Between 10 and 100 km the constellation is quite similar to the results of the unpolarized lasers (Fig. 1.12). However, the standard deviation of the constellation is increased significantly if the fiber length is longer than 500 km. The mixed polarization can reduce the PMD effect at short ranges. The laser polarization can be reversed but it will result in a worse signal transmission. Because the transmitter is unpolarized the PMD has higher effect on the signal which results in a larger standard deviation (Table 1.3). The unpolarized signal transmission provides better signal transmission at all examined fiber lengths than the mixed polarization. Although the standard deviation of the constellation is increased but moving of the constellation is eliminated. Similar results can be observed if the higher PMD coefficient fiber is used in the simulations. Only the length of the transmission is shortened. The maximum fiber length is 50 km then the points of the constellation are overlapped.

1.3.4 Fiber Nonlinearity

Four wave mixing (FWM) and self-phase modulation (SPM) make smaller signal degradation than CD or PMD. They appear, if the power density in the fiber is

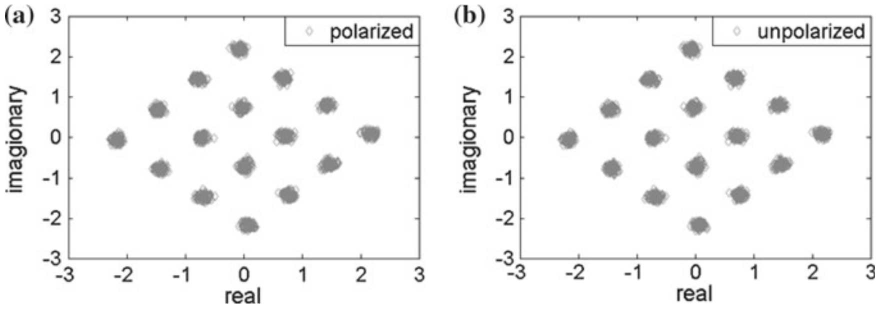

Fig. 1.12 Received constellations if the PMD coefficient is 0.1 ps/km$^{1/2}$, and the fiber length is 50 km. **a** Transmitter laser is polarized and the laser at the receiver side is unpolarized. **b** Both lasers are unpolarized

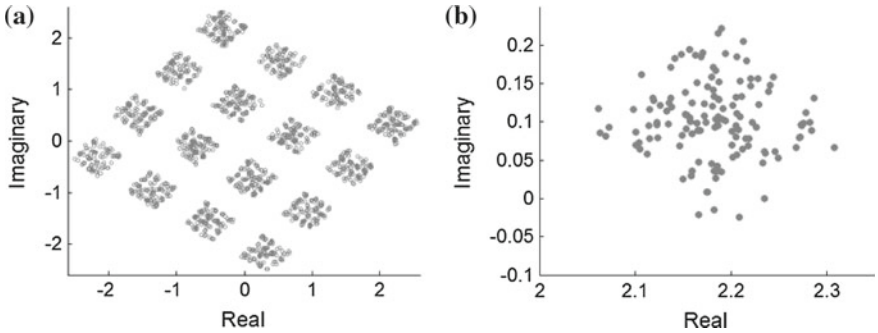

Fig. 1.13 **a** Symbol deviation caused by SPM and FWM. **b** Only FWM caused symbol spread at one point of the constellation

above 1 W. The dispersion of the fiber is set to zero to examine only the effect of nonlinearity. Laser power is 20 W and fiber length is 50 km. Increasing the laser power will not improve the quality of transmission. Noise level increases outside of the OFDM spectrum because of FWM. Constellation symbols highly spread and it seems they contain the full constellation diagram in small size (Fig. 1.13a). This kind of modulation mainly comes from the SPM and in smaller extent from the FWM. Decreasing the laser power the SPM effect will be negligible and FWM will be dominant. FWM causes ICI and it spreads the symbols along both axes (Fig. 1.13b). It is similar to the effect of white noise. Standard deviation is 0.0472 which is twice as much as that one caused by the MZM.

1.4 Conclusions

In this paper we showed the major distortion effect on the transmitted signal. Chromatic dispersion has the strongest signal degradation effect among the investigated distortions. However, it can be compensated, the easiest way is using DCF. A more compact CD compensation solution is made by DSP. CD caused distortion will not play an important role in optical OFDM systems because its value can be fully controlled.

Distortion of the MZM is similar to the CD caused one. It rotates the constellation and the symbol distances depend on the bias point of the MZM. The rotation caused by MZM can be easily eliminated by differential driving. It minimizes the rotation but the standard deviation of symbols is increased slightly. If the electrical field of MZM provides opposite rotation this effect does not exist and the rotation stays small. The nonlinearity of the modulator also can be compensated by DSP, but this solution requires plus equipment, which increases the price. Laser phase noise increases the standard deviation of the constellation diagram. In our system two lasers are applied and they show symmetry in the phase noise investigation.

The standard deviation of the constellation diagram is independent from the place of the narrow linewidth laser. It is the same if the narrow linewidth laser is put into the transmitter or it is placed at the receiver side. Using a narrow linewidth laser at either side of the system the phase noise caused distortion can be significantly decreased.

PMD not only spreads the constellation points but it rotates them and in some cases it splits the points into two pieces. The use of low PMD coefficient fiber is the most efficient way to decrease the PMD effect. However, to replace all fibers with a new low PMD coefficient one is extremely expensive. Using polarized light smaller PMD caused signal distortion can be achieved, but the applied detection method is sensitive for the polarization state. It is pointed out that using polarized light a higher distortion is obtained because of the polarization sensitivity of the detecting method. The golden way between the polarization sensitivity and the PMD effect is the mixed polarization. Transmitter laser is polarized to decrease the PMD effect while at the receiver side an unpolarized laser is used to minimize the polarization sensitivity of the receiver. This gives better results compared to the case when both lasers are unpolarized. However, using only polarized lasers a major drawback is encountered. If the polarization of the transmitter laser is orthogonal to the laser polarization at the receiver, no signal detection will occur. Only the noise will be detected. The chance of this orthogonality is small but we showed it can cause high signal degradation independently of the fiber length. As both polarizations are used to decrease the PMD it will make difficulties in the future when the signal transmission is multiplexed in polarization too.

Other nonlinearities of SMF (e.g. four wave mixing, self phase modulation) cause smaller distortion and they are covered by the distortion effect of MZM nonlinearity, CD or PMD. We usually use low laser power so only FWM will influence the transmission.

Most of the examined distortion can be compensated without any plus equipment. CD is one of the exceptions which needs plus hardware to eliminate its distortion. It is beneficial to do post CD compensation by DSP, because then DSP can be used to compensate the other distortions effect. There is a question; is it worth to do everything with a DSP or it is better to apply proper MZM driving technique (e.g. differential driving) or using small linewidth lasers.

References

1. W. Shieh, OFDM for flexible high-speed optical networks, J. Lightwave Technol., **29**(10) (2011)
2. W. Shieh, H. Bao, Y. Tang, Coherent optical OFDM: theory and design, Opt. Exp. **16**(2) (2008)
3. W. Shieh, I. Djordjevic, *Orthogonal frequency division multiplexing for optical communication* (Academic Press, London, 2010)
4. B. Collings, F. Heismann, G. Lietaert, *Reference guide to fiber optic testing*, **2**, JDSU (2010)
5. S. Ten, M. Edwards, *An introduction to the fundamentals of PMD in fibers*, WP5051, Corning Incorporated (2006)

6. F. Heismann, *Polarization mode dispersion: fundamentals and impact on optical communication systems*, ECOC (1998)
7. J. Armstrong, OFDM for optical communications, J. Lightwave Technol. **27**(3) (2009)
8. H. Louchet, A. Richter, *Novel scheme for high bit-rate coherent OFDM transmission without PLL*, ECOC (2007)

Chapter 2
DQPSK Optical Networks Impaired by Multi Line Rates and Mixed Modulation Formats Interferers

João L. Rebola, Luís G.C. Cancela and João J.O. Pires

Abstract Future metropolitan optical networks face the challenge of having signals with different modulation formats and different bit rates coexisting in the network. The interference between those signals, and mainly from signals at the same wavelength, named in-band crosstalk, may lead to severe network performance degradation. In this work, the performance of 40 Gb/s DQPSK optical receivers impaired by in-band crosstalk due to mixed modulation formats and multiple line rates is assessed. It is shown that the most severe performance degradation due to in-band crosstalk is caused by 10 Gb/s interferers, being the OOK interferer the most detrimental to the network performance. We show also that the reduction of the duty-cycle of the interferers increases the DQPSK optical receiver tolerance to in-band crosstalk.

2.1 Introduction

Nowadays, optical networks have the capability of transporting signals with multiple modulation formats and a multitude of bit rates, in order to support the growing traffic capacity demands. The actual trend is to further increase the number

---

J.L. Rebola (✉) · L.G.C. Cancela · J.J.O. Pires
Instituto de Telecomunicações, Av. Rovisco Pais 1, 1049-001 Lisbon, Portugal
e-mail: joao.rebola@iscte.pt; joao.rebola@lx.it.pt

L.G.C. Cancela
e-mail: luis.cancela@iscte.pt

J.J.O. Pires
e-mail: jpires@lx.it.pt

J.L. Rebola · L.G.C. Cancela
Department of Information Science and Technology, Instituto Universitário de Lisboa
(ISCTE-IUL), Av. das Forças Armadas, Edifício II, 1649-026 Lisbon, Portugal

J.J.O. Pires
Department of Electrical and Computer Engineering, Instituto Superior Técnico,
Lisbon, Portugal

P.A. Ribeiro and M. Raposo (eds.), *Photoptics 2014*,
Springer Proceedings in Physics 177, DOI 10.1007/978-3-319-27321-1_2

of different formats and bit rates that coexist in the network [9, 15]. The main reason for this increase is the widespread use of coherent technology and the flexibilisation of the 50 GHz optical grid—the so called flexgrid [11]. Nevertheless, this technology, that allows the use of advanced modulation formats with greater spectral efficiency and increased signal bit rate, is mostly used in long-haul networks [14]. On the other hand, optical metropolitan area networks (MANs) are still based in intensity modulation direct detection systems, because of their simplicity and low power consumption characteristics. The typical signals coexisting in these metro networks are the 10 Gb/s OOK (On-Off Keying) and DPSK (Differential Phase-Shift Keying) signals, and the 40 Gb/s DPSK and DQPSK (Differential Quadrature Phase-Shift Keying) signals.

The physical constraints of optical MANs are an important issue in network planning and performance evaluation. In particular, in-band crosstalk is considered an important physical limitation [8]. The impact of this phenomenon has been intensively studied in direct detection systems. In the majority of these studies, it is assumed that the crosstalk signals have the same bit rate and modulation format than the selected signal. Examples of these studies for OOK, DPSK and DQPSK signals are, respectively, given in [1, 2, 10]. There are also a few studies which consider that the selected signal has a different bit rate and modulation format than the crosstalk signals [3, 5]. In [3], an analytical formalism is used to evaluate the impact of a single OOK interferer in a DPSK system, and in [5] the impact of a single OOK/DPSK/DQPSK interferer in a DPSK system is evaluated in an experimental and simulation setup.

In this work, we extend these studies and evaluate the impact of in-band crosstalk due to 10/40 Gb/s OOK/DPSK/DQPSK multiple interferers on the performance of 40 Gb/s DQPSK optical receivers. The crosstalk impact is evaluated by Monte Carlo (MC) simulation, and an analytical formalism based on the moment generating function [2] is used to validate the MC simulation for the single interferer scenario. The impact of the extinction ratio of OOK signals and the impact of the crosstalk signal duty cycle on the receiver performance are also assessed.

This paper is structured as follows. Section 2.2 describes the simulation model to assess the impact of multi-format interferers in a DQPSK receiver. Numerical results are discussed in Sect. 2.3 and conclusions are presented in Sect. 2.4.

2.2 System Description

In this section, the model used to characterise the DQPSK optical receiver is described. The implementation of the MC simulator used to assess the performance of the optical receiver when impaired by in-band crosstalk is also presented.

2.2.1 Optical DQPSK Receiver

The structure of a typical differential direct detection DQPSK receiver is depicted in Fig. 2.1, [6]. It consists of an optical pre-amplifier with a constant power gain G over the amplifier bandwidth; an optical filter with −3 dB bandwidth B_o; and a −3 dB coupler to split the signal between the two branches of the optical receiver. Each branch of the optical receiver consists of a delay line interferometer with a differential delay equal to the symbol period T_s; a balanced photodetector; and a post-detection electrical filter with −3 dB bandwidth B_e. In the lower branch (Q), the arms of the interferometer have a phase difference of π/4, while in the upper branch (I), the interferometers arms phase difference is −π/4 [6]. Throughout this work, the possible imperfections of the optical DQPSK receiver are neglected.

The electrical field at the optical filter output, $\vec{E}(t)$, can be expressed as [2]

$$\vec{E}(t) = \left[\sqrt{G}\cdot\vec{E}_s(t) + \sqrt{G}\cdot\sum_{i=1}^{M}\vec{E}_{c,i}(t) + \vec{E}_{ASE}(t)\right] * h_o(t) \tag{2.1}$$

where * stands for convolution and $h_o(t)$ is the impulse response of the optical filter. The first term of (2.1), $\vec{E}_s(t)$, corresponds to the electrical field of the incoming DQPSK signal, named selected signal and is described as $\vec{E}_s(t) = \sqrt{P_s}\ \exp[j\theta_s(t)]\vec{e}_s$, where P_s is the average signal power at the optical pre-amplifier input; $\theta_s(t)$ is the signal phase that carries the DQPSK symbol information, with possible values $\{\pi/4, 3\pi/4, -3\pi/4, -\pi/4\}$; and $\vec{e}_s$ is the signal polarization unit vector.

The second term of (2.1), $\sum_{i=1}^{M}\vec{E}_{c,i}(t)$, corresponds to the electrical field of the in-band crosstalk, with M possible interferers. The complex envelope of the ith crosstalk signal field can be represented as

$$\vec{E}_{c,i}(t) = \sqrt{P_{c,i}}A_{c,i}\left(t+\Delta\tau_{c,i}\right)\cdot\exp\left[j\left(\theta_{c,i}(t+\Delta\tau_{c,i}) + \Delta\phi_{c,i}\right)\right]\vec{e}_c \tag{2.2}$$

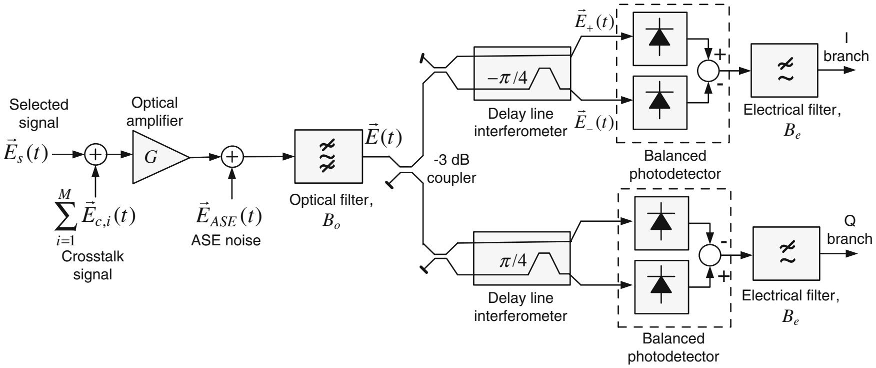

Fig. 2.1 Block diagram of the DQPSK optical receiver

where $P_{c,i}$ is the crosstalk power. The crosstalk level of the ith interferer is defined as the ratio between the crosstalk power, $P_{c,i}$, and the signal power, P_s. The total crosstalk level is the sum of the crosstalk levels of the M interferers. In (2.2), $\Delta\tau_{c,i}$ is a random time shift within one symbol period, which is modelled considering a uniform distribution over that period [13]; $\Delta\phi_{c,i}$ is a random phase difference with respect to the selected signal, which is modelled considering a uniform distribution over the interval [0, 2π[[13]; $\vec{e}_c$ is the crosstalk signal polarisation unit vector, which as a worst-case assumption is assumed co-polarised with the selected signal, $\vec{e}_s = \vec{e}_c$; $A_{c,i}(t)$ and $\theta_{c,i}(t)$ are, respectively, the envelope and the phase of the crosstalk signal, which define the modulation format of the ith interferer. The modulation formats and bit rates of the crosstalk signal considered in this work are 10 Gb/s OOK, 10 Gb/s DPSK, 40 Gb/s OOK, 40 Gb/s DPSK and 40 Gb/s DQPSK. The extinction ratio of the OOK crosstalk signals is defined as $r = P_1/P_0$, with P_1 defining the average power of the bits ‘1’ and P_0 the average power of the bits ‘0’. The duty-cycle of RZ (Return-to-Zero) pulses, D, is defined as the fraction of time that a rectangular pulse lasts within a symbol period, before it returns to zero.

The third term of (2.1), $\vec{E}_{ASE}(t)$, corresponds to the complex envelope of the electrical field of the amplified spontaneous emission (ASE) noise originated at the optical pre-amplifier. The ASE noise is assumed as a zero mean white stationary Gaussian noise with single-sided power spectral density in each polarisation described by $N_o = h\nu_s GF/2$, where $h\nu_s$ is the photon energy at the signal wavelength, and F is the pre-amplifier noise figure.

The −3 dB couplers and delay interferometers are modelled as in [12]. For the I branch, the electrical fields $\vec{E}_+(t)$ and $\vec{E}_-(t)$ are described by

$$\begin{bmatrix} \vec{E}_+(t) \\ \vec{E}_-(t) \end{bmatrix} = \frac{1}{2\sqrt{2}} \begin{bmatrix} j\vec{E}(t) + j\vec{E}(t - T_s) \cdot \exp(-j\pi/4) \\ -\vec{E}(t) + \vec{E}(t - T_s) \cdot \exp(-j\pi/4) \end{bmatrix} \tag{2.3}$$

Using the same model described in [12], the electrical fields after the delay line interferometer of the Q-branch of the optical receiver can be readily calculated. The photodetectors are modelled as ideal square-law detectors.

2.2.2 *Monte Carlo Simulation*

In the MC simulation, a sequence of bits of length N_b corresponding to the information carried by the DQPSK selected signal is generated using deBruijn sequences [7]. The differential encoding and conversion to quaternary symbols with Gray coding follows [4, 6]. Then, the sequence of symbols is discretized in N_a samples per symbol, which allows considering the signal waveform within a symbol period [for example, non-RZ (NRZ) or RZ pulses]. Hence, the effect of intersymbol interference on the performance of the DQPSK optical receiver can be rigorously evaluated on the MC simulation.

In the simulator, the ASE noise is generated using a random number generator, which follows a Gaussian distribution with zero mean and variance of $N_o \cdot B_{sim}$, where B_{sim} is the bandwidth used in the MC simulation. In each iteration of the simulation, a sample function of the ASE noise is generated [7].

At that same iteration, a sample function of the crosstalk signal is also constructed. Each ith crosstalk signal is generated considering a random sequence of bits, which are, then modulated. The same modulation format is considered for all ith crosstalk signals.

After the generation of selected signal, crosstalk signal and ASE noise sample functions, the electrical field given in (2.1) is obtained and is propagated through the DQPSK optical receiver depicted in Fig. 2.1. The current at the output of the I branch and Q branch is, then, determined and sampled at the time instants corresponding to the maximum eye-opening obtained without noise and crosstalk. After sampling, each received bit in its respective branch, which is corrupted by noise and crosstalk, is compared to the corresponding transmitted bit to find out if an error has occurred. The bit error probability (BEP) is, then, calculated from [4]

$$BEP = \frac{BEP_I + BEP_Q}{2} \tag{2.4}$$

where BEP_I and BEP_Q are the bit error probabilities, respectively, of the I and Q branches, which are estimated through direct error counting using

$$BEP_I = \frac{N_{E,I}}{N_{it} \cdot N_b/2} \tag{2.5}$$

$$BEP_Q = \frac{N_{E,Q}}{N_{it} \cdot N_b/2} \tag{2.6}$$

where N_{it} is the number of iterations of the MC simulation, which is equivalent to the number of simulated sample functions and $N_{E,I}$ and $N_{E,Q}$ are the number of counted errors, respectively, in the I and Q branches of the receiver. A specific number of counted errors is set as a stopping criterion of the MC simulation.

2.3 Numerical Results

In this section, the impact of multi-format and multi-rate crosstalk signals on the performance of 40 Gb/s DQPSK pre-amplified optical receivers is evaluated using MC simulation. The duty-cycle variation of the crosstalk signals, the extinction ratio variation of OOK crosstalk signals and single and multiple interference are considered in these studies.

Throughout this section, the amplifier noise figure, F, is 5 dB, the pre-amplifier gain, G, is 30 dB, and both ASE noise polarisations are considered. The optical filter is a Gaussian filter with normalized −3 dB bandwidth given by $B_o T_s = 5$. The electrical filter is a Gaussian filter with normalized −3 dB bandwidth given by $B_e T_s = 0.7$. The optical signal-to-noise ratio (OSNR) is measured in the reference bandwidth of 0.1 nm at $\lambda_s = 1550$ nm. The total crosstalk level considered for the interferers is −13 dB, for all data rates and modulation formats. This means that the power corresponding to the sum of powers of each individual interferer is −13 dB below the original DQPSK signal power. We also assume that the power is equally distributed by the interferers. The modulation formats of the crosstalk signal considered are 10 Gb/s OOK, 10 Gb/s DPSK, 40 Gb/s OOK, 40 Gb/s DPSK and 40 Gb/s DQPSK. The bit rate of the selected DQPSK signal is 40 Gb/s. The number of simulated bits is $N_b = 2^7$, $N_a = 128$ samples per symbol and $B_{sim} = 5.1$ THz are used. The BEP is estimated using MC simulation considering at least $N_{E,I} = 1000$ or $N_{E,Q} = 1000$ counted errors. This high number of counted errors, in comparison with the typical 100 errors used in MC simulation [7], has been set to obtain BEP curves with a very smooth behavior.

2.3.1 Single and Multiple Interference in Multi-rate and Multi-format Scenarios

In this subsection, the impact of multi-rate and multi-format crosstalk signals on the selected DQPSK signal is evaluated. The pulse shape of all modulation formats is NRZ and the extinction ratio of the OOK interferers is ideal, $r = \infty$. The influence of the random time shift $\Delta\tau_{c,i}$ is neglected, since it has been verified that its influence on the receiver performance is minor, when considering NRZ pulse shapes.

Figure 2.2 shows the BEP as a function of the OSNR, for a single interferer, $M = 1$, with different modulation formats and bit rates on the crosstalk signal. The BEP obtained without crosstalk is also depicted in Fig. 2.2 for comparison purposes. To check the MC simulation results, the BEP is also computed using the analytical formalism (A) proposed in [2], considering the absence of crosstalk and a 40 Gb/s DQPSK crosstalk signal. This analytical formalism is capable of assessing in a rigorous way the impact of in-band crosstalk in DQPSK receivers independently of the optical and electrical filter shapes, considering the isolated DQPSK symbol scenario. This formulation was first developed in [10] for analysing the impact of in-band crosstalk in DPSK receivers and uses an eigenfunction expansion technique to decompose signal, crosstalk, and ASE noise, at the optical filter input, in a series of orthogonal functions and relies on the moment generating function to

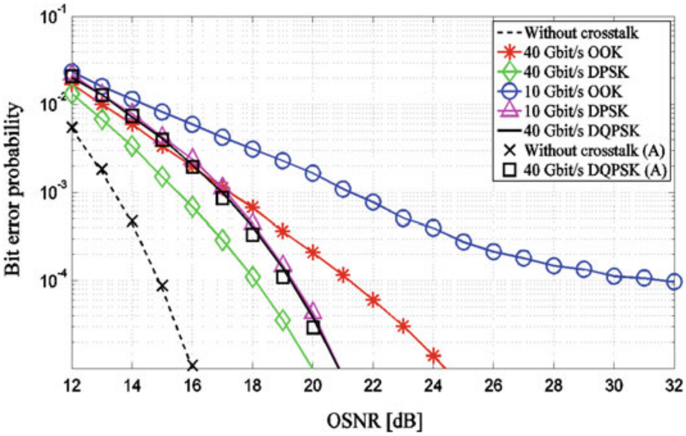

Fig. 2.2 BEP as a function of the OSNR for a single interferer, $M = 1$ and different modulation formats and bit rates on the crosstalk signal

describe the decision variable statistics. From Fig. 2.2, a good agreement between simulation and analytical results is observed.

Figure 2.2 shows that the 10 Gb/s OOK crosstalk signal leads to the most severe interference on the 40 Gb/s DQPSK optical receiver. For very high OSNR, the BEP is reaching a floor. The 40 Gb/s OOK interferer leads to the second worst BEP degradation, especially for OSNRs above 17 dB, where the signal-crosstalk beating power is becoming significant. The 40 Gbs DQPSK and 10 Gb/s DPSK crosstalk signals provide similar performances, while the less harmful interferer is the 40 Gb/s DPSK. As a main conclusion, the interference of amplitude modulated signals leads to higher BEP degradation than phase-modulated signals interference. This conclusion is in agreement with the results presented in [5] for a single interferer and considering a 40 Gb/s DPSK signal as the selected signal. This conclusion is similar to the one found in the presence of cross-phase modulation (XPM) [11]. Amplitude modulated signals at 10 Gb/s induce a higher XPM on coexisting phase modulated signals at higher bit rates, and as a result, lead to higher performance degradation.

It is still an open issue if this scenario is kept for $M > 1$. Figures 2.3 and 2.4 depict the BEP as a function of the OSNR for, respectively, $M = 4$ and $M = 8$ interferers, considering different modulation formats and bit rates on the crosstalk signals. It should be pointed out that, we have considered that, all M interferers have the same modulation format and bit rate.

Figure 2.3 shows that, for $M = 4$, the BEP reaches a floor for high OSNRs for all crosstalk signals, except for the 40 Gb/s DPSK interferer case. For such high OSNRs, the beating between signal and crosstalk is dominating the optical receiver performance, and the power increase of the selected signal gives no longer any performance improvement. The higher BEP degradation occurs also for the 10 Gb/s interferer. However, in comparison with $M = 1$, the 10 Gb/s DPSK interferer leads

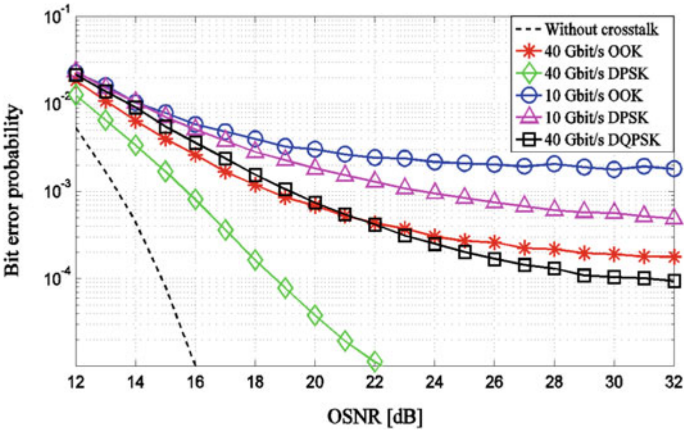

Fig. 2.3 BEP as a function of the OSNR for $M = 4$ interferers and different modulation formats and bit rates on the crosstalk signal

to a higher BEP degradation than 40 Gb/s OOK and DQPSK signals, which exhibit a similar performance.

Figure 2.4 shows the enhancement of the behaviours observed in Fig. 2.3, with the increase of the interferers number. The 40 Gb/s OOK and 40 Gb/s DQPSK crosstalk signals lead practically to the same receiver performance. The BEP with the 10 Gb/s DPSK crosstalk signal is becoming similar with the 10 Gb/s OOK crosstalk signal. Notice that between Figs. 2.3 and 2.4, the increase on the number of interferers had no particular influence on the BEP, when considering the 10 Gb/s

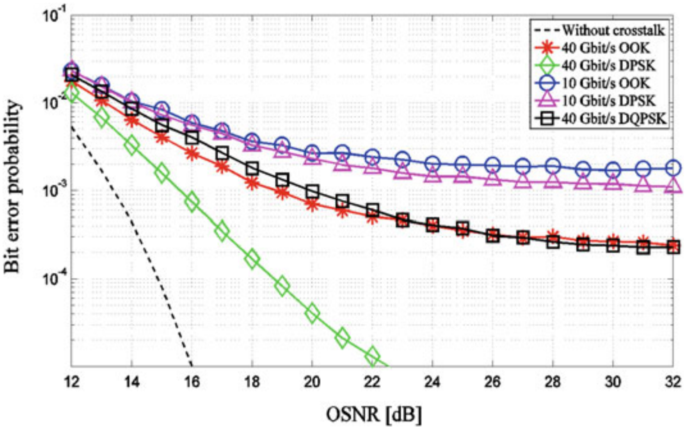

Fig. 2.4 BEP as a function of the OSNR for $M = 8$ interferers and different modulation formats and bit rates on the crosstalk signal

OOK signal. This means that the superposition of the symbol patterns of the interferers is not contributing for further degradations of the receiver performance. For the 40 Gb/s DPSK crosstalk signal, the increase of the number of interferers practically does not influence the BEP.

As a main conclusion, we have seen that with the increase on the number of interferers, the slower bit rate signals, 10 Gb/s, are the ones that lead to a higher BEP degradation. As the bit rate is smaller, when there is a combination of symbols on the crosstalk signals that impairs significantly the receiver performance, it affects at least four times the same number of symbols on the selected 40 Gb/s DQPSK signal.

2.3.2 Duty-Cycle Variation

In this subsection, the influence of the duty-cycle of the crosstalk signals on the receiver performance is investigated. All results are obtained considering a 40 Gb/s DQPSK NRZ signal and M = 4 interferers. In these studies, the influence of a random time shift $\Delta\tau_{c,i}$ inside the symbol period is taken into account in the BEP estimation. Although the main qualitative conclusions are not changed, the values of the BEP may differ noticeably, when neglecting this random time shift for interferers with RZ pulse shape.

Figures 2.5, 2.6 and 2.7 show the BEP as a function of the OSNR for, respectively, 10 Gb/s OOK, 10 Gb/s DPSK and 40 Gb/s DQPSK crosstalk signals, for several duty-cycles. The extinction ratio of the OOK interferers is assumed ideal, $r = \infty$.

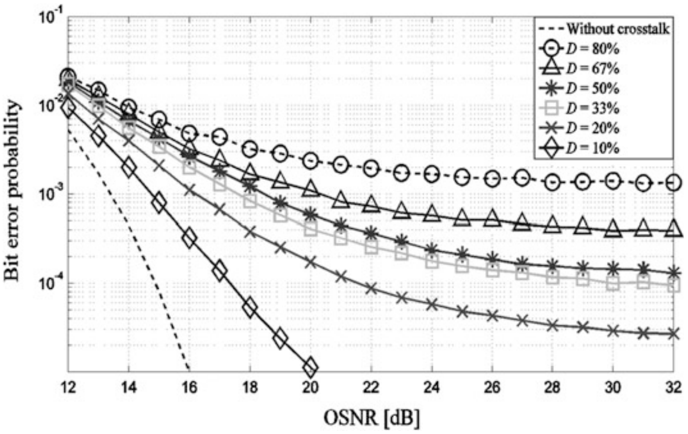

Fig. 2.5 BEP as a function of the OSNR for 10 Gb/s OOK crosstalk signal with M = 4 and different duty-cycles

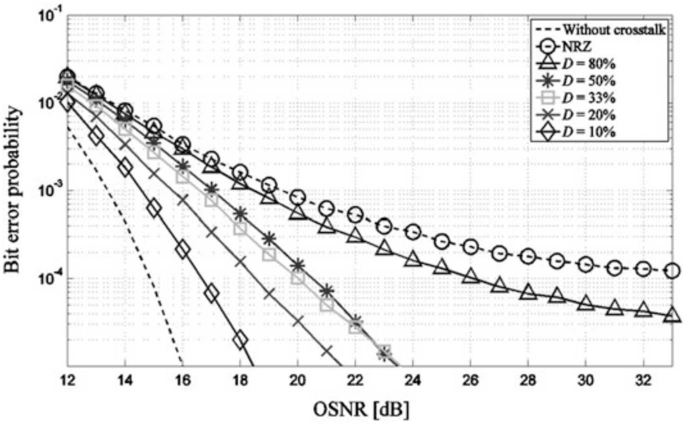

Fig. 2.6 BEP as a function of the OSNR for 10 Gb/s DPSK crosstalk signal with $M = 4$ and different duty-cycles

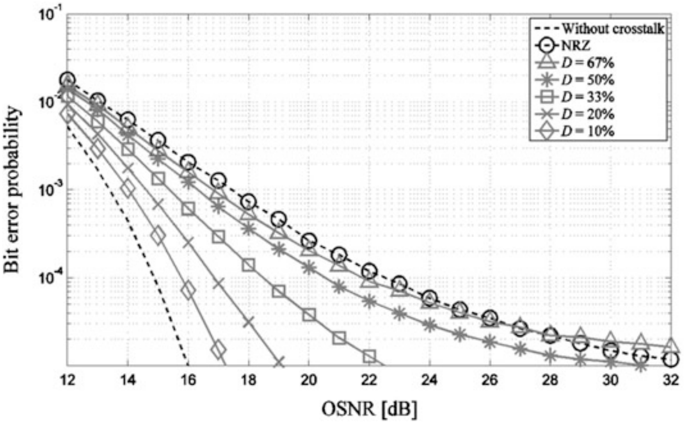

Fig. 2.7 BEP as a function of the OSNR for 40 Gb/s DQPSK crosstalk signal with $M = 4$ and different duty-cycles

Figures 2.5, 2.6 and 2.7 show that the reduction of the duty-cycle of the interferers reduces the crosstalk impact on the receiver performance. For very low duty-cycles (below 20 %), the BEP estimated in the presence of crosstalk becomes very close to the BEP estimated in its absence. With the duty-cycle reduction, the fraction of time of the pulse that is interfering with one pulse of the selected signal is becoming smaller, and the crosstalk impact on the receiver performance is decreased, although the total crosstalk power is the same.

Similar conclusions to those taken from Figs. 2.5, 2.6 and 2.7 have been drawn when considering 40 Gb/s OOK and 40 Gb/s DPSK crosstalk signals.

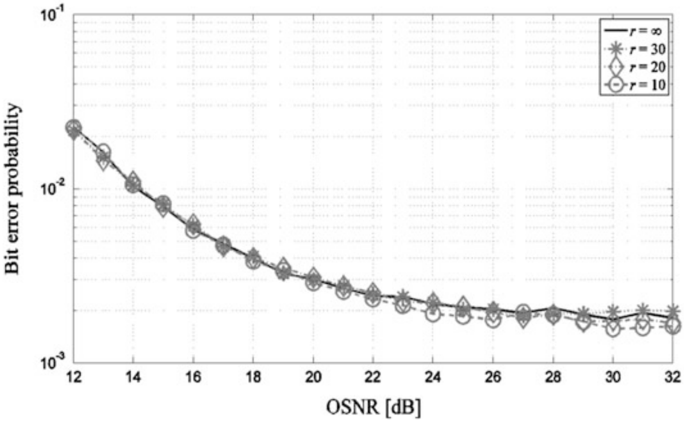

Fig. 2.8 BEP as a function of the OSNR for 10 Gb/s OOK NRZ crosstalk signal with $M = 4$ and different extinction ratios

2.3.3 Extinction Ratio Variation

In this subsection, the influence of the extinction ratio of 10 and 40 Gb/s OOK interferers on the 40 Gb/s DQPSK receiver performance is investigated.

Figure 2.8 depicts the BEP as a function of the OSNR for 10 Gb/s OOK NRZ crosstalk signals, with the extinction ratio as a parameter. Figure 2.8 shows that the 40 Gb/s DQPSK optical receiver performance is practically independent of the extinction ratio of the interferer. The same conclusion has been found for the 40 Gb/s OOK interferer and is in agreement with the results presented in [3] for DPSK optical receivers.

2.4 Conclusions

In this work, the impact of in-band crosstalk due to multi-rate and multi-format interferers on the performance of 40 Gb/s DQPSK optical receivers has been assessed using MC simulation.

It has been shown that the 10 Gb/s OOK interferer, which is the traditional modulation format of optical communication systems, is the one that leads to the highest performance degradation of the 40 Gb/s DQPSK receiver. For a high number of interferers, slower bit rates, i.e., 10 Gb/s, on the crosstalk signals are the most detrimental to the receiver performance. The crosstalk induced by 40 Gb/s DPSK signals is the less harmful and is practically independent of the number of interferers.

It has been shown that the reduction of the duty-cycle of the interferers decreases the crosstalk impact on the receiver performance and that the influence of the OOK interferer extinction ratio on the DQPSK receiver performance is practically negligible.

Acknowledgments This work was supported by Instituto de Telecomunicações of Portugal within the project IXOS3D—PEst-OE/EEI/LA0008/2011.

References

1. J. Attard, J. Mitchell, C. Rasmussen, Performance analysis of interferometric noise due to unequally powered interferers in optical networks. J. Lightwave Technol. **23**(4), 1692–1703 (2005)
2. L. Cancela, J. Rebola, J. Pires, In-band crosstalk tolerance of direct detection DQPSK optical systems, in *IEEE Photonics Conference IPC* (Burlingame, California, USA, 2012)
3. L. Cancela, J. Rebola, J. Pires, Analytical assessment of the impact of OOK crosstalk signals on a DPSK direct detection system, in *Conference on Telecommunications Conftele* (Castelo Branco, Portugal, 2013)
4. N. Costa, A. Cartaxo, Optical DQPSK modulation performance evaluation, in *Book chapter in Advances in Lasers and Electro Optics, In-Tech* (2010), pp 427–452
5. M. Filer, S. Tibuleac, Impact of ROADM in-band Crosstalk on 40G DPSK signals, in *Conference of Optical Fiber Communication OFC* (San Diego, California, USA, 2010)
6. K. Ho, *Phase-Modulated Optical Communication Systems*, 1st edn. (Springer, New York, USA, 2005)
7. M. Jeruchim, P. Balaban, K. Shanmugan, *Simulation of Communication Systems—Modeling, Methodology and Techniques*, 2nd edn. (Kluwer Academic/Plenum Publishers, New York, USA, 2000)
8. I. Monroy, E. Tangdiongga, *Crosstalk in WDM Communication Networks*, 1st edn. (Kluwer Academic Publishers, New York, 2002)
9. A. Nag, M. Tornatore, B. Mukherjee, Optical network design with mixed line rates and multiple modulation formats. J. Lightwave Technol. **28**(4), 466–475 (2010)
10. J. Pires, L. Cancela, Estimating the performance of direct-detection DPSK in optical networking environments using eigenfunction expansion techniques. J. Lightwave Technol. **28** (13), 1994–2003 (2010)
11. N. Sambo, P. Castoldi, F. Cugini, G. Bottari, P. Iovanna, Toward high-rate and flexible optical networks. IEEE Commun. Mag. **50**(5), 66–72 (2012)
12. M. Seimetz, *High-Order Modulation for Optical Fiber Transmission*, 1st edn. (Springer, Berlin, 2009)
13. P. Winzer, M. Pfennigbauer, R. Essiambre, Coherent crosstalk in ultradense WDM systems. J. Lightwave Technol. **23**(4), 1734–1744 (2005)
14. P. Winzer, High-spectral-efficiency optical modulation formats. J. Lightwave Technol. **30**(24), 3824–3835 (2012)
15. T. Xia, S. Gringeri, M. Tomizawa, High capacity optical transport networks. IEEE Commun. Mag. **50**(11), 170–178 (2012)

Chapter 3
Insulation Quality Assessment of Transformers Using Laser Raman Spectroscopy

Toshihiro Somekawa, Makoto Kasaoka, Yoshitomo Nagano, Masayuki Fujita and Yasukazu Izawa

Abstract Transformers are very important components in electricity transmission and distribution networks. Its insulating oil sampling analysis, such as dissolved gas analysis, is generally used as a maintenance tool for determining transformer working condition, but requires time consuming preprocessing steps. Here, we propose an in-situ transformer health diagnosis technique without the need for oil sampling using laser Raman spectroscopy. In our method, degradation indicators present in oils are detected by direct laser irradiation into the oil. As an oil-specific degradation indicator, we demonstrated the Raman spectroscopic identification of C_2H_2 gas dissolved in oil. This technique was also capable of successful identification of CO and furfural—a paper-specific degradation indicator in oil samples. The results show that laser Raman spectroscopy is a useful alternative method for diagnoses of the transformer faults.

3.1 Introduction

Transformers are important components in any power system and their condition monitoring is essential for ensuring reliable operation of the system. In general, power transformer coils are insulated with a cellulose paper and immersed in mineral oil. Under the normal operating conditions, insulating mineral oils in the transformers include small amounts of gases, but failure of the transformer is known to be preceded by significant evolution of hydrogen (H_2), carbon monoxide (CO), carbon

---

T. Somekawa (✉) · M. Fujita · Y. Izawa
Institute for Laser Technology, 2-6 Yamadaoka, Suita, Osaka 565-0871, Japan
e-mail: somekawat@ile.osaka-u.ac.jp

M. Kasaoka · Y. Nagano
Kanden Engineering Corporation, 3-1-176 Fukuzaki, Minato-ku, Osaka 552-0013, Japan

M. Fujita · Y. Izawa
Institute of Laser Engineering, Osaka University, 2-6 Yamadaoka,
Suita, Osaka 565-0871, Japan

P.A. Ribeiro and M. Raposo (eds.), *Photoptics 2014*,
Springer Proceedings in Physics 177, DOI 10.1007/978-3-319-27321-1_3

dioxide (CO_2), methane (CH_4), ethane (C_2H_6), ethylene (C_2H_4), and acetylene (C_2H_2) gases caused by corona discharges, overheating, or arcing. Therefore, dissolved gas analysis (DGA) of the insulating oils has become the most widely used method for investigating incipient faults in transformers [1]. Dissolved gases extracted from oil aliquots due to pressure reduction or substitution by inert gases are measured by gas chromatography. In addition, it is known that furfural in oil comes only from the decomposition of insulation papers. So the furfural content in insulation oil is an important indicator for assessing the degradation of the insulating paper in transformer [2]. Furfural concentration in oil was generally extracted by methanol and measured by high performance liquid chromatograpy. These conventional methods usually offer sensitive detection limits at ppm levels that are suitable for monitoring the transformer conditions, but require time consuming preprocessing steps and include risks of sample contamination during sampling.

We recently reported detection of C_2H_2 dissolved in the insulation oil using laser Raman spectroscopy technique [3]. The C_2H_2 is mainly produced at very high temperatures that occur in presence of arcing. C_2H_2 is not detected in transformers during normal operation, but concentrations as high as 1 % are detected in presence of huge arcing [4]. Therefore, C_2H_2 is considered as an effective indicator. Our approach does not require gas separation in oils. The gas content in the insulating oil is directly measured by an irradiating laser. Based on this technique, on-line and in-situ detection of dissolved gases and byproduct materials can be adapted for diagnosis of transformer faults.

In this paper, we examined the applicability of our Raman spectroscopic technique as transformer health diagnosis tool for monitoring paper-specific indicators, CO and furfural. We found that Raman signals of CO ($\sim$2138 cm^{-1}) and furfural ($\sim$1705 cm^{-1}) can be detected with no interfering peaks from the insulating oil. Hence, Raman spectroscopy could be a useful technique for in-situ transformer health diagnosis without the need for oil sampling.

3.2 Experimental

3.2.1 Raman Spectroscopy

Figure 3.1 shows the schematic diagram of Raman spectroscopy. The laser was a standard Q-switched Nd:YAG laser (Continuum, Surelite: 10 ns pulse-width with 100 mJ pulse energy at 10 Hz repetition rate) operating at its second harmonic wavelength of 532 nm. A non-focused laser beam having about 8 mm diameter was used to avoid laser induced damage of the oil sample. The Raman signals from samples were collected using an achromatic lens at an angle of 25° from the forward direction of the laser beam. This design provides a longer optical path length than a conventional detection geometry at 90°, offering an order of magnitude increase in Raman scattering intensity. After passing through the edge and notch filters at 532 nm, the Raman signal is coupled into an optical fiber bundle by

Fig. 3.1 Schematic diagram of the experimental setup

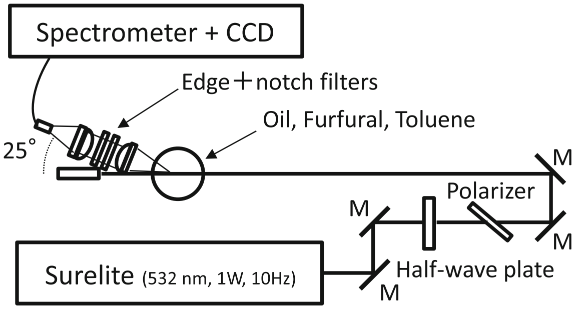

using an achromatic lens. The collected Raman signal is dispersed by a spectrometer (Acton, SpectraPro-2300i) with an entrance slit width set to 15 μm and detected with a liquid nitrogen-cooled charge-coupled device (CCD) camera (Princeton Instruments, SPEC-10). The exposure time was set at 90 ms. The spectra of C_2H_2, CO, and furfural were averaged over 3000 measurements. The spectral resolution of this system was estimated to be about 5 cm^{-1}.

3.2.2 *Sample Preparation*

The insulating oil used in this work was a mixture of naphthenic (41.6 %), paraffinic (50.0 %), and aromatic (8.4 %) oils. The used insulating oil samples were optically clear in the visible region. The insulating oils were stored in glass bottles with diameters of 3 cm. We confirmed that the glass bottles had no effect on Raman spectra. After complete degassing in vacuum for 4 h, the C_2H_2 and CO gases were introduced via a gastight syringe. The C_2H_2 concentrations of the samples under the investigation were measured by the gas chromatography and had 1.9, 5.7, and 10 % concentrations, respectively. The concentration of CO gas was about 10 %.

Furfural is only slightly soluble in this oil. Therefore, toluene solvent is added to oil. The concentration of toluene in oil was constant at approximately 9 % for quantitative analysis. Furfural used in this experiment becomes yellow on exposure to air and light, but the spectrum obtained using 532 nm excitation is not dominated by fluorescence.

3.3 Results and Discussion

3.3.1 *Raman Spectrum of Oil*

Figure 3.2a shows the Raman spectra of oil. In short and long edges of the spectrum, it exhibits numerous features that are specific to complex oil structures [3],

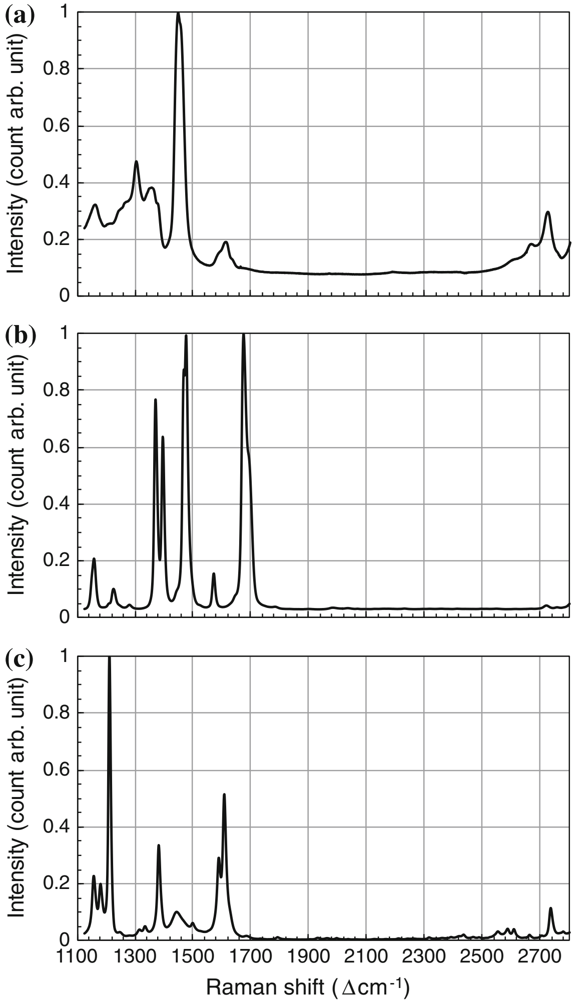

Fig. 3.2 Raman spectra of **a** oil, **b** furfural and **c** toluene

however, it has no large Raman spectral features and relatively low background baseline between 1700 and 2500 cm^{-1} range. The large peak centered at 1450 cm^{-1} corresponds to CH_3–CH_2 bending mode, and the set of peaks at 1302 and 1350 cm^{-1} corresponds to paraffin C–H twisting modes. The peak at 1610 cm^{-1} is due to an aromatic C=C stretching mode. The band at 2725 cm^{-1} can be assigned to the C–H stretching mode. In higher wavenumber side not shown here, the Raman spectrum of oil shows only C–H stretching mode around 3000 cm^{-1}, but no signals in the region between 3100 and 4200 cm^{-1}. Figures 3.2b and c show the Raman spectra of furfural and toluene, respectively, as discussed below.

3.3.2 Raman Spectra of C_2H_2 and CO Dissolved in Oil

Figure 3.3 shows the spectra of C_2H_2 gas at different concentrations and CO gas (~10 %) dissolved in the insulation oil. These Raman spectra were normalized at ~2191 cm^{-1}.

Weak Raman signals at ~2191 cm^{-1} were assigned to the oil-derived Raman signal since its peak intensity remained almost unchanged as the gas concentration increased in the oil.

In C_2H_2 dissolved in oil, Raman peak intensity of relatively sharp line at ~1972 cm^{-1} increased linearly versus increasing C_2H_2 concentration. We assign the peak around 1972 cm^{-1} to the CC stretching mode of C_2H_2 [5]. On the other hand, the band at 2138 cm^{-1} corresponds to the CO stretching mode. There are no large Raman bands from oil interfering with this signal. Thus, we found that CO gas is a promising candidate as a paper-specific degradation indicator, but the CO Raman signal is weak due to its small Raman scattering cross section [6].

Quantitative analysis in Raman spectroscopy was performed by using band intensity ratio calculations. This is because the Raman scattering intensity is a weak signal and the reproducibility of a Raman spectrum is degraded due to the variation in the excitation laser intensity and changes in the sample matrix. The oil-derived Raman signals at ~2191 cm^{-1} were used for these analyses. Figure 3.4 shows Raman peak intensity ratio, $I_{1972\ cm^{-1}}/I_{2191\ cm^{-1}}$, as a function of C_2H_2 concentration. The error bars were evaluated using the standard deviation of 10 consecutive spectra. The slope of the linear fit was 0.0825. Therefore, the C_2H_2 concentration can be determined by this slope and the Raman peak intensity ratio. Also, we estimated the detection limit of the present system to be $3\sigma_{C_2H_2} \sim 0.37$ %, where $\sigma_{C_2H_2}$ is the standard deviation of the Raman spectra from C_2H_2 free oil sample (0 %) in

Fig. 3.3 Raman spectra of C_2H_2 gas at different concentrations and CO gas dissolved in the insulation oil

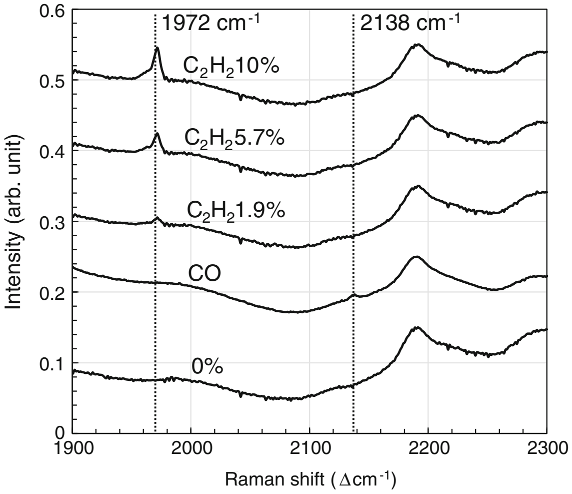

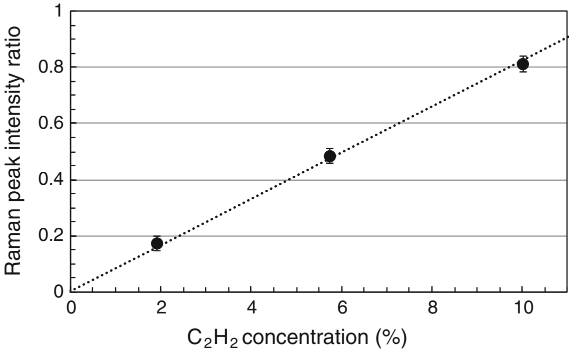

Fig. 3.4 Raman peak intensity ratio ($I_{1972\ \mathrm{cm}^{-1}}/I_{2191\ \mathrm{cm}^{-1}}$) as a function of dissolved C_2H_2 concentration in oil

1952–1977 cm^{-1} spectral range. Thus, the high C_2H_2 concentrations (~1 %) observed in actual insulating oils are detectable with current Raman system. On the other hand, the detection limits could be improved by using longer path length oil sample, higher average power CW laser, and more sensitive CCD detector.

3.3.3 Raman Spectrum of Furfural in Oil

Figure 3.2 shows the Raman spectra of (b) furfural and (c) toluene. The furfural Raman spectrum shows a H–C–C/O bending mode at 1372 cm^{-1}, C–C stretching mode at 1398 cm^{-1}, C=C stretching modes at 1478 and 1573 cm^{-1}, C=O stretching modes at 1675–1705 cm^{-1} [7]. As shown in Fig. 3.2c, the measured Raman spectrum of toluene includes no spectral interferences caused by Raman band overlap over ~1600 cm^{-1}. Detailed toluene mode assignments can be found elsewhere [8].

The furfural spectrum clearly shows an additional C=O stretching mode at 1675–1705 cm^{-1}, which is not found in oil. Thus, we can easily distinguish furfural from oil using this Raman band. Figure 3.5 shows Raman spectra of furfural at

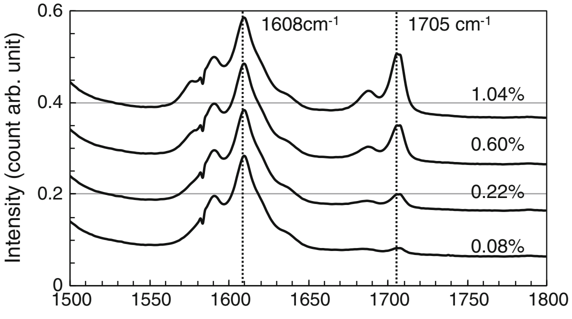

Fig. 3.5 Raman spectra of furfural at different concentrations in oil in the presence of toluene (~9 %) as a solvent

Fig. 3.6 Raman peak intensity ratio ($I_{1705\ \mathrm{cm}^{-1}}/I_{1608\ \mathrm{cm}^{-1}}$) as a function of furfural concentration in oil

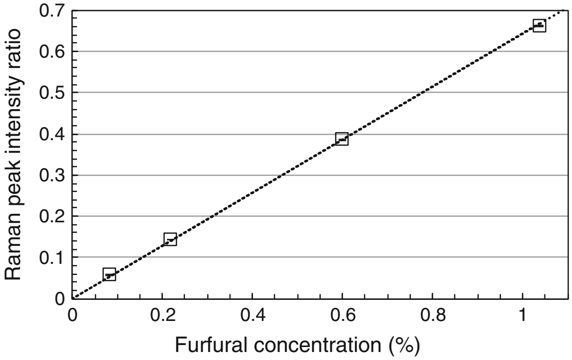

different concentrations in oil, in the presence of toluene (~9 %) as a solvent. Raman peak intensity at ~1705 cm^{-1} increased linearly versus increasing furfural concentration. The spectral shape differences between Figs. 3.2b and 3.5 can be observed at 1675–1705 cm^{-1}, which may be due to strong solvent interference [9].

Figure 3.6 shows Raman peak intensity ratios, ($I_{1705\ \mathrm{cm}^{-1}}/I_{1608\ \mathrm{cm}^{-1}}$), as a function of furfural concentration. It shows a linear dependence on the furfural concentration in contrast to the non-linear relationship between the Raman ratio ($I_{1687\ \mathrm{cm}^{-1}}/I_{1608\ \mathrm{cm}^{-1}}$) and furfural concentration. In this study, as a furfural-concentration-invariant signal, we chose the Raman peak of oil and toluene mixture at 1608 cm^{-1}. The error bars were evaluated using the standard deviation of 5 consecutive spectra and were hidden in the plot symbols. These ratios can be reasonably well fitted by a line with a slope of 0.643. We estimated also the detection limit of the present system to be $3\sigma_F \sim 65$ ppm, where σ_F is the standard deviation of the Raman spectra from 0.08 % furfural sample between 1720 and 1750 cm^{-1} range. However, the permissible concentrations of furfural in oil are 1.5 and 15 ppm at caution and danger levels, respectively [10]. Therefore, further development of the measurement system is needed to improve sensitivity.

3.4 Conclusions

We demonstrated in-situ application of Raman spectroscopy for detection of C_2H_2 and furfural in the insulating oil to diagnose the transformer health condition. Our method also has the advantage of simplicity, it is time saving and does not require sample preprocessing steps. In addition, the Raman spectroscopy could simultaneously monitor multi-trace gases and byproduct materials to get relevant information about the transformer condition. In future research, sensitivity improvements of our Raman spectroscopy system will be performed. We believe that it can be generally applied for assessing the transformer conditions.

In this work, we used clear and colorless oil samples. However, in actual field aged transformers, the oils are dark yellow or brown, which results in fluorescence emission by laser irradiation at 532 nm. Thus, the Raman signals are buried in fluorescence, and S/N ratio degrades. Therefore, to evaluate actual aging transformer working condition, we are taking two different approaches. First, in order to avoid fluorescence, we will use the longer wavelength laser as an excitation light source. And second, for obtaining Raman spectra from fluorescent samples, we plan to do time-resolved Raman signal detection by ICCD camera.

References

1. M. Duval, IEEE Electr. Insul. Mag. **5**, 22 (1989)
2. R.M. Morais, W.A. Mannheimer, M. Carballeira, J.C. Noualhaguet, IEEE Trans. Dielectr. Electr. Insul. **6**, 159 (1999)
3. T. Somekawa, M. Kasaoka, F. Kawachi, Y. Nagano, M. Fujita, Y. Izawa, Opt. Lett. **38**, 1086 (2013)
4. M. Duval, A. dePable, IEEE Electr. Insul. Mag. **17**, 31 (2001)
5. H. Fast, H.L. Welsh, J. Mol. Spectrosc. **41**, 203 (1972)
6. X. Li, Y. Xia, L. Zhan, J. Huang, Opt. Lett. **33**, 2143 (2008)
7. T. Kim, R.S. Assary, L.A. Curtiss, C.L. Marshall, P.C. Stair, J. Raman Spectrosc. **42**, 2069 (2011)
8. H.F. Hameka, J.O. Jensen, J. Mol. Struct. (Theochem) **362**, 325 (1996)
9. G. Allen, H.J. Bernstein, Can. J. Chem. **33**, 1055 (1955)
10. S. Okabe, G. Ueta, T. Tsuboi, IEEE Trans. Dielectr. Insul. **20**, 346 (2013)

Chapter 4
High Performance in Random Laser Using a Colloidal Suspension of TiO_2@Silica Nanoparticles

Ernesto Jimenez-Villar, Valdeci Mestre and Gilberto F. De Sá

Abstract A new scattering medium for random laser has been introduced. This random laser is composed of TiO_2@Silica nanoparticles suspended in an ethanol solution of rhodamine 6G. TiO_2 nanoparticles with average diameter of 0.41 μm were coated with a silica shell of ∼40 nm thickness. Random laser study comparing TiO_2 and TiO_2@Silica suspensions was performed. The study showed a higher performance for TiO_2@Silica system. This fact was attributed to an increase of the scattering strength (TiO_2@Silica) due to a better colloidal stability and light-coupling enhancement with TiO_2 scatter cores. Optical and chemical stability has been combined by coating TiO_2 nanoparticles with a silica shell of ∼40 nm thickness.

4.1 Introduction

The first evidence of random lasing (RLA) in solution was obtained by Lawandy et al. [1] who suspended TiO_2 nanoparticles (Np) in a conventional laser dye. RLA have been observed in a variety of gain media including GaN nanocolumns [2], dye-infiltrated opals [3], porous media infiltrated with liquid crystals with dyes [4], porous network of air into a solid glass or semiconductor crystal [5], ZnO scattering films and nanoclusters [6], on waveguided plasmonic [7] and many others. In the works reported by Noginov [8], Cao [9] and Wiersma [10] detailed reviews on random laser (RL) can be found.

E. Jimenez-Villar (✉) · G.F. De Sá
Departamento de Química Fundamental, Universidade Federal de Pernambuco, Recife,
PE 50670-901, Brazil
e-mail: ernesto.jimenez@uv.es

E. Jimenez-Villar
Instituto de Ciencia Molecular, Universitat de València, C/Catedrático José Beltrán Nº 2,
46980 Paterna, Valencia, Spain

V. Mestre
CCEA, Universidade Estadual da Paraíba, Patos, PB 58706-560, Brazil

P.A. Ribeiro and M. Raposo (eds.), *Photoptics 2014*,
Springer Proceedings in Physics 177, DOI 10.1007/978-3-319-27321-1_4

The strategy introduced by Lawandy, suspending highly scattering particles in laser dye has been repeated by other authors [11, 12], in order to study the random laser. However, the photodegradation effect and the inability to ensure complete colloidal dispersion, have limited the development and applications of such systems. The complete colloidal dispersion is related to a linear increase of the scattering surface with the suspended particles concentration. This is extremely difficult to obtain in solution at high concentrations, because particles tend to agglomerate [13]. The surface modification of TiO_2 Np with a silane-coupling agent has been used in order to reduce the agglomeration effect and improve the mechanical properties and UV protection of urethane clear coatings in TiO_2 composites [14]. Other authors have reported the replacement of the dispersive medium (TiO_2 Np) by silica Np [15], demonstrating random lasing. This kind of scattering medium greatly decreases the photodegradation effect. However, the relatively small difference in refractive index between silica and the alcohol-dye solution in comparison to TiO_2 causes a threshold increase and an efficiency decrease of the RL. In this work, we propose RLA with reduced photodegradation effect in an RL composed of TiO_2@Silica nanoparticles suspended in ethanol solution of rhodamine 6G (R6G). TiO_2 particles were coated with a silica shell of ~ 40 nm thickness. Particles like $TiO_2@SiO_2$ have already been synthesized before (over ten years back) [16], however, their application in RL has been done very recently [17, 18]. In this work, we have studied RLA and photodegradation effect for an extended range of pumping energy fluencies (between 0.12 and 264 mJ/cm^2). Additionally, we have studied the scattering strength of the TiO_2@Silica scattering medium and its relationship with the silica shell.

The silica shell with thickness around 40 nm presents a steric effect, preventing the “optical” junction of scattering TiO_2 surfaces. Moreover, this silica shell improves the light coupling with the TiO_2 particles by light refraction at the ethanol-silica interface. In addition, silica shell acts as a barrier to prevent the charge transfer, which is the principal cause of the dye degradation [19]. These have been practical difficulties for the development of RL and novel optical devices with improved performance and functionality. In turn, the silica coating is particularly advantageous due to its high dispersibility [20, 21], low density, and the inertness of nanoparticles [22, 23] along with the numerous possibilities for their use [24–27].

4.2 Experimental Section

4.2.1 Chemical Synthesis and Characterization

R6G laser dye ($C_{28}H_{31}N_2O_3Cl$) with molecular weight 479.02 g/mol supplied by Fluka: Ethanol alcohol (C_2H_5OH) with spectroscopic grade purity supplied by Alphatec: Tetra-ethyl-ortho-silicate (TEOS) supplied by Sigma-Aldrich. Titanium dioxide (TiO_2 Np; diameter 410 nm) of rutile crystal structure was acquired from DuPont Inc (R900).

Two kinds of samples were prepared containing [1×10^{-4} M] of Rhodamine 6G (R6G), one with TiO_2 and another with TiO_2@Silica scatters Np. The silica coating of TiO_2 Np was made via Stöber method [28, 29]. In the first stage 2 g of TiO_2 Np were dispersed in 250 ml of absolute ethanol by ultrasound bath for 20 min. Then, the solution of TiO_2 Np was divided into two equal portions of 125 ml. One of the parts was placed in a bath at 5 °C and 1.1 ml of TEOS, previously diluted in 11 ml of ethanol, was added. The 10 % diluted solution of TEOS was added in 110 portions of 100 µl during the course of 1 h. The solution was stirred during the TEOS addition and after it was stored during 4 week at room temperature. The other portion was stored and used as a reference in every experiment.

The silica coating on the TiO_2 Np were examined by transmission electron microscopy (TEM), performed on a 100 kV JEOL, model 1200EX, microscope. The commercial carbon-coated Cu TEM grid was immersed in the solution of TiO_2@Silica Np previously diluted 50-fold lower and then left to dry before being introduced into the microscope. The stoichiometric ratio (Ti/Si) of nanoparticles (TiO_2@Silica) was determined by Energy Dispersive X-ray fluorescence (ED-XRF) using an X-ray spectrometer SIEMENS D5000. The sample was prepared in three steps; precipitation, washing and drying. The nanoparticles powder (TiO_2@Silica) was pressed into a tablet form of a 12 mm diameter for analysis.

4.2.2 Experimental Setup of Random Laser

Figure 4.1c, d show the schematic diagrams of the RL experimental setup and transmission experiment, respectively. The laser system was the second harmonic of a *Q*-switched Nd: YAG Continuum Minilite II (25 mJ, $\lambda = 532$ nm, with a pulse width of ~4 ns, repetition rate up to 15 Hz, and spot size of 3 mm). The laser power was regulated through neutral density filters (NDF), a polarizer and a half wave plate. For RLA study, the samples were accommodated in a 2 mm pathlength quartz cuvette. The pump laser beam was incident upon the sample at ~15°. The emission spectra were collected through a multimode optical fiber (200 µm) coupled to a spectrometer HR4000 UV-VIS (Ocean Optics) with 0.36 nm spectral resolution (FWHM). The collection angle (optical fiber) was ~45° with respect to the incident pumping beam, that is, 60° with respect to the cuvette surface. The liquid samples were placed in an ultrasound bath for about 10 min before recording the spectrum, in order to obtain the same dispersion of nanoparticles (initial conditions) in all measurements. For transmission experiment, the transmitted coherent intensity I_{TC} was determined as a function of slab thickness: the same laser beam (*Q*-switched Nd:YAG Continuum Minilite II, $\lambda = 532$ nm), attenuated 10^3 times by neutral density filters 1 µJ, was passed through a positive lens L_1 (200 mm focal length) so as to obtain the focus with its waist near the pinhole PH_1 (600 µm diameter). The cell consisted of two optical flat F in wedge form, in this way; the

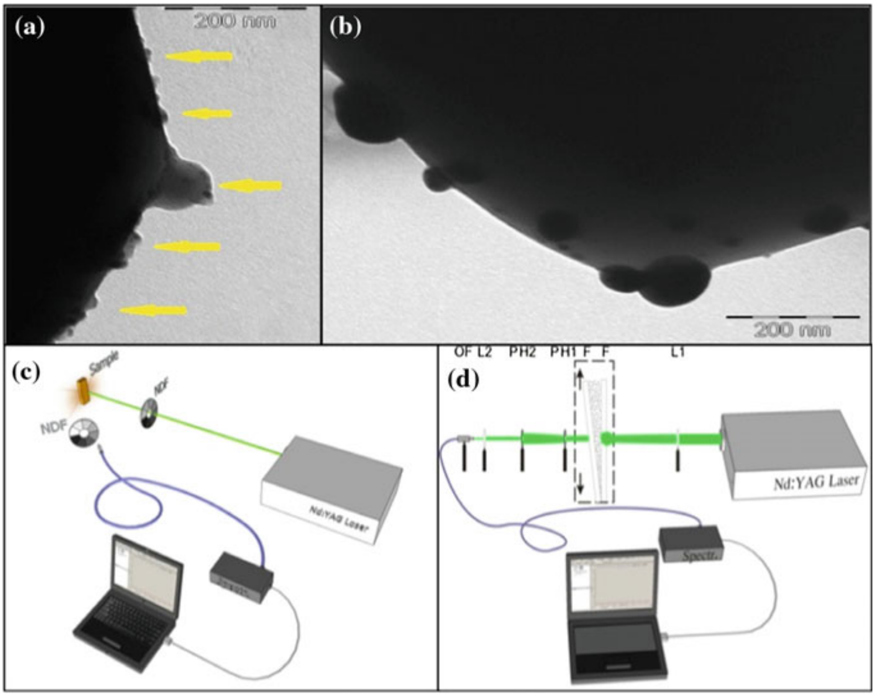

Fig. 4.1 TEM images of; **a** silica coating on the TiO_2@Silica surface and **b** TiO_2 nanoparticle surface. The scale bars represent 200 nm. *Yellow arrows* (**a**) indicate the silica coating. **c**–**d** Schematic diagrams for RL experimental setup and transmission experiment (ballistic), respectively

slab thickness depends on the incidence point of the cell. Another pinhole, PH_2 (1200 μm diameter), was positioned 80 mm away to PH_1 in order to reduce the diffuse light. Yet another lens, L_2 (50 mm focal length), allowed for focalization on the optical fiber (200 μm).

4.3 Results and Discussion

4.3.1 Silica Shell onto TiO_2 Nanoparticles

In TEM images (Fig. 4.1a) we observe the silica coating on TiO_2 Np, such as the one indicated by the yellow arrows. This silica shell presents an irregular morphology with a thickness ranging between 20 and 70 nm. Figure 4.1b shows the surface of one TiO_2 Np, before the coating with silica. As can be seen, the Np surface is irregular; this fact should determine the morphology of the silica coating subsequently. The mass percentage ratio (Ti/Si) determined by ED-XRF was Ti_{70}/Si_{30}.

The average thickness of silica coating, calculated from the typical silica density obtained by the TEOS hydrolysis 2.1 g/cm^3 [30], was ~40 nm. In this way, the silica shell represents a barrier that prevents the "optical" binding of TiO_2 scattering surfaces, with the additional advantage to present a chemically stable surface (SiO_2).

4.3.2 Random Laser Action

Figure 4.2a, b show the behavior of the emitted intensity and the spectral width (FWHM), as a function of pumping energy fluencies for the two kind of scattering medium (TiO_2 and TiO_2@Silica). The RL action for pumping energy fluencies between 0.12 and 264 mJ/cm^2 were performed. The calculated concentrations of scatters Np and dye were 5.6×10^{10} Np/ml and 1×10^{-4} M, respectively. Each value of emission intensity and bandwidth represented in the graphs (Fig. 4.2a, b)

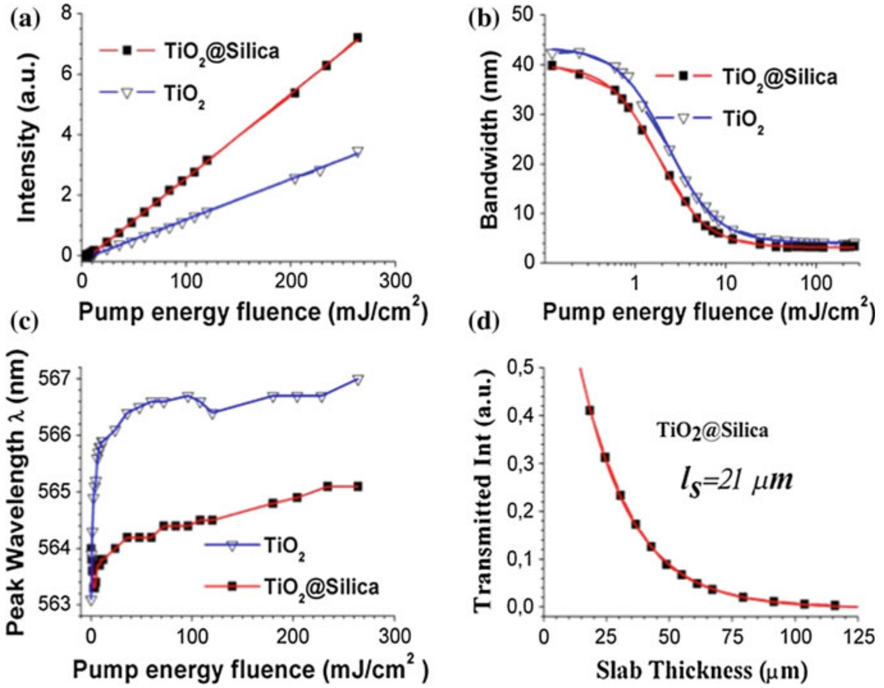

Fig. 4.2 **a** The emitted peak intensity and **b** spectral FWHM emission of the RL, for the two kinds of nanoparticles (TiO_2 and TiO_2@Silica). The *solid lines* represent the fits with experiments points; *blue* and *red lines* correspond to the TiO_2 and TiO_2@Silica systems, respectively. **c** Influence of the pump energy fluence on peak wavelength of emission spectrums for TiO_2 and TiO_2@Silica systems. **d** Typical transmission curve for TiO_2@Silica system. l_s represents the scattering mean free path

was taken by integrating 10 laser pulses, which allowed us to rule out any photodegradation effects during the measurement. As observed, the RL action for TiO_2@Silica system is improved, i.e. presented higher slope efficiency, narrower bandwidth and lower laser threshold. For the TiO_2@Silica system, the RL efficiency slope (RL_{eff}) was ~2.1 times greater than for TiO_2.

The RL threshold values extracted from the fittings (inflection points, Fig. 4.2b) for TiO_2 and TiO_2@Silica systems were 2.29 ± 0.04 and 1.79 ± 0.02 mJ/cm^2, respectively.

The peak position of the emission spectrum was measured as a function of the pumping energy fluence (between 0.12 and 260 mJ/cm^2). Figure 4.2c shows a comparison of these peak positions with fluence for the TiO_2@Silica and TiO_2 systems. The emission spectrum shows a redshift for the TiO_2 system, which undergoes a large increase in fluencies between 0.12 and 12 mJ/cm^2 (0–2.8 nm). This redshift increases (between 3 and 3.9 nm) for fluencies >12 mJ/cm^2. Instead, the emission spectrum peak for TiO_2@Silica system shows a blueshift for fluencies ≤12 mJ/cm^2. For fluencies between 12 and 260 mJ/cm^2, the redshift increases in the same fashion, from 0 up to ~1 nm. The shift was previously observed and explained by a model considering absorption and emission at the transition between the ground and the first excited singlet of the dye molecule [31]. In this way, the redshift must be determined by the ratio between R6G molecules and R6G molecules involved in the stimulated emission. Therefore, it can be inferred that the percentage of R6G molecules involved in the stimulated emission is higher for the TiO_2@Silica system. The above results could be explained by the increase of scattering strength due to the better "optical" colloidal stability (OCS) and light-coupling enhancement (LCE) with TiO_2 scattering cores provided by the silica shell [17, 18]. For the TiO_2@Silica and TiO_2 systems, we have determined l_s from the transmission experiment [32]. The transmitted coherent intensity was measured as a function of slab thickness. This must show an exponential decay (linear in log scale). The l_s values can be determined from slopes. Typical transmission curve for TiO_2@Silica system is showed in the Fig. 4.2d. The l_s values measured from transmission experiment were 21 and 52 μm for TiO_2@Silica and TiO_2 systems, respectively. The l_s value calculated by Mie theory for a TiO_2 particles (0.41 μm diameter) suspension (in ethanol) at [5.6×10^{10} NPs/ml] is ~40 μm, which is lower than TiO_2 (52 μm) and higher than TiO_2@Silica (21 μm). Therefore, the scattering strength increase must be associated with both effects, OCS improving and LCE (TiO cores) provided by the silica shell. A higher scattering strength means that the pumping energy is confined in a lower volume (higher effective pumping fluence). Moreover, the amount of R6G molecules inside this volume would be lower, exciting a higher percent of molecules (higher population inversion). In turn, a higher efficiency of the RL must be expected for TiO_2@Silica system. Notice that, the volume of emission laser should increase with pumping fluence (I_{P0}). The pumping fluence at a depth length l inside the scattering medium (I_{Pl}) could be expressed as follows:

$$I_{Pl} = I_{P0}e^{-l/\sqrt{l_s \times l_a}} \quad (4.1)$$

l_a is the ballistic absorption length. The decay behavior of diffuse intensity has been neglected.

Therefore, there would be a limit depth length (l_{Th}) inside the scattering medium, beyond which the pumping intensity (I_{PTh}) is unable to provoke population inversion. The l_{Th} should depend on the pumping fluence I_{P0} as follows:

$$I_{PT} = I_{P0}e^{-l_{Th}/\sqrt{l_s \times l_a}} \rightarrow l_{Th} = \sqrt{l_s \times l_a} * (\ln I_{P0} - \ln I_{PTh}) \quad (4.2)$$

I_{PTh} would correspond with the RL threshold fluence. Therefore, for $I_{P0} \gg I_{PTh}$ then l_{Th} is directly proportional to $(l_s)^{1/2}$. In turn, the effective pumping intensity into the RL emission region is inversely proportional to $(l_s)^{1/2}$, so, it is higher for TiO_2@Silica system.

Figure 4.3 shows a representative scheme of RL scattering medium consisting of light interaction with a TiO_2@Silica Nps suspension. The silica shell avoids the contact between TiO_2 scattering surfaces and improves the light coupling with TiO_2 cores, which leads to a higher effective scattering surface and consequently to an increase of scattering strength.

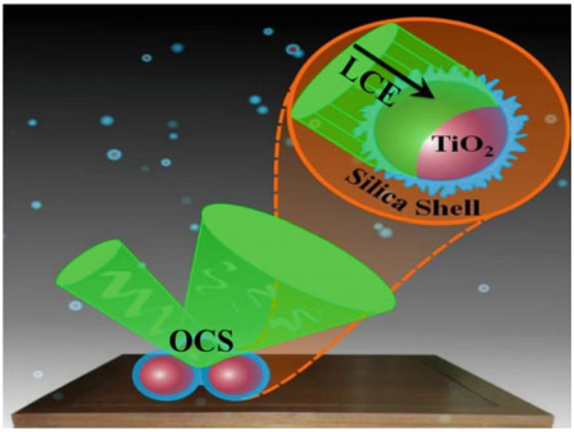

Fig. 4.3 Representative scheme of RL scattering medium, it consists of a TiO_2@Silica Nps suspension. The *blue* coating represents the silica shell on the TiO_2 Nps and the *red spheres* correspond to the TiO_2 cores. The silica shell between two TiO_2 cores avoids the contact between those and also improves the light coupling, which leads to a increase of the scattering strength

4.3.3 Photodegradation Study

Figure 4.4 shows the photodegradation process by the RL emission intensity as a function of shots number for systems TiO_2@Silica (a) and TiO_2 (b). The laser beam of 3 mm diameter and fluencies of 200 and 260 mJ/cm^2, was used to pump the samples, which volume was 200 μl accommodated in a 2 mm pathlength quartz cuvette. Figure 4.3a, b show a decrease in emission intensity (RL) with the number of shots for the pumping fluencies 200 mJ/cm^2 (grey) and 260 mJ/cm^2 (black). The TiO_2 system shows a rapid exponential decay. The number of shots for which the emission intensity decreases to 50 % for the fluencies of 200 and 260 mJ/cm^2 was 960 and 342, respectively. However, for the TiO_2@Silica system the number of shots required were much higher, 59077 (200 mJ/cm^2) and 26010 (260 mJ/cm^2), respectively. These represent a decrease in the photodegradation rate more than 60 times (200 mJ/cm^2) and 74 times (260 mJ/cm^2), respectively.

The TiO_2 photocatalytic properties are a well studied subject, which has been used to remove or degrade dyes from the environment [33]. The photocatalytic pathway involves a reaction on the TiO_2 surface following several steps: (1) photogeneration of electron–hole pairs by exciting the semiconductor with >3.2 eV light; (2) separation of electrons and holes by traps existing on the TiO_2 surface; (3) a redox process induced by the separated electrons and holes with the adsorbates present on the surface.

The exponential decrease of the RL intensity, for the system TiO_2, indicates that the photodegradation is proportional to its derivative, as to the photodegradation rate. This means that the charge transfers [34] and therefore the redox reaction [35] will cause a greater charge transfer in the next laser shot. Thus, one might think that the high concentrations of charges created by the TiO_2 nanoparticles at high pumping fluencies must react with the proper surface of the nanoparticles, reducing Ti^{4+} and oxidizing O^{2-}. This process results in oxygen vacancies [36], which act as traps for photoelectrons. These electrons, trapped near the surface, act as a source of electron transfer coming from these superficial traps, increasing the efficiency of the

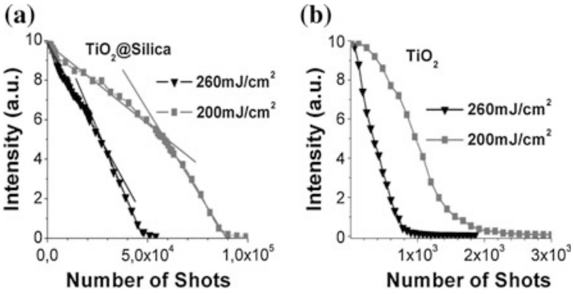

Fig. 4.4 Photodegradation process of Random laser action as a function of the number of shots for the laser pumping fluencies of 200 mJ/cm^2 (*grey*) and 260 mJ/cm^2 (*black*): **a** TiO_2@Silica Np system; **b** TiO_2 Np system

redox process [37]. Additionally, the creation of oxygen vacancies in TiO_2 causes a progressive decreasing of gap on the nanoparticle surfaces (TiO_2), which is reflected in the progressive increase in the creation of electron–hole pairs. This photo-darkening effect is observed in films of TiO_2 exposed to successive irradiation of laser pulses [38, 39].

The photodegradation process for the TiO_2@Silica system presents a linear behaviour. However, the modulus of the slope increases slightly after the emission intensity decreases to ~50 %. Subsequently, the photodegradation rate experiences a slight increase, but remains constant. This phenomenon could be due to the decreased absorption of R6G, provoking an increase of the effective pumping fluence inside the scattering medium (TiO_2@Silica), which should increase the photodegradation rate of R6G.

The photodegradation process (RL) for the system TiO_2@Silica could be explained through the reaction of the ethanol radical CH_3CHOH with R6G ground state molecules [40]. The free radical CH_3CHOH is produced by energy transfer from the R6G molecules in a higher triplet state, which is produced by two sequential single-photon absorptions [41]. This photodegradation process is much less effective, since it does not involve charges transfer from the TiO_2 nanoparticles, which is known as an efficient photocatalyzers.

4.4 Conclusions

The RL action using a novel scattering media composed by titanium oxide Np coated with ~ 40 nm thickness of silica shell was studied. This scattering medium (TiO_2@Silica Np) combines the high refractive index of TiO_2 with chemical inertness, "optical" colloidal stability and light coupling enhancement (TiO_2 cores) provided by the silica shell. Random lasing with higher efficiency, lower threshold, narrower bandwidth and very long photo-bleaching lifetime was obtained. The RL efficiency was 2.1 times higher and the R6G photodegradation period was between 60 and 74 times higher than the conventional scattering medium (TiO_2). The high RL efficiency was ascribed to lower l_s for TiO_2@Silica system. This fact is associated with the silica shell, which avoid the "optical" junction of TiO_2 scattering surface and improves the light coupling with TiO_2 cores. In other words, the core-shell scattering particles present a core with high refractive index (TiO_2) and a shell that combines high chemical stability, light coupling enhancement (TiO_2 cores) and a steric "optical" effect. Therefore, a lower l_s provokes higher effective pumping fluence, leading to higher population inversion and stimulated emission rate. In this way, it has been remarked the colloidal stability of the scattering medium, which is an important parameter and is not insignificant for the treatment of RL.

The lower photodegradation period was associated to the higher chemical stability provided by the silica shell, which must establish a potential barrier for the charge transfer.

Acknowledgments We gratefully acknowledge financial support from Rede 36 Nanobiotec CAPES (Brazil). V.M. thanks the CAPES (Brazil) for doctoral fellowships.

References

1. N.M. Lawandy, R.M. Balachandran, A.S.L. Gomes, E. Sauvain, Nature **368**, 436–438 (1994)
2. M. Sakai, Y. Inose, K. Ema, T. Ohtsuki, H. Sekiguchi, A. Kikuchi, K. Kishino, Appl. Phys. Lett. **97**, 151109 (2010)
3. M.N. Shkunov, M.C. DeLong, M.E. Raikh, Z.V. Vardeny, A.A. Zakhidov, R.H. Baughman, Synth. Met. **116**, 485–491 (2001)
4. D. Wiersma, S. Cavalier, Nature **414**, 708–709 (2001)
5. F.J.P. Schuurmans, D. Vanmaekelbergh, J. van de Lagemaat, A. Lagendijk, Science **284**, 141–143 (1999)
6. H. Cao, Y. Ling, J.Y. Xu, C.Q. Cao, P. Kumar, Phys. Rev. Lett. **86**, 4524–4527 (2001)
7. T. Zhai, X. Zhang, Z. Pang, X. Su, H. Liu, S. Feng, L. Wang, Nano Lett. **11**(10), 4295–4298 (2011)
8. M.A. Noginov, *Solid-State Random Lasers (Springer Series in Optical Sciences)* (Norfolk State University, Norfolk, 2005)
9. H. Cao, J. Phys. A: Math. Gen. **38**, 10497–10535 (2005)
10. D.S. Wiersma, Nat. Phys. **4**, 359–367 (2008)
11. M.A. Noginov, H.J. Caulfield, N.E. Noginova, P. Venkateswarlu, Opt. Commun. **118**, 430–437 (1995)
12. M. Leonetti, C. Conti, C. Lopez, Appl. Phys. Lett. **101**, 051104 (2012)
13. N. Mandzy, E. Grulke, T. Druffel, Powder Technol. **160**, 121–126 (2005)
14. M. Sabzi, S.M. Mirabedini, J. Zohuriaan-Mehr, M. Atai, Prog. Org. Coat. **65**, 222–228 (2009)
15. A.M. Brito-Silva, A. Galembeck, A.S.L. Gomes, A. Jesus-Silva J, C.B. de Araújo, J. Appl. Phys. **108**, 033508 (2010)
16. J.N. Ryan, M. Elimelech, J.L. Baeseman, R.D. Magelky, Environ. Sci. Technol. **34**, 2000–2005 (2000)
17. E. Jimenez-Villar, V. Mestre, P.C. de Oliveira, G.F. de Sá, Nanoscale **5**, 12512–12517 (2013)
18. E. Jimenez-Villar, V. Mestre, P.C. de Oliveira, W.M. Faustino, D.S. Silva, Gilberto F. de Sá, Appl. Phys. Lett. **104**, 081909 (2014)
19. M.A. Fox, M.T. Dulay, Chem. Rev. **93**, 341 (1993)
20. E. Jimenez, K. Abderrafi, J. Martınez-Pastor, R. Abargues, J.L. Valdes, R. Ibañez, Superlattices Microstruct. **43**, 487–493 (2008)
21. E. Jimenez, K. Abderrafi, R. Abargues, J.L. Valdes, J.P. Martınez-Pastor, Langmuir **26**(10), 7458–7463 (2010)
22. G. Fuertes, O.L. Sanchez-Munoz, E. Pedrueza, K. Abderrafi, J. Salgado, E. Jimenez, Langmuir **27**, 2826–2833 (2011)
23. G. Fuertes, E. Pedrueza, K. Abderrafi, R. Abargues, O. Sánchez, J. Martínez-Pastor, J. Salgado, E. Jiménez, in *Proceedings of SPIE Medical Laser Applications and Laser-Tissue Interactions* V, 8092, 80921M (2011)
24. E. Rodríguez, E. Jimenez, A.A.R. Neves, L.A. Padilha, G.J. Jacob, C.L. Cesar, L.C. Barbosa, Appl. Phys. Lett. **86**(11), 113117 (2005)
25. E. Rodriguez, E. Jimenez, G.J. Jacob, A.A.R. Neves, C.L. Cesar, L.C. Barbosa, Physica E **26**, 361 (2005)
26. E. Rodriquez, G. Kellerman, E. Jiménez, C.L. César, L.C. Barbosa, Superlattices Microstruct. **43**(5–6), 626–634 (2008)
27. G. Kellermann, E. Rodriguez, E. Jimenez, C.L. Cesar, L.C. Barbosa, C. Aldo Felix, J. Appl. Crystallogr. **43**, 385–393 (2010)
28. W. Stöber, A. Fink, E. Bohn, J. Colloid Interface Sci. **26**, 62 (1968)

29. A. Kamal, E. Jimenez, T. Ben, S.I. Molina, R. Ibáñez, V. Chirvony, J.P. Martínez-Pastor, J. Nanosci. Nanotechnol. **12**(8), 6774–6778 (2012)
30. B. Karmakar, G. De, D. Ganguli, J. Non-Cryst. Solids **272**, 119–126 (2000)
31. M.A. Noginov, H.J. Caulfield, N.E. Noginova, P. Venkateswarlu, Opt. Commun. **118**, 430–437 (1995)
32. M.B. van der Mark, M.P. van Albada, A. Lagendijk, Phys. Rev. B **37**(7), 3575–3592 (1998)
33. G. van Wold, Chem. Mater. **5**, 280 (1993)
34. A.L. Linsebigler, L. Guangquan, J.T. Yates Jr., Chem. Rev. **95**, 735–758 (1995)
35. N. Serpone, E. Pelizzetti, *Photocatalysis-Fundamentals and Applications*, ed. by H. van Damme Chapter 7, Supports in Photocatalysis (Wiley, New York, 1989)
36. M. Tsukamoto, N. Abe, Y. Soga, M. Yoshida, H. Nakano, M. Fujita, J. Akedo, Appl. Phys. A **93**, 193–196 (2008)
37. H. Ceriscber, A. Heller, J. Phys. Chem. **95**(13), 5261 (1991)
38. M. Tsukamoto, T. Shinonaga, M. Takahashi, M. Fujita, N. Abe, Transa. JWRI, **40**(1), 21–23 (2011)
39. M. Tsukamoto, N. Abe, Y. Soga, M. Yoshida, H. Nakano, M. Fujita, J. Akedo, Appl. Phys. A **93**, 193–196 (2008)
40. A. Dunne, M.F. Quinn, J. Chem. Soc., Faraday Trans. 1 **72**, 2289–2295 (1976)
41. M. Yamashita, H. Kashiwagi, IEEE J. Quant. Electron. **12**(1), 90–95 (1976)

Chapter 5
Gamma-Ray Dose-Rate Dependence on Radiation Resistance of Specialty Optical Fiber with Inner Cladding Layers

Seongmin Ju, Youngwoong Kim, Seongmook Jeong, Jong-Yeol Kim, Nam-Ho Lee, Hyun-Kyu Jung and Won-Taek Han

Abstract A germano-silicate glass optical fiber with inner cladding layers of pure silica buffer and boron-doped silica was fabricated to enhance photosensitivity of fiber Bragg grating (FBG) maintaining the radiation resistance for sensing applications. The gamma-ray dose-rate dependence on the radiation-induced attenuation (RIA) and the peak shift of the FBG inscribed in the core of the fiber was investigated. As the γ-ray irradiation on the fiber with the FBG increased to 22.86 kGy/h, the reflected peak power increased together with small temperature increase but the transmitted power at 1550 nm decreased. While the Bragg reflection wavelengths were shifted toward longer wavelengths during the γ-ray irradiation, the FWHM bandwidth remained unchanged. The Bragg peak shift of the FBG was found to saturate at a 78 pm level and the RIA of 1.345 dB/m at 1550 nm was obtained with the accumulated dose-rate of 22.86 kGy/h.

5.1 Introduction

A real-time monitoring sensor system for stable usage of nuclear power based on a fiber-optic technology have drawn renewed attention because the leaking radiation from nuclear power plants caused by accident is emerging as a serious social problem [1]. The optical fiber Bragg grating (FBG) sensor is seeking applications in

---

S. Ju · Y. Kim · S. Jeong · W.-T. Han (✉)
School of Information and Communications/Department of Physics and Photon Science, Gwangju Institute of Science and Technology, 123 Cheomdangwagi-ro, Buk-gu, Gwangju, Republic of Korea
e-mail: wthan@gist.ac.kr

S. Ju
e-mail: jusm@gist.ac.kr

J.-Y. Kim · N.-H. Lee · H.-K. Jung
Nuclear Convergence Technology Development Department, Korea Atomic Energy Research Institute, 989-111 Daedeok-Daero, Yuseong-gu, Daejeon, Republic of Korea

P.A. Ribeiro and M. Raposo (eds.), *Photoptics 2014*,
Springer Proceedings in Physics 177, DOI 10.1007/978-3-319-27321-1_5

the fields of the nuclear reactor and nuclear power plant in harsh nuclear environments, mainly due to the advantages of remote metering, intrinsic safety, high sensitivity, fast response, electromagnetic interferences (EMI) immunity, lightweight, multiplexing capabilities, and durability. However, the effect of radiation on the FBG written in the optical fiber is well-known to be an increase of the transmission loss and the shift of the Bragg peak wavelength [2–6]. Regarding the radiation effect on transmission, the signal transmission loss increased due to the formation of radiation-induced defects and color centers [4, 5, 7, 8]. The radiation-resistant optical fibers including pure silica core fiber, fluorine doped silica core fiber, and OH doped silica core fiber have been reported [5, 7–13]. The radiation resistance of optical fibers is dependent on the glass composition, especially with dopants, by reducing the non-bridging oxygen hole center (NBOHC) and blocking the formation of E′ center in SiO_2 glass [7, 8, 12]. Also, by decreasing the residual stress in the fiber core or defects at the interface of the core and the cladding, the radiation resistance can be increased due to the small number of defect centers such as NBOHC or E′ center [11].

As for the Bragg peak wavelength shift of the FBG under radiation, the reported shift values varied from tens to several hundreds of pico-meters for a dose in the 100 kGy range [2, 3, 6]. The direction of the Bragg peak shift depended on dopants in the optical fiber core region due to its effect on refractive index change [5, 6] and thus it is probably not linked to the inscription of the FBG but is a property of the fiber. Thus the FBG based sensor is insensitive to radiation-induced loss because the information on the measured parameters such as temperature, bend, or strain is wavelength-encoded [14]. However, when the fiber is exposed under high dose irradiation, the Bragg resonance or the transmission is highly attenuated and the resonance wavelength is hard to define. Therefore, the radiation resistant optical fiber is a key component for the optical fiber temperature sensors based on the FBG under gamma-ray radiation. However, the reported radiation-resistant optical fiber based on pure silica core glass, which does not incorporate Ge in the fiber core for enhancing the radiation resistance, has limitation to use as an optical fiber sensor probe based on the FBG because of its low photosensitivity [11].

In this paper, therefore, we fabricated the germano-silicate glass optical fiber employing two inner cladding layers of a pure silica buffer and boron-doped silica to enhance photosensitivity for fiber Bragg grating (FBG) maintaining the radiation resistance for sensing applications. The gamma-ray dose-rate dependence on the radiation-induced attenuation (RIA) and the peak shift of the FBG inscribed in the core of the fiber was investigated.

5.2 Experimental Procedure

The germano-silicate glass optical fiber preform with two inner cladding layers of a pure silica buffer and boron-doped silica was fabricated by using the modified chemical vapor deposition (MCVD) process. BCl_3 gas was added with $SiCl_4$ during the MCVD process to incorporate boron oxide in the inner cladding region in order to make a depressed-index layer. Then the silica glass tube with depressed-index inner cladding layer was collapsed and jacketed with the germano-silicate glass core rod with pure silica buffer cladding layer. To decrease possible residual stress in the fiber core or defects at the interface of the core and the cladding due to their different volume expansions, a buffer layer of a pure silica glass was made between the core and the inner cladding. The index profile of the fiber preform is shown in Fig. 5.1. Finally, the preform was drawn into a fiber with outer diameter of 125 μm using the draw tower at 2150 °C. The core diameter and the cut-off wavelength of the fiber with pure silica buffer cladding layer and boron-doped depressed-index inner cladding layer (fiber 1) were 8.30 μm and 1208 nm, respectively. The length of the buffer layer between the core and the depressed-index inner cladding layer was 11.16 μm and the width of the depressed-index layer was 8.93 μm. The refractive index differences between the core and the buffer layer (Δn_{core}) and between the buffer layer and the depressed-index inner cladding layer ($\Delta n_{depressed\text{-}index}$) were 0.0050 and −0.0035, respectively, as shown in Fig. 5.1. For a comparison, a commercial single-mode fiber without any inner cladding layers (fiber 2) was also used as a reference. The core diameter and the cut-off wavelength of the fiber 2 were 9.5 μm and 1190 nm, respectively. The transmission losses of the fiber 1 and the fiber 2 at 1550 nm were 4.8 and 2.7 dB/km, respectively, as shown in Fig. 5.2. The optical attenuation was measured by a cut-back method using the optical spectrum analyzer (OSA, Ando AQ6317B) with the white light source (Ando AQ4303B) for launching the input broadband light. The absorption peaks

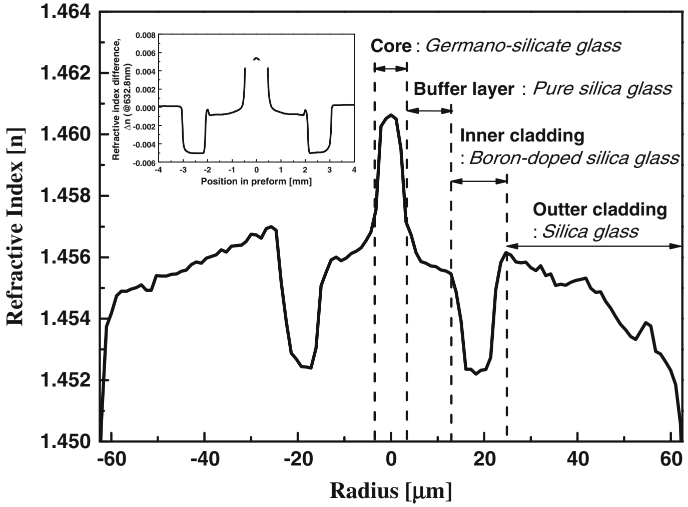

Fig. 5.1 The refractive index profile of the germano-silicate glass optical fiber with two inner cladding layers of a pure silica buffer and boron-doped silica (*Inset* optical fiber preform)

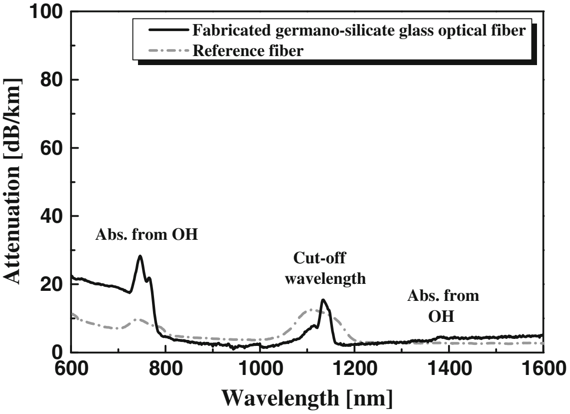

Fig. 5.2 Attenuation spectra of the fabricated germano-silicate glass optical fiber and the reference fiber

appeared at around 1100 nm were from cut-off wavelength of both fibers. The extra absorption peaks shown at 740 and 1380 nm in fibers were due to the presence of OH ion impurities [15].

Using the fabricated optical fiber (fiber 1), the optical fiber sensor probe based on FBG was made. To facilitate the FBG formation by increasing photosensitivity of the fibers, the hydrogen loading process was carried for the fibers 1 and 2 under the pressure of 100 bars at room temperature for 96 h. Note that the fibers 1 and 2 were pre-irradiated under γ-ray @ 7.20 kGy before FBG inscription. FBGs were written on the stripped portion of the fibers by using a phase mask (Pitch No. 1071.2, QPS Photronics Inc.) with a KrF excimer laser (248 nm) near 1550 nm. The fibers were then annealed at 80 °C for 10 h to release weak photo-induced changes from hydrogen molecules penetrated in the optical fiber core during the hydrogen loading process [16, 17]. Then the fibers were recoated with acrylate polymer and cured with UV light. The dose-rate dependent characteristics of the fibers with the FBG on RIA and FBG properties under gamma-ray radiation was measured by using the optical spectrum analyzer (OSA, Ando AQ6317B) together with the amplified spontaneous emission source (ASE source, Optoware-B200) operating around 1550 nm as an input light source. The fibers with the FBG were irradiated by ^{60}Co γ-ray (MSD Nordion, pencil type/C-198 sealed) at a dose-rate of 1.20 kGy/h and ^{60}Co γ-ray (MSD Nordion, pencil type/C-188 sealed) at dose-rate of 22.86 kGy/h for low dose-rate (20 Gy/min) and high dose-rate (381 Gy/min), respectively, at room temperature in air. The RIA and the shift of the Bragg peak wavelength were measured during the γ-ray irradiation of the fibers for 1 h with annealing of the fibers for 40 min after the γ-ray irradiation where the total length of the fiber including the FBG was 200 mm. The measurement set-up for the dose-rate effect of radiation on the FBG written in the fibers is shown in Fig. 5.3, where the length of the FBG and the recoated region were about 10 and 20 mm, respectively.

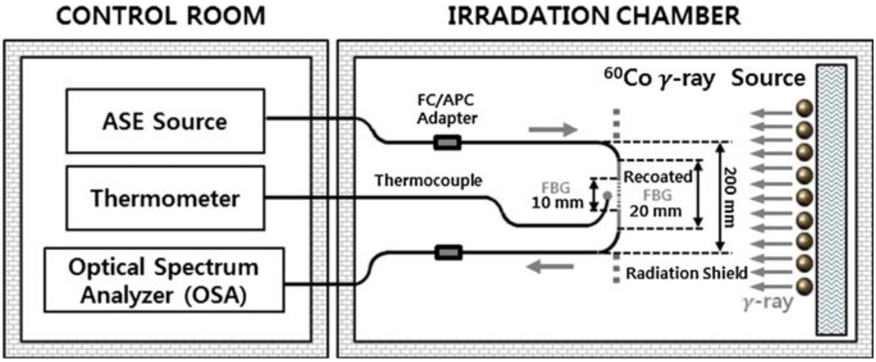

Fig. 5.3 Schematic diagram of the experimental setup for γ-ray irradiation on the optical fibers with the FBG

5.3 Results and Discussion

The transmission spectra of the FBG written in the fiber 1 and the fiber 2 during and after γ-ray irradiation to 1.20 and 22.86 kGy/h are shown in Figs. 5.4 and 5.5, respectively. Detailed specifications of the fiber 1 and the fiber 2 with the FBG during and after γ-ray irradiation are listed in Table 5.1. As shown in Fig. 5.4a, the temperature change, the Bragg reflection wavelength, the reflected peak power, and the transmission power at 1550 nm of the fiber 1 with FBG were 0.6 °C, −10 pm, −0.070, and −0.056 dB with the increase of γ-ray irradiation to 1.20 kGy/h, respectively. In the case of the fiber 2 with the FBG, the temperature change, the Bragg reflection wavelength, the reflected peak power, and the transmission power at 1550 nm were 0.1 °C, 5 pm, −0.057, and −0.072 dB with increase of γ-ray irradiation to 1.20 kGy/h as shown in Fig. 5.4b, respectively. From the results of Fig. 5.4, the RIA of the fibers 1 and 2 at 1550 nm were 0.280 and 0.360 dB/m, respectively. As γ-ray irradiation on the fiber 1 with the FBG increased, the temperature was found to increase and the Bragg reflection wavelength and the reflected peak power were shifted toward shorter wavelengths and decreased, respectively. However, in the case of the fiber 2 with the FBG, the Bragg reflection wavelength was shifted toward longer wavelengths with the increase of γ-ray irradiation. The FWHM bandwidth of fibers 1 and 2 remained unchanged during and after γ-ray irradiation to 1.20 kGy/h. The change in temperature, the Bragg reflection wavelength, and the RIA at 1550 nm during and after γ-ray irradiation to 1.20 kGy/h are shown in Figs. 5.6 and 5.7. While the temperature, the Bragg peak shift, and the RIA at 1550 nm have clearly shown the dose-rate dependence, no influence on the FWHM bandwidth and on the reflected power was observed, within the accuracy of our measurements.

It is interesting that as shown in Figs. 5.6 and 5.7, after the γ-ray irradiation, the temperature, the Bragg reflection wavelength, and the RIA at 1550 nm became recovered. The reflected peak power was found to decrease regardless of γ-ray

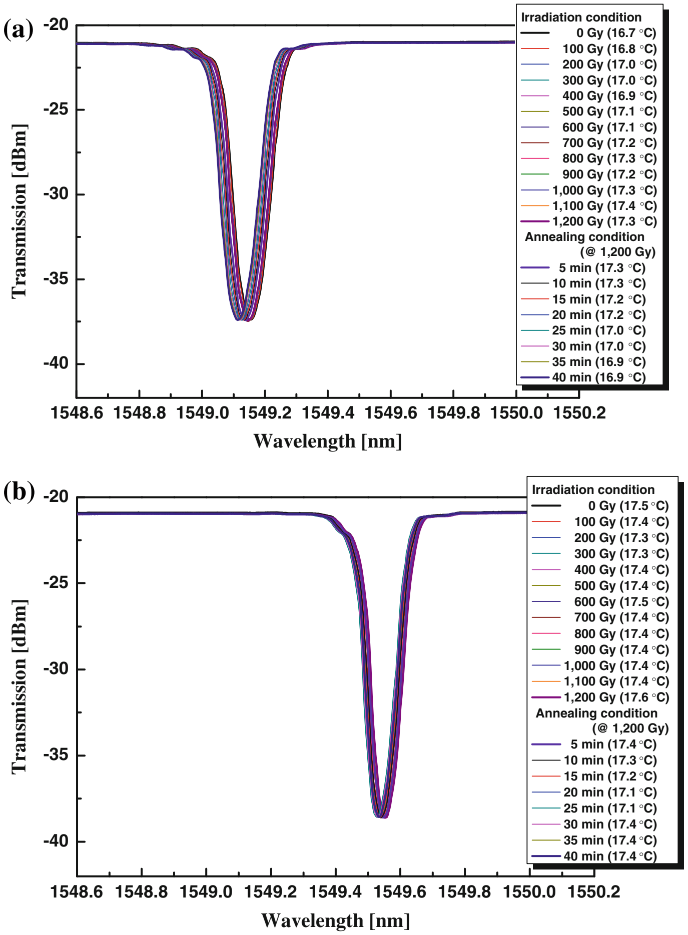

Fig. 5.4 Transmission spectra of the FBG written in **a** the fiber 1 and **b** the fiber 2 at dose-rates ranging from 0 to 1.20 kGy/h

irradiation and annealing process. Note that the radiation resistance characteristics was unaffected by the pure silica buffer layer and boron-doped inner cladding region of optical fiber and by γ-ray irradiation to 1.20 kGy/h, because of the low dose-rate or small total dose of the pre-irradiation (7.20 kGy γ-ray).

When the dose rate of γ-ray irradiation increased to 22.86 kGy/h, the radiation resistance characteristics during irradiation was strongly dependent on the large dose-rate and total dose, as shown in Fig. 5.5. The change in the temperature, the Bragg reflection wavelength, the reflected peak power, and the transmission power at 1550 nm of the fiber 1 with the FBG were 5.5 °C, 78 pm, 0.269, and −0.269 dB with the increase of γ-ray irradiation to 22.86 kGy/h, respectively. In the case of the fiber 2 with the FBG, the same four parameters of the fiber 2 with FBG were 5.7 °C,

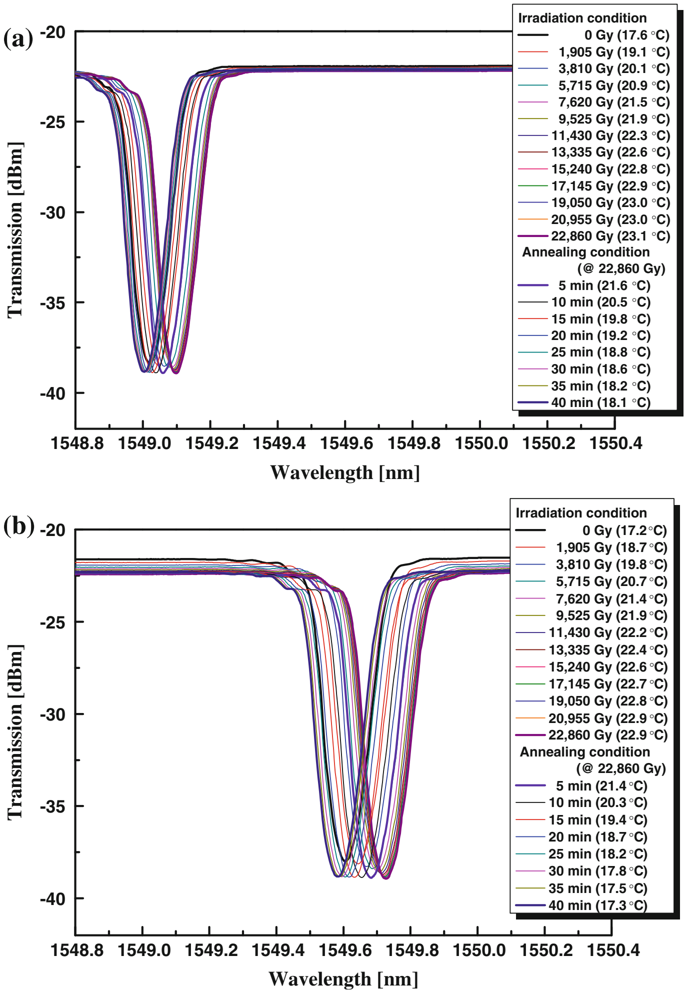

Fig. 5.5 Transmission spectra of FBG written in **a** the fiber 1 and **b** the fiber 2 at dose-rates ranging from 0 to 22.86 kGy/h

122 pm, 0.118, and −0.842 dB with the increase of γ-ray irradiation to 22.86 kGy/h as shown in Fig. 5.5b, respectively. The RIA of the fibers 1 and 2 at 1550 nm were 1.345 and 4.210 dB/m, respectively, from Fig. 5.5. As γ-ray irradiation on the fibers 1 and 2 with the FBG increased, the temperature and the reflected peak power increased and the transmission power at 1550 nm decreased. While the Bragg reflection wavelengths were shifted toward longer wavelengths during γ-ray irradiation, the FWHM bandwidth remained unchanged. With the increase of γ-ray irradiation to 22.86 kGy/h, the temperature, the Bragg reflection wavelength, and the RIA at 1550 nm became saturated. As shown in Figs. 5.8 and 5.9, after γ-ray

Table 5.1 Specifications of the fiber 1 and the fiber 2 with the FBG during and after γ-ray irradiation

			Temperature (°C)	Bragg reflection wavelength (nm)	FWHM bandwidth (nm)	Reflected peak power (dB)	Transmission @ 1550 nm (dBm)	RIA @ 1550 nm (dB/m)
Low dose-rate (20 Gy/min)	Fiber 1	Before irradiation (0 Gy)	16.7	1549.155	0.130	16.463	−20.968	0.280
		After irradiation (1.2 kGy)	17.3	1549.145	0.130	16.393	−21.024	
		After annealing (40 min)	16.9	1549.113	0.131	16.331	−21.010	–
	Fiber 2	Before irradiation (0 Gy)	17.5	1549.548	0.104	17.744	−20.846	0.360
		After irradiation (1.2 kGy)	17.6	1549.553	0.104	17.687	−20.918	
		After annealing (40 min)	17.4	1549.535	0.104	17.666	−20.895	–

(continued)

Table 5.1 (continued)

			Temperature (°C)	Bragg reflection wavelength (nm)	FWHM bandwidth (nm)	Reflected peak power (dB)	Transmission @ 1550 nm (dBm)	RIA @ 1550 nm (dB/m)
High dose-rate (381 Gy/min)	Fiber 1	Before irradiation (0 Gy)	17.6	1549.020	0.126	16.474	−21.911	1.345
		After irradiation (22.86 kGy)	23.1	1549.098	0.126	16.743	−22.180	
		After annealing (40 min)	18.1	1549.004	0.129	16.729	−22.110	–
	Fiber 2	Before irradiation (0 Gy)	17.2	1549.604	0.150	16.438	−21.539	4.210
		After irradiation (22.86 kGy)	22.9	1549.726	0.150	16.556	−22.381	
		After annealing (40 min)	17.3	1549.584	0.151	16.579	−22.242	–

Fig. 5.6 Variations of the Bragg reflection wavelength and the temperature during γ-ray irradiation of 1.20 kGy/h for **a** the fiber 1 and **b** the fiber 2 with the FBG

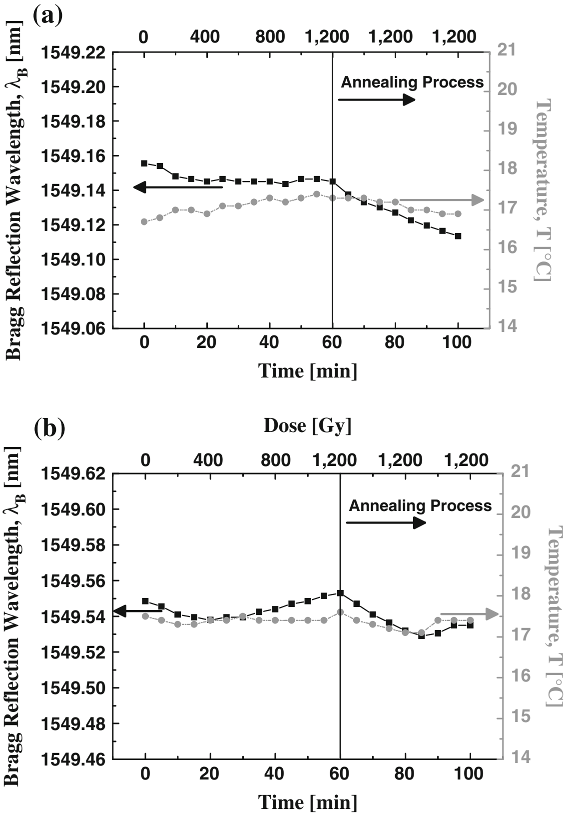

irradiation to 22.86 kGy/h, the temperature, the Bragg reflection wavelength, and the RIA at 1550 nm were recovered similar to those by γ-ray irradiation to 1.20 kGy/h. From the above results, it can be distinguished that the observed radiation-induced hardening strongly depends on the pure silica glass layer (buffer layer) of the germano-silicate glass optical fiber because of the employed pure silica buffer layer, which could block the increase of the NBOHC and the formation of E′ center in SiO_2 glass under γ-ray irradiation and minimize the residual stress developed in the fiber core due to different thermal properties of glasses having different compositions [8, 12, 14]. Therefore the germano-silicate glass optical fiber with pure silica buffer cladding layer can significantly decrease the RIA value about 3 times, as compared with that of the commercial single-mode fiber at dose-rate of 22.86 kGy/h.

Generally, the sensitivity of optical fiber sensor based on FBG depends on the Bragg wavelength shift per temperature, usually about 10 pm per 1 °C [2, 16]. Also, when the optical fiber sensor with the FBG is exposed to radiation, the Bragg reflection wavelength and the transmission power are shifted, decreasing due to the change of the reflective index of glass, the radiation-induced defects and color

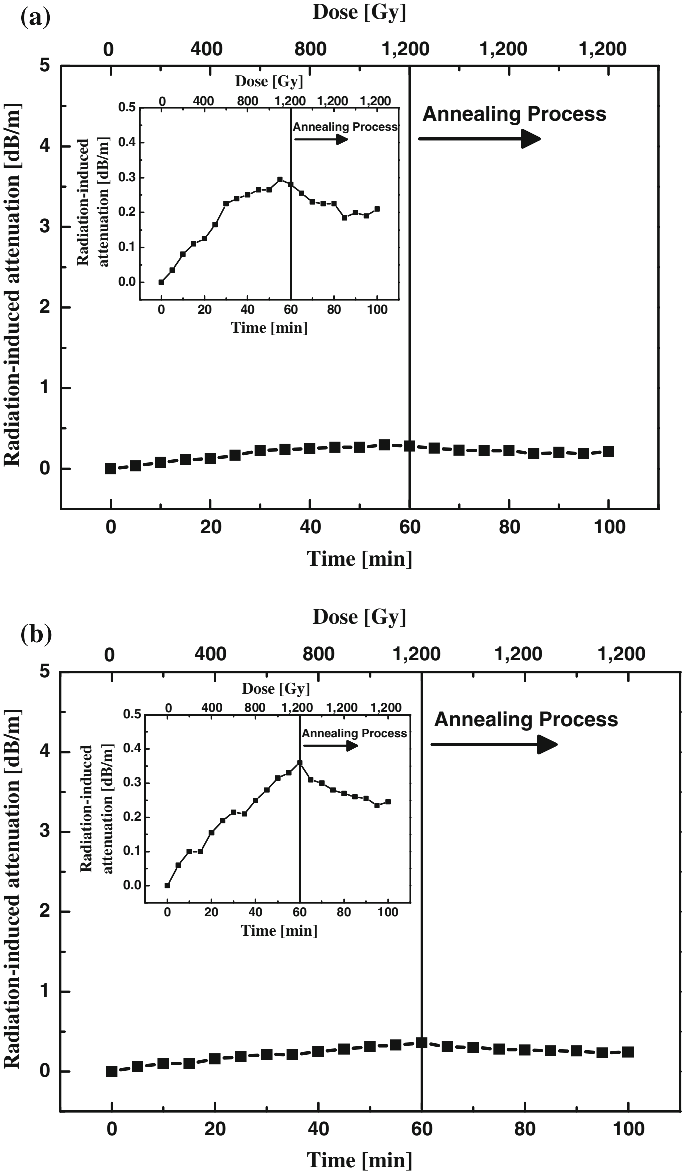

Fig. 5.7 Variations of the RIA during γ-ray irradiation of 1.20 kGy/h for **a** the fiber 1 and **b** the fiber 2 with the FBG

centers formation [4, 5, 7, 8]. Thus, the measurement sensitivities from temperature and radiation are limited by possible cross-sensitivity problems. The measured temperature sensitivities of the fiber 1 and fiber 2 at a dose-rate of 1.20 kGy/h were

Fig. 5.8 Variations of the Bragg reflection wavelength and the temperature during γ-ray irradiation of 22.86 kGy/h for **a** the fiber 1 and **b** the fiber 2 with the FBG

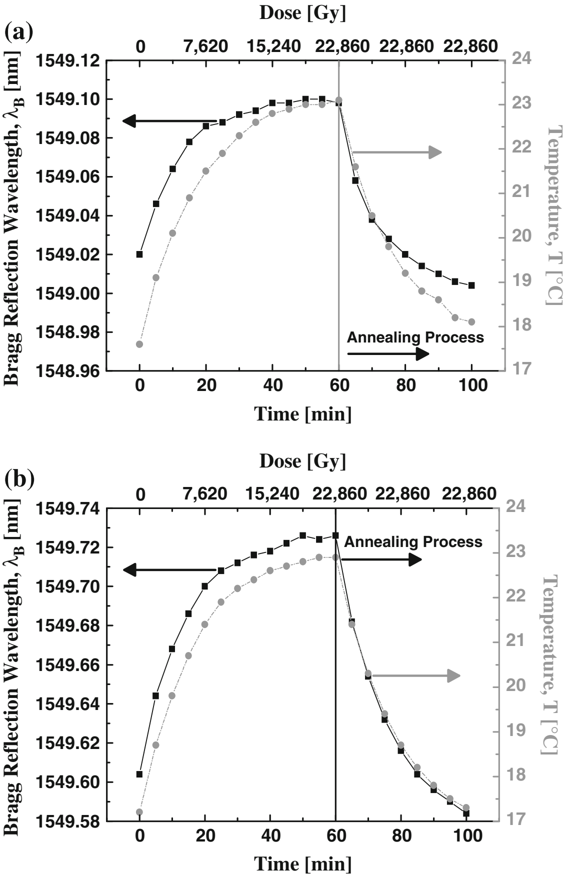

about −16 and 50 pm/°C, respectively, and at a dose rate of 22.86 kGy/h were about 14 and 21 pm/°C, respectively. Although the dose-rate effect of radiation on the FBG written in the optical fiber was limited at low dose-rate of 1.20 kGy, the temperature sensitivity of fiber 1 was lower than that of fiber 2 at a dose-rate of 22.86 kGy/h because the presence of boron oxide in the depressed-index inner cladding of the optical fiber may lead to a decrease of the refractive index as well as to a decrease in thermo-optic coefficient [14, 18]. Also, in the case of fiber 1, the temperature sensitivity was found to be unaffected at any dose-rate of γ-ray irradiation as compared with that of fiber 2. Therefore, the germano-silicate glass optical fiber with pure silica buffer cladding layer and boron-doped depressed-index inner cladding layer is useful for real-time temperature monitoring system in harsh nuclear environments.

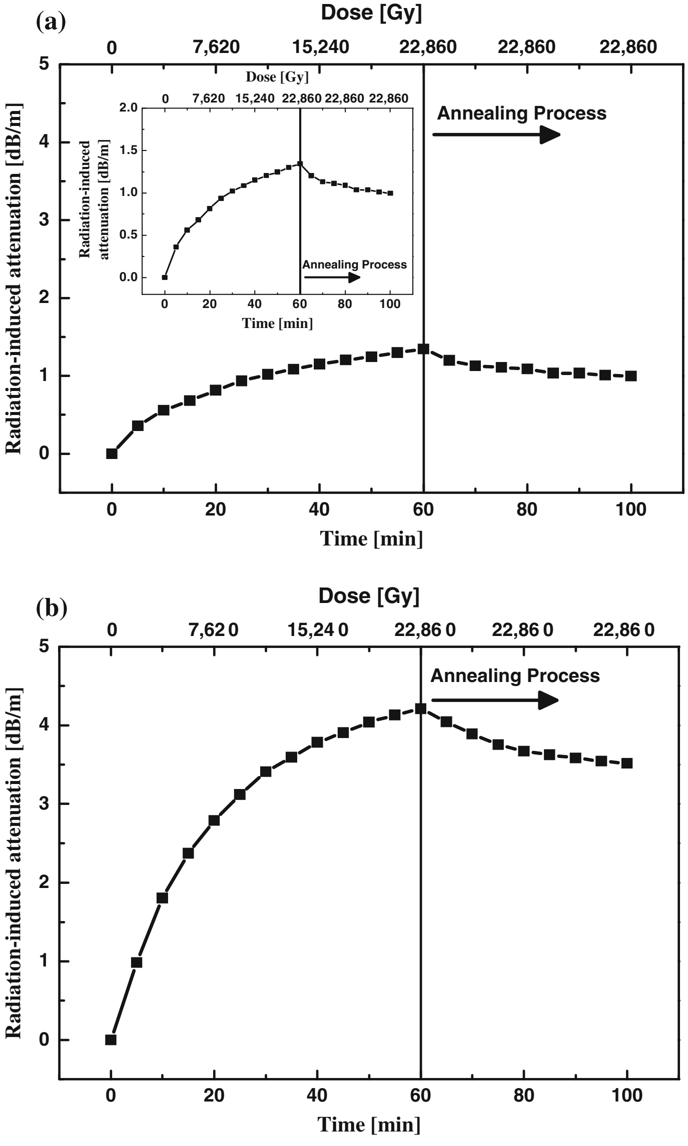

Fig. 5.9 Variations of the radiation-induced attenuation during γ-ray irradiation of 22.86 kGy/h for **a** the fiber 1 and **b** the fiber 2 with the FBG

5.4 Conclusions

The germano-silicate glass optical fiber incorporated with two inner cladding layers of pure silica buffer and boron-doped silica was fabricated by using the MCVD and the drawing process to enhance photosensitivity for FBG maintaining the radiation resistance for sensing applications in harsh nuclear environments. The pure silica buffer layer between the core and the cladding of the fiber was effective to increase the radiation resistance by blocking the increase of the NBOHC and the formation of E' center and by decreasing the residual stress in the fiber core. As the γ-ray irradiation on the FBG inscribed in the fabricated fiber increased, the Bragg reflection wavelength was shifted toward longer wavelength and saturated at a 78 pm level. The temperature sensitivity and the RIA were about 14 pm/°C and 1.345 dB/m at 1550 nm with the accumulated dose rate of 22.86 kGy/h, respectively. However, the FWHM bandwidth of the FBG remained practically unchanged.

Acknowledgements This work was partially supported by the New Growth Engine Industry Project of the Ministry of Trade, Industry and Energy, Basic Science Research Program through the National Research Foundation of Korea (NRF) funded by the Ministry of Education (No. 2013R1A1A2063250), the Korea government (MSIP) (No. 2011-0031840), the Brain Korea-21 Plus Information Technology Project through a grant provided by the Gwangju Institute of Science and Technology, South Korea.

References

1. J. Shah, Effects of environmental nuclear radiation on optical fibers. Bell Syst. Tech. J. **54**(7), 1207–1213 (1975)
2. A.I. Gusarov, F. Berghmans, O. Deparis, A.F. Fernandez, Y. Defosse, P. Mégret, M. Decréton, M. Blondel, High total dose radiation effects on temperature sensing fiber Bragg gratings. IEEE Photon Technol. Lett. **11**(9), 1159–1161 (1999)
3. A.I. Gusarov, F. Berghmans, A.F. Fernandez, O. Deparis, Y. Defosse, D. Starodubov, M. Decréton, P. Mégret, M. Blondel, Behavior of fiber Bragg grating under high total dose gamma radiation. IEEE Trans. Nucl. Sci. **47**(3), 688–692 (2000)
4. A.F. Fernandez, B. Brichard, F. Berghmans, M. Decréton, Dose-rate dependencies in gamma-irradiated fiber bragg grating filters. IEEE Trans. Nucl. Sci. **49**(6), 2874–2878 (2002)
5. A. Gusarov, D. Kinet, C. Caucheteur, M. Wuilpart, P. Mégret, Gamma radiation induced short-wavelength shift of the Bragg peak in type I fiber gratings. IEEE Trans. Nucl. Sci. **57**(6), 3775–3778 (2010)
6. A. Gusarov, S. Vasiliev, O. Medvedkov, I. Mckenzie, F. Berghmans, Stabilization of fiber Bragg gratings against gamma radiation. IEEE Trans. Nucl. Sci. **55**(4), 2205–2212 (2008)
7. B.D. Evans, The role of hydrogen as a radiation protection agent at low temperature in a low-OH, pure silica optical fiber. IEEE Trans. Nucl. Sci. **35**(6), 1215–1220 (1998)
8. A. Iino, J. Tamura, Radiation resistivity in silica optical fibers. J. Lightwave Technol. **6**(2), 145–149 (1988)
9. K. Sanada, N. Shamoto, K. Inada, Radiation resistance of fluorine-doped silica-core fibers. J. Non-Cryst. Solids **179**(4), 339–344 (1994)

10. H. Henschel, J. Kuhnhenn, U. Weinand, Radiation hard optical fibers. Paper presented at the optical fiber communication conference, Anaheim, California, OThI1-3 March 2005
11. K. Nagasawa, Y. Hoshi, Y. Ohki, K. Yahagi, Improvement of radiation resistance of pure silica core fibers by hydrogen treatment. Jpn. J. Appl. Phys. **24**(9), 1224–1228 (1985)
12. T. Kakuta, T. Shikama, M. Narui, T. Sagawa, Behavior of optical fibers under heavy irradiation. Fusion Eng. Des. **41**(1), 201–205 (1998)
13. E.M. Dianov, K.M. Golant, R.R. Khrapko, A.L. Tomashuk, Nitrogen doped silica core fibers: a new type of radiation-resistant fiber. Electron. Lett. **31**(17), 1490–1491 (1995)
14. S. Ju, Y. Kim, S. Jeong, J.-Y. Kim, N.-H. Lee, H.-K. Jung, W.-T. Han, Gamma-ray dose-rate dependence of fiber Bragg grating inscribed germano-silicate glass optical fiber with boron-doped inner cladding. Paper presented at the 2nd international conference on photonics, optics, and laser technology, Lisbon, Portugal, 107–113 January 2014
15. J. Stone, Reduction of OH absorption in optical fibers by OH → OD isotope exchange. Ind. Eng. Chem. Prod. Res. Dev. **25**(4), 609–621 (1986)
16. S. Ju, P.R. Watekar, W.-T. Han, Enhanced sensitivity of the FBG temperature sensor based on the PbO-GeO_2-SiO_2 glass optical fiber. J. Lightwave Technol. **28**(18), 2697–2700 (2010)
17. K.O. Hill, G. Meltz, Fiber Bragg grating technology fundamentals and overview. J. Lightwave Technol. **15**(8), 1263–1276 (1997)
18. P.M. Cavaleiro, F.M. Araújo, L.A. Ferreira, J.L. Santos, F. Farahi, Simultaneous measurement of strain and temperature using Bragg gratings written in germanosilicate and boron-codoped germanosilicate Fibers. IEEE Photon Technol. Lett. **11**(12), 1635–1637 (1999)

Chapter 6
Optical Modelling of Luminescent Cascade Systems with the Adding-Doubling Method

Sven Leyre, Martijn Withouck, Guy Durinck, Johan Hofkens, Geert Deconinck and Peter Hanselaer

Abstract The adding-doubling method can be used to determine the reflection and transmission characteristics of materials exhibiting bulk scattering and photoluminescence. In this work, the method is adapted to allow the implementation of luminescent cascade systems. Distinctive for these systems are the multiple re-absorption and re-emission events by the different luminescent materials. The proposed method is validated by comparing its results to the simulation results of traditional Monte Carlo ray tracing. The average difference over the visible wavelength range between the two methods is found to be smaller than 0.5 %. A large reduction in computation time was realized compared to the ray tracing simulations, which makes the adding-doubling method an excellent optimization tool.

S. Leyre · M. Withouck · G. Durinck · P. Hanselaer (✉)
Light & Lighting Laboratory, KU Leuven, Gebroeders Desmetstraat 1,
9000 Ghent, Belgium
e-mail: peter.hanselaer@kuleuven.be

S. Leyre
e-mail: sven.leyre@kuleuven.be

M. Withouck
e-mail: martijn.withouck@kuleuven.be

G. Durinck
e-mail: guy.durinck@kuleuven.be

J. Hofkens
Department of Chemistry, KU Leuven, Celestijnenlaan 200 F, bus 2404,
3001 Leuven, Belgium
e-mail: johan.hofkens@chem.kuleuven.be

G. Deconinck
ESAT/ELECTA, KU Leuven, Kasteelpark Arenberg 10, bus 2445,
3001 Leuven, Belgium
e-mail: geert.deconinck@esat.kuleuven.be

P.A. Ribeiro and M. Raposo (eds.), *Photoptics 2014*,
Springer Proceedings in Physics 177, DOI 10.1007/978-3-319-27321-1_6

6.1 Introduction

The adding-doubling (AD) method is a commonly used evaluation method to quickly determine the reflection and transmission characteristics of a stack of homogeneous plane parallel layers [5, 14, 21]. The layers may contain both surface and bulk scattering. Recently, the method was extended for photoluminescent layers [10]. However, the method described in [10] does not allow re-absorption and subsequent re-emission. This hampers the simulation of luminescent cascade systems and the modelling of materials with a significant overlap between excitation and emission spectra.

In many applications, multiple photoluminescent materials are combined. In white light-emitting diodes (LEDs), blue LEDs are usually combined with a yellow phosphor to obtain white light [9, 13, 16, 22]. To obtain better colour rendering characteristics, a red emitting luminescent material is usually added. The most commonly used yellow phosphor for LED applications is the Yttrium Aluminium Garnet doped with Cerium (YAG:Ce). As a red-emitting luminescent material, EU^{2+} doped phosphors or red-emitting quantum dots can be used [16, 22]. These phosphors will typically exhibit significant absorption in the yellow wavelength range and thus constitute a luminescent cascade system.

An alternative way to obtain white LEDs is the combination of near uv emitting diodes and a red, green, and blue emitting phosphor [3, 4, 22]. This approach is similar to the tri-colour phosphor blends used in fluorescent tubes, compact fluorescent lamps, and cold cathode fluorescent tubes used in backlight units for displays.

The use of luminescent cascade systems is also popular in luminescent solar concentrators (LSCs). In these devices, light incident on a sheet containing one or more luminescent materials, is (partially) absorbed and re-emitted in all directions at longer wavelengths. Part of the re-emitted light is trapped in the sheet due to total internal reflection at top and bottom of the sheet. Light travels laterally towards the sides, where a solar cell is located. To obtain a high efficiency, multiple luminescent dyes are used to obtain a broad absorption spectrum [1, 20].

In this paper, an improved version of the adding-doubling method for photoluminescent layers is presented, which allows the implementation of luminescent cascade systems and adequate modelling of materials with a significant overlap between excitation and emission spectra. First, the light propagation in photoluminescent materials is discussed, next the theoretical background for the improved adding-doubling method is presented, and finally the method is validated by comparing the results with traditional Monte Carlo ray tracing simulations.

6.2 Radiative Transfer Equation

Light propagating through a system can interact with objects and surfaces present in the system. At a smooth interface, reflection and refraction according to Snell's and Fresnel's laws occurs. When the interface is rough, scattering will take place, which is usually described by a Bidirectional Scattering Distribution Function (BSDF).

Within a medium, the time invariant light propagation is described by the radiative transfer equation (RTE), given in (6.1) [10].

$$\begin{aligned} &\boldsymbol{s} \cdot \nabla L(\boldsymbol{r}, \boldsymbol{s}, \lambda) \\ &\quad = -(\mu_a(\lambda) + \mu_s(\lambda)) \cdot L(\boldsymbol{r}, \boldsymbol{s}, \lambda) + \mu_s(\lambda) \cdot \int p(\boldsymbol{s}, \boldsymbol{s}', \lambda) \cdot L(\boldsymbol{r}, \boldsymbol{s}', \lambda) \cdot d\Omega' \end{aligned} \tag{6.1}$$

In words, this equation represents the change in spectral radiance $L(\boldsymbol{r}, \boldsymbol{s}, \lambda)$ at position $\boldsymbol{r}$ in direction $\boldsymbol{s}$. The first term on the right hand side represents the spectral radiance lost due to absorption and scattering, the second term is the radiance contribution in direction $\boldsymbol{s}$ due to scattering from all other directions $\boldsymbol{s}'$ integrated over solid angle $d\Omega'$.

In (6.1), $\mu_a(\lambda)$ and $\mu_s(\lambda)$ are the absorption and scattering coefficient and define the average distance traveled by a photon before being absorbed and scattered, respectively. The phase function $p(\boldsymbol{s}, \boldsymbol{s}')$ gives the probability a photon will be scattered in a certain direction. If the scattering occurs isotropically, $p(\boldsymbol{s}, \boldsymbol{s}')$ is a constant. A commonly used phase function is the Henyey-Greenstein phase function, which has one free parameter: the anisotropy factor g, which is identical to the average of the cosine of the scatter angle [6].

The RTE given in (6.1) must be extended for photoluminescent materials to take into account the contribution due to emission at the emission wavelengths. The RTE for emission wavelengths in a material with a single photoluminescent material is given by (6.2) [10].

$$\begin{aligned} \boldsymbol{s} \cdot \nabla L(\boldsymbol{r}, \boldsymbol{s}, \lambda) = &-(\mu_a(\lambda) + \mu_s(\lambda)) \cdot L(\boldsymbol{r}, \boldsymbol{s}, \lambda) + \mu_s(\lambda) \cdot \int p(\boldsymbol{s}, \boldsymbol{s}', \lambda) \cdot L(\boldsymbol{r}, \boldsymbol{s}', \lambda) \cdot d\Omega' \\ &+ \int \mu_e(\lambda_i) \cdot QE(\lambda_i) \cdot w_M(\lambda, \lambda_i) \cdot \int \frac{1}{4 \cdot \pi} \cdot L(\boldsymbol{r}, \boldsymbol{s}', \lambda_i) \cdot d\Omega' \cdot d\lambda_i \end{aligned} \tag{6.2}$$

The third term on the right hand side is the contribution at the emission wavelength λ due to luminescence caused by excitation at all excitation wavelengths λ_i. Since the emission due to excitation at wavelength λ_i causes emission at all emission wavelengths, a weight factor $w_M(\lambda, \lambda_i)$ is used to denote the fraction of the light emitted at a particular emission wavelength λ due to excitation at

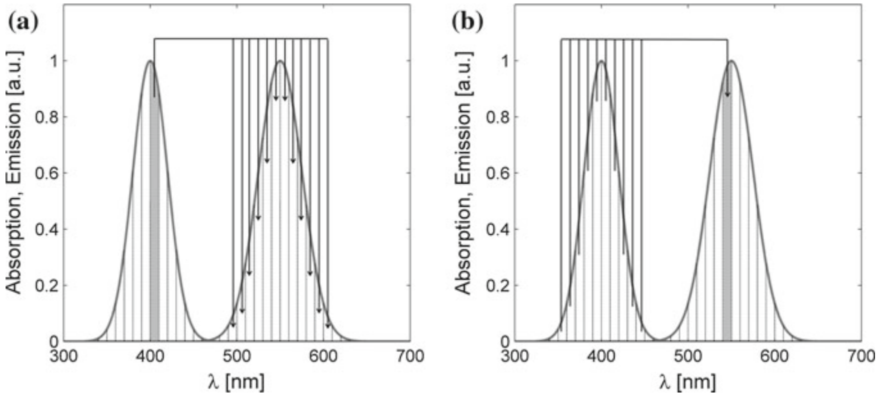

Fig. 6.1 Schematic representation of **a** the distribution of the emitted light due to photoluminescent from one excitation wavelength over the emission wavelength range and **b** the contribution of all excitation wavelengths to the emission at one emission wavelength

wavelength λ_i. This weight factor can be immediately derived from the emission spectrum, as shown in Fig. 6.1a. The integral of all weight factors at emission wavelength λ over the excitation wavelength λ_i must be normalized to one. QE is the quantum efficiency of the luminescent material, $\mu_e(\lambda_i)$ is the excitation coefficient, and can be calculated using (6.3).

$$\mu_e(\lambda_i) = \mu_a(\lambda_i) \cdot \frac{\int w_M(\lambda, \lambda_i) \cdot \lambda \cdot d\lambda}{\lambda_i} \tag{6.3}$$

The excitation coefficient can be derived from the absorption coefficient $\mu_a(\lambda_i)$ at excitation wavelength λ_i, and the Stokes shift losses. The integral over all excitation wavelengths λ_i in (6.2), denotes that there is a contribution from all excitation wavelengths at the particular emission wavelength λ, schematically shown in Fig. 6.1b. If the selected wavelength λ is not included in the spectral emission band of the material, the third term on the right hand side of (6.2) disappears ($w_M(\lambda, \lambda_i)$ is zero) and the RTE for non-fluorescent materials is obtained [10].

Several solutions exist to solve the RTE (for photoluminescence), e.g. Monte Carlo simulations [19], two flux approximations [23], discrete ordinates angular discretization schemes (SN methods) [8], and the AD method [10]. The latter approach has the advantage that it combines fast computation with high accuracy.

The RTE for luminescent cascade systems containing M types of photoluminescent particles is given by (6.4).

$$\begin{aligned}
\boldsymbol{s}\cdot\nabla L(\boldsymbol{r},\boldsymbol{s},\lambda) = &-\left(\mu_a^1(\lambda)+\mu_s^1(\lambda)\right)\cdot L(\boldsymbol{r},\boldsymbol{s},\lambda)+\mu_s^1(\lambda)\cdot\int p^1(\boldsymbol{s},\boldsymbol{s}',\lambda)\cdot L(\boldsymbol{r},\boldsymbol{s}',\lambda)\cdot d\Omega' \\
&+\int \mu_e^1(\lambda_i)\cdot QE^1(\lambda_i)\cdot w_M^1(\lambda,\lambda_i)\cdot\int\frac{1}{4\cdot\pi}\cdot L(\boldsymbol{r},\boldsymbol{s}',\lambda)\cdot d\Omega'\cdot d\lambda_i \\
&-\left(\mu_a^2(\lambda)+\mu_s^2(\lambda)\right)\cdot L(\boldsymbol{r},\boldsymbol{s},\lambda)+\mu_s^2(\lambda)\cdot\int p^2(\boldsymbol{s},\boldsymbol{s}',\lambda)\cdot L(\boldsymbol{r},\boldsymbol{s}',\lambda)\cdot d\Omega' \\
&+\int \mu_e^2(\lambda_i)\cdot QE^2(\lambda_i)\cdot w_M^2(\lambda,\lambda_i)\cdot\int\frac{1}{4\cdot\pi}\cdot L(\boldsymbol{r},\boldsymbol{s}',\lambda)\cdot d\Omega'\cdot d\lambda_i \\
&+\ldots \\
&-\left(\mu_a^M(\lambda)+\mu_s^M(\lambda)\right)\cdot L(\boldsymbol{r},\boldsymbol{s},\lambda)+\mu_s^M(\lambda)\cdot\int p^M(\boldsymbol{s},\boldsymbol{s}',\lambda)\cdot L(\boldsymbol{r},\boldsymbol{s}',\lambda)\cdot d\Omega' \\
&+\int \mu_e^M(\lambda_i)\cdot QE^M(\lambda_i)\cdot w_M^M(\lambda,\lambda_i)\cdot\int\frac{1}{4\cdot\pi}\cdot L(\boldsymbol{r},s',\lambda)\cdot d\Omega'\cdot d\lambda_i
\end{aligned} \tag{6.4}$$

In (6.4), the superscripts denote the optical properties of the various types of photoluminescent particles. The RTE for multiple photoluminescent pigments can be written in the form of (6.2) for a single luminescent material, by calculating the optical properties for the combined luminescent particles from the optical properties of the individual luminescent pigments, using (6.5)–(6.10).

$$\mu_a(\lambda)=\mu_a^1(\lambda)+\mu_a^2(\lambda)+\cdots+\mu_a^M(\lambda) \tag{6.5}$$

$$\mu_s(\lambda)=\mu_s^1(\lambda)+\mu_s^2(\lambda)+\cdots+\mu_s^M(\lambda) \tag{6.6}$$

$$p(\boldsymbol{s},\boldsymbol{s}',\lambda)=\frac{p^1(\boldsymbol{s},\boldsymbol{s}',\lambda)\cdot\mu_s^1(\lambda)+p^2(\boldsymbol{s},\boldsymbol{s}',\lambda)\cdot\mu_s^2(\lambda)+\cdots+p^M(\boldsymbol{s},\boldsymbol{s}',\lambda)\cdot\mu_s^M(\lambda)}{\mu_s^1(\lambda)+\mu_s^2(\lambda)+\cdots+\mu_s^M(\lambda)} \tag{6.7}$$

$$\mu_e(\lambda_i)=\mu_e^1(\lambda_i)+\mu_e^2(\lambda_i)+\cdots+\mu_e^M(\lambda_i) \tag{6.8}$$

$$QE(\lambda_i)=\frac{QE^1(\lambda_i)\cdot\mu_e^1(\lambda_i)+QE^2(\lambda_i)\cdot\mu_e^2(\lambda_i)+\cdots+QE^M(\lambda_i)\cdot\mu_e^M(\lambda_i)}{\mu_e^1(\lambda_i)+\mu_e^2(\lambda_i)+\cdots+\mu_e^M(\lambda_i)} \tag{6.9}$$

$$w_M(\lambda,\lambda_i)=\frac{\begin{array}{r}w_M^1(\lambda,\lambda_i)\cdot\mu_e^1(\lambda_i)\cdot QE^1(\lambda_i)+w_M^2(\lambda,\lambda_i)\cdot\mu_e^2(\lambda_i)\cdot QE^2(\lambda_i)\\ +\cdots+w_M^M(\lambda,\lambda_i)\cdot\mu_e^M(\lambda_i)\cdot QE^M(\lambda_i)\end{array}}{\mu_e^1(\lambda_i)\cdot QE^1(\lambda_i)+\mu_e^2(\lambda_i)\cdot QE^2(\lambda_i)+\cdots+\mu_e^M(\lambda_i)\cdot QE^M(\lambda_i)} \tag{6.10}$$

Reducing the RTE for luminescent cascade systems to the form of a single photoluminescent material has the advantage that is allows for straight forward implementation in the existing methods to solve the photoluminescent RTE.

6.3 The Adding-Doubling Method

The adding-doubling (AD) method was first developed by Stokes [18] in 1862 and allows the calculation of reflection and transmission of a stack of layers. The method has been adapted to allow the calculation of reflection and transmission of a homogeneous plane parallel slab containing bulk scattering [21] and has found its way to the astronomy [5] and bio-medical field [15]. Recently, the method was adapted to allow the calculation of reflection and transmission of a photoluminescent layer [10]. The main advantage of the AD method over e.g. Monte Carlo ray tracing simulations is that the AD method is much quicker. This allowed the use of the AD method in an iterative procedure to estimate bulk scattering properties of tissues and diffusers [11, 12, 14]. The Monte Carlo approach has the advantage that it is not limited to plane parallel geometries.

In the AD method, the incident radiance on a material is angularly divided into cones or channels, which can be mathematically represented as a vector, where each element in the vector represents the radiance within a channel. The reflection and transmission characteristics are represented in matrices, allowing the radiance to be angularly distributed over the different channels.

Equation (6.11) gives the mathematical representation of the transmission of the spectral radiance through a slab [21].

$$\begin{bmatrix} L_1(\theta_1) \\ \vdots \\ L_1(\theta_n) \end{bmatrix} = \begin{bmatrix} T_{01}(\theta_1,\theta_1) & \cdots & T_{01}(\theta_1,\theta_n) \\ \vdots & \ddots & \vdots \\ T_{01}(\theta_n,\theta_1) & \cdots & T_{01}(\theta_n,\theta_n) \end{bmatrix} \times \begin{bmatrix} L_0(\theta_1) \\ \vdots \\ L_0(\theta_n) \end{bmatrix} \tag{6.11}$$

With L_0 being the incident spectral radiance and L_1 the transmitted spectral radiance. The radiance is divided into n channels (represented by the corresponding polar angle θ). The matrix elements $T_{xy}(\theta_a, \theta_b)$ represent the light propagation from spectral radiance in channel a, at interface x of the plane parallel layer, to spectral radiance in channel b, at interface y. Equation (6.11) can also be written as $\boldsymbol{L}_1 = \boldsymbol{T}_{01} \times \boldsymbol{L}_0$, with $\boldsymbol{L}_0$ and $\boldsymbol{L}_1$ being the spectral radiance vectors and $\boldsymbol{T}_{01}$ the transmission matrix.

When dealing with luminescent layers, the radiance is not only redistributed angularly, but also spectrally. The spectral radiance at wavelengths included in the spectral emission band, has contributions from all spectral radiances included in the spectral excitation band. Leyre et al. [10] used conversion matrices to handle the spectral redistribution of the spectral radiance (mathematically represented in (6.12).

$$\boldsymbol{L}_1(\lambda) = \boldsymbol{T}_{01}(\lambda) \times \boldsymbol{L}_0(\lambda) + \sum_{i=1}^{N} \boldsymbol{T}_{01}(\lambda_i) \times \boldsymbol{L}_0(\lambda_i) \tag{6.12}$$

In (6.12), $\boldsymbol{L}_0(\lambda)$ and $\boldsymbol{L}_1(\lambda)$ are the incident and transmitted spectral radiance at emission wavelength λ, respectively, $\boldsymbol{L}_0(\lambda_i)$ is the incident spectral radiance at excitation wavelength λ_i and $\boldsymbol{T}_{01}(\lambda_i, \lambda)$ is the conversion matrix, representing the contribution due to photoluminescence at wavelength λ from wavelength λ_i in the forward direction. Each wavelength within the excitation wavelength region will contribute to the emission at wavelength λ, this is represented by the summation in (6.12), where the excitation wavelength region is divided into N wavelength intervals with central wavelength λ_i.

To calculate the reflection and transmission through a layer which contains bulk scattering or photoluminescence, the AD method starts from a thin single scatter layer. The thickness of the layer is chosen in such a way that a photon will only interact a single time with the material. The reflection and transmission characteristics of this single scatter layer are determined from the RTE, given in (6.2). Next, the layer is doubled in size, by adding two identical layers together and calculating the reflection and transmission. This step is repeated until the desired thickness is reached. A more elaborate explanation of the AD method can be found in [10].

The AD method for luminescent layers starts from (6.13) and (6.14), representing the relationship between the upward and downward spectral radiance at each interface of a single plane parallel layer.

$$\begin{aligned} \boldsymbol{L}_1^+(\lambda) &= \boldsymbol{R}_{10}(\lambda) \times \boldsymbol{L}_1^-(\lambda) + \boldsymbol{T}_{01}(\lambda) \times \boldsymbol{L}_0^+(\lambda) \\ &\quad + \sum_{i=1}^{N} \boldsymbol{R}_{10}^c(\lambda, \lambda_i) \times \boldsymbol{L}_1^-(\lambda_i) + \boldsymbol{T}_{01}^c(\lambda, \lambda_i) \times \boldsymbol{L}_0^+(\lambda_i) \end{aligned} \tag{6.13}$$

$$\begin{aligned} \boldsymbol{L}_0^-(\lambda) &= \boldsymbol{R}_{01}(\lambda) \times \boldsymbol{L}_0^+(\lambda) + \boldsymbol{T}_{10}(\lambda) \times \boldsymbol{L}_1^-(\lambda) \\ &\quad + \sum_{i=1}^{N} \boldsymbol{R}_{01}^c(\lambda, \lambda_i) \times \boldsymbol{L}_0^+(\lambda_i) + \boldsymbol{T}_{10}^c(\lambda, \lambda_i) \times \boldsymbol{L}_1^-(\lambda_i) \end{aligned} \tag{6.14}$$

Herein, the superscripts '+' and '−' represent the spectral radiance going down- and upwards respectively. The subscript '0' and '1' for the radiances represent the spectral radiance incident on or leaving the top and bottom interface of the layer respectively. For the reflection and transmission matrices, the first number of the subscripts denotes the in interface on which the radiance is incident (e.g. $\boldsymbol{R}_{01}$ represents the reflection matrices for light incident on the top of the layer). If the wavelength does not fall within the emission wavelength region, the third and fourth term on the right hand side of (6.13) and (6.14) will disappear, since the conversion matrices are null matrices.

The AD method combines (6.13) and (6.14) to obtain the reflection and transmission characteristics of the doubled layer. It inherently assumes that all radiances at wavelengths λ_i are not included in the emission wavelength region, i.e. the conversion matrices in (6.13) and (6.14) are null matrices for all λ_i [10]. The result of this approach is that luminescent cascade systems, where re-absorption (and subsequent re-emission) of converted photons occurs, cannot be adequately treated.

To solve this problem, the spectral radiance can be written in vector form for the full spectrum instead of one vector for each wavelength. As a result, the reflection and transmission matrices will allow the conversion of wavelength (both up- and down-conversion) without the need for special conversion matrices. Equation (6.15) now replaces the equations for each individual wavelength given by (6.11).

$$\begin{bmatrix} L_1(\theta_1,\lambda_1) \\ \vdots \\ L_1(\theta_n,\lambda_1) \\ \vdots \\ L_1(\theta_1,\lambda_n) \\ \vdots \\ L_1(\theta_n,\lambda_n) \end{bmatrix} = \begin{bmatrix} T_{01}(\theta_1,\theta_1,\lambda_1,\lambda_1) & \cdots & T_{01}(\theta_1,\theta_n,\lambda_1,\lambda_1) & \cdots & T_{01}(\theta_1,\theta_n,\lambda_1,\lambda_N) \\ \vdots & & \vdots & & \vdots \\ T_{01}(\theta_n,\theta_1,\lambda_1,\lambda_1) & \cdots & T_{01}(\theta_n,\theta_n,\lambda_1,\lambda_1) & \cdots & T_{01}(\theta_1,\theta_n,\lambda_1,\lambda_N) \\ \vdots & & \vdots & & \vdots \\ T_{01}(\theta_1,\theta_1,\lambda_N,\lambda_1) & \cdots & T_{01}(\theta_1,\theta_n,\lambda_N,\lambda_1) & \cdots & T_{01}(\theta_1,\theta_n,\lambda_N,\lambda_N) \\ \vdots & & \vdots & & \vdots \\ T_{01}(\theta_n,\theta_1,\lambda_N,\lambda_1) & \cdots & T_{01}(\theta_n,\theta_n,\lambda_N,\lambda_1) & \cdots & T_{01}(\theta_1,\theta_n,\lambda_N,\lambda_N) \end{bmatrix}$$

$$\begin{matrix} \cdots & T_{01}(\theta_1,\theta_n,\lambda_1,\lambda_N) \\ & \vdots \\ \cdots & T_{01}(\theta_n,\theta_n,\lambda_1,\lambda_N) \\ & \vdots \\ \cdots & T_{01}(\theta_n,\theta_n,\lambda_N,\lambda_N) \\ & \vdots \\ \cdots & T_{01}(\theta_n,\theta_n,\lambda_N,\lambda_N) \end{matrix}\Bigg] \times \begin{bmatrix} L_0(\theta_1,\lambda_1) \\ \vdots \\ L_0(\theta_n,\lambda_1) \\ \vdots \\ L_0(\theta_1,\lambda_n) \\ \vdots \\ L_0(\theta_n,\lambda_n) \end{bmatrix} \tag{6.15}$$

Equation (6.15) allows both angular and spectral redistribution of light with a single matrix. Using the new vector-matrix notation, the third and fourth term on the right hand side of (6.13) and (6.14) become obsolete (since conversion matrices are no longer required). In Fig. 6.2, a schematic representation of the vector-matrix equation given in (6.13) for a system with one excitation and one emission wavelength is presented, according to the old notation in (6.11) (Fig. 6.2a), and according to the new notation, given by (6.15) (Fig. 6.2b).

It is now much easier to obtain the reflection and transmission characteristics of a double layer, by combining (6.13) and (6.14). The condition that the excitation wavelengths cannot be emission wavelengths as well, no longer exists. This allows to obtain the reflection and transmission characteristics of luminescent cascade systems and materials which exhibit a significant spectral overlap between excitation and emission wavelength regions. Equations (6.13) and (6.14) (without the third and fourth term on the right hand side) can be written for two separate second layers. Combining the equations for the two layers leads to the reflection and transmission matrices for the combined layer, given by (6.16) and (6.17) [10, 21].

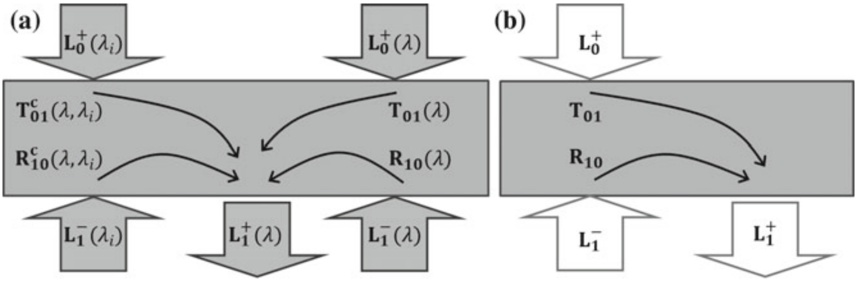

Fig. 6.2 Schematic representation of the vector-matrix equation (6.13) according to **a** the vector-notation given by (6.11), with a vector for the spectral radiance at each wavelength and **b** the vector-matrix notation given by (6.15), with the radiance for all wavelengths gathered in one vector

$$\boldsymbol{R}_{20} = \boldsymbol{R}_{21} + \boldsymbol{T}_{12} \times (\boldsymbol{E} - \boldsymbol{R}_{10} \times \boldsymbol{R}_{12})^{-1} \times \boldsymbol{R}_{10} \times \boldsymbol{T}_{21} \tag{6.16}$$

$$\boldsymbol{T}_{02} = \boldsymbol{T}_{12} \times (\boldsymbol{E} - \boldsymbol{R}_{10} \times \boldsymbol{R}_{12})^{-1} \times \boldsymbol{T}_{01} \tag{6.17}$$

Herein, $\boldsymbol{E}$ is the unity matrix. To obtain the transmittance and reflectance of a layer, the elements of the incident radiance vector ($\boldsymbol{L}_0$) in (6.15) must be given the value 1 for the desired angles and wavelengths. The transmitted radiance vector ($\boldsymbol{L}_1$) can be calculated using (6.15). The transmittance at each wavelength can be calculated by integration over the different angles of the radiance represented in the transmitted radiance vector. In a similar way the reflectance can be obtained.

6.4 Adding-Doubling Versus Monte Carlo Simulations

To validate the method described in the previous section, the results of the AD method are compared with traditional Monte Carlo ray tracing simulations. A remote phosphor converter (RPC) containing a yellow phosphor and red quantum dots is modelled to compare the results obtained with both methods. The RPC has optical flat surfaces (only Fresnel reflections at the air-converter interfaces), a refractive index of 1.5, thickness of 1 mm, and contains YAG:Ce phosphor particles and CIS/ZnS quantum dots. The concentration of the luminescent particles in the RPC was optimized to obtain a colour temperature of 4000 K in transmission.

The optical properties of the YAG:Ce phosphor particles are taken from [13]. At a concentration of 0.085 g/cm^3, the average scattering coefficient μ_s over the visible wavelength range is 10.86 mm^{-1}, and the average anisotropy factor g is 0.863. For the modelling the Henyey-Greenstein phase function is selected, since this allows for easy implementation in the AD method [7]. The absorption and emission spectra of the phosphor are shown in Fig. 6.3. The peak absorption at 470 nm at concentration 0.085 g/cm^3 is 0.76 mm^{-1}. The QE of the phosphor is 0.87.

Fig. 6.3 Absorption (*dashed line*) and emission spectrum (*full line*) of the YAG:Ce phosphor (*green*) and the CIS/ZnS quantum dots (*red*), together with the spectral radiant flux of the blue LED (*full blue line*)

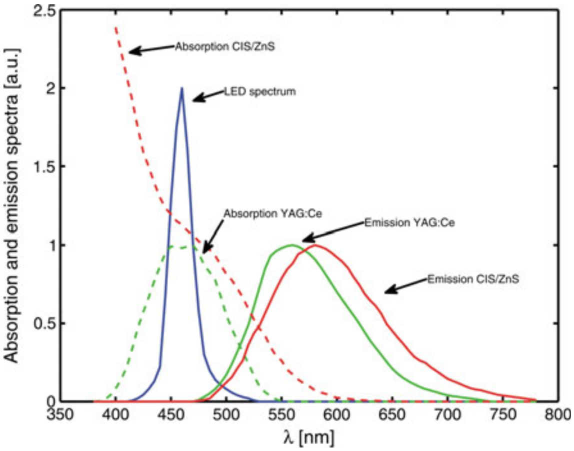

The optical properties of the CIS/ZnS quantum dots are taken from [17]. Quantum dots exhibit negligible scattering compared to the absorption and therefore scattering by the quantum dots is not taken into account in the simulations. The absorption and emission spectra of the quantum dots are shown in Fig. 6.3. The QE of the quantum dots is 0.79. In Fig. 6.3, an obvious overlap between absorption spectrum of the quantum dots and the emission spectrum of the YAG:Ce phosphor can be noticed, which makes the combination of these luminescent materials an excellent choice for the validation of the improved AD method.

The phosphor converter is illuminated with a blue LED, with peak wavelength 460 nm. The spectral radiant flux of the LED is represented in Fig. 6.3.

The Monte Carlo simulations are performed with the software package TracePro. In this software, Fresnel reflections are handled by attributing a probability to each ray to be reflected or transmitted at an interface according to the Fresnel reflection and transmission coefficients. The volume scattering is handled by use of the scattering coefficient and the anisotropy factor, which can be introduced in the program for each wavelength. The photoluminescence is handled by tracing the source from short to long wavelengths. The rays absorbed in the fluorescent material are stored to the hard disk. When an emission wavelength is reached, the absorbed rays are converted to the emission wavelength and given the appropriate radiant flux. This approach differs from the standard ray tracing procedure for photoluminescence in the ray tracer software and allows for the simulation of luminescent cascade systems.

Both luminescent materials exhibit a spectral overlap between excitation and emission spectra. When the illumination wavelength falls within this overlap range, the emission spectra will red-shift, since it is not physically possible to have photoluminescent emission of photons with a higher energy than the absorbed photons [2]. In this study, the emission spectrum at excitation wavelengths that fall within the emission wavelength range, is cut-off at the excitation wavelength.

6.4.1 Accuracy Comparison

Using an infinite number of rays in the Monte Carlo simulations, would result in the perfect solution of the light propagation problem. Using a smaller amount of rays will introduce some noise in the simulations. To estimate the accuracy of the AD method, the Monte Carlo ray trace was performed with 500,000 rays per wavelength. This resulted in an average relative standard deviation over all wavelengths of less than 0.5 % between traces performed with different random seeds.

The accuracy of the AD method depends on the number of angular channels used, using more channels leads to a better description of the light propagation and thus a more accurate calculation of the transmittance and reflectance.

The simulations and calculations are performed between 380 and 780 nm and in steps of 5 nm. In Fig. 6.4, the result of the Monte Carlo simulation (using 500,000 rays per wavelength) and the AD calculations (using 32 angular channels) is shown, together with the relative deviation between the two methods.

From Fig. 6.4, it can be seen that there is only a very small deviation between the AD calculations and the Monte Carlo simulations. The average relative deviation is smaller than 0.5 %. Moreover, given the random variation of the deviation over the wavelengths, it can be attributed to noise in the Monte Carlo simulations. It can be concluded that the AD method can indeed be used to calculate reflection and transmission of a luminescent cascade system with a high accuracy.

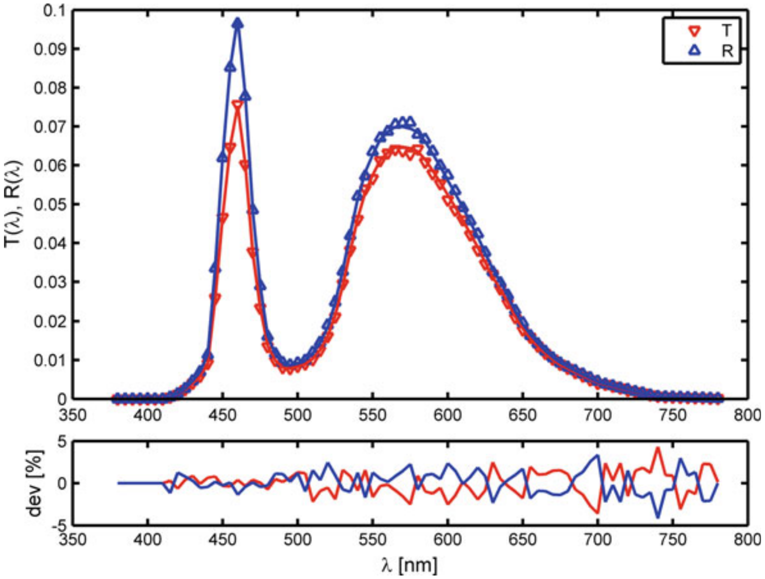

Fig. 6.4 Comparison between the AD method (*lines*) and Monte Carlo simulations (*marks*) for the transmitted spectrum T (*triangles*) and the reflected spectrum R (*squares*), together with the relative deviation (dev) between the two methods

6.4.2 Computation Time Comparison

The computation time strongly depends on the number of rays per wavelength used in the ray tracing simulations and the number of channels considered in the AD method. Decreasing the number of rays for the Monte Carlo simulations or channels in the AD calculations, will lead to a shorter computation time but also to a lower accuracy. The amount of noise in the ray tracing simulations can be quantified by performing different simulations with a different seed or initial random set of rays and aclulating the standard deviation between the different simulation results. The accuracy of the AD calculations is determined by comparing its results with a ‘perfect’ solution, i.e. by comparing it to the results of a ray tracing simulations with 500,000 rays per wavelength.

In Fig. 6.5, the computation time and corresponding noise in the Monte Carlo simulations is presented in function of the number of incident rays per wavelength, together with the accuracy and computation time of the AD method in function of the number of angular channels.

Setting the threshold accuracy to 1 %, the ray tracing simulation requires 10,000 rays per wavelength, corresponding to approximately 37 min of computation time. The computation time of the AD method depends on the number of angular channels which are considered. If 8 channels are used, the computation time is approximately 12 s. If 16 channels are used, the deviation on the result drops to approximately 0.5 % and the computation time amounts to 88 s. This corresponds to a reduction of computation time compared to the Monte Carlo simulations with a factor 185 and 25 for 8 and 16 channels, respectively.

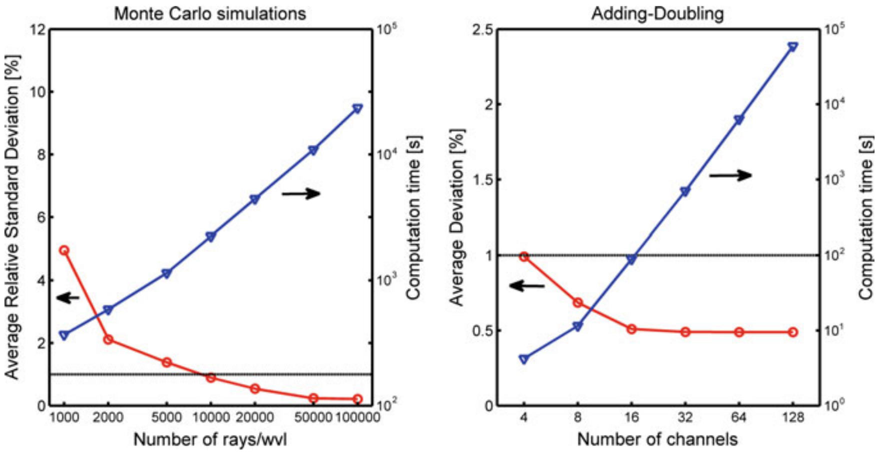

Fig. 6.5 Accuracy (*red*) and computation time (*blue*), in function of the number of incident wavelengths for the Monte Carlo simulations (*left*) and in function of the number of angular channels for the AD calculations (*right*). The *black lines* denote the accuracy threshold of 1 %

6.5 Conclusions

The adding-doubling (AD) method for photoluminescent materials was adapted to allow the calculation of reflection and transmission characteristics of a plane parallel luminescent cascade system. The proposed method was validated by comparing its results to the results of traditional Monte Carlo ray tracing simulations. The deviation between the two methods was smaller than 0.5 %. The computation time with the AD method was approximately 12 s, while the Monte Carlo simulations took 37 min, resulting in a decrease of computation time with a factor 185. The accurate yet fast results make the AD method an excellent tool for the optimization of luminescent cascade systems.

Acknowledgements The authors would like to thank the SIM (Flemish Strategic Initiative for Materials) and IWT (Flemish agency for Innovation by Science and Technology) for their financial support through the SoPPoM project within the SIBO program.

References

1. S.T. Bailey, G.E. Lokey, M.S. Hanes, J.D.M. Shearer, J.B. McLafferty, G.T. Beaumont, T.T. Baseler, J.M. Layhue, D.R. Broussard, Y. Zhang, B.P. Wittmershaus, Optimized excitation energy transfer in a three-dye luminescent solar concentrator. Sol. Energ. Mat. Sol. C. **91**, 67–75 (2007)
2. S. Dhami, A.J. de Mello, G. Rumbles, S.M. Bishop, D. Phillips, A. Beeby, Phthalocyanine fluorescence at high concentration: dimers or reabsorption effect? Photochem. Photobiol. **61** (4), 341–346 (1995)
3. N.C. George, K.A. Denault, R. Seshadri, Phosphors for solid-state white lighting. Annu. Rev. Mater. Res. **43**, 481–501 (2013)
4. J.K. Han, J.I. Choi, A. Piquette, M. Hannah, M. Anc, M. Galvez, J.B. Talbot, J. McKittrick, Phosphor development and integration for near-UV LED solid state lighting. ECS J. Solid State Sci. Technol. **2**(2), R3138–R3147 (2013)
5. J.E. Hansen, Radiative transfer by doubling very thin layers. Astrophys. J. **155**, 563–573 (1969)
6. L.G. Henyey, J.L. Greenstein, Diffuse radiation in the galaxy. Astrophys. J. **93**, 70–83 (1941)
7. J.H. Joseph, W.J. Wiscombe, The delta-eddington approximation for radiative flux transfer. J. Atmos. Sci. **33**, 2452–2459 (1976)
8. A. Joshi, J.C. Rasmussen, E.M. Sevick-Muraca, T.A. Wareing, J. McGhee, Radiative transport based frequency domain fluorescence tomography. Phys. Med. Biol. **53**(8), 2069–2088 (2008)
9. K.H. Lee, S.W.R. Lee, in *Process development for yellow phosphor coating on blue light-emitting diodes (LEDs) for white light illumination*. 8th Conference Electronics Packaging Technology, Singapore (2006)
10. S. Leyre, G. Durinck, B. Van Giel, W. Saeys, J. Hofkens, G. Deconinck, P. Hanselaer, Extended adding-doubling method for fluorescent applications. Opt. Express **20**(16), 17856–17872 (2012)
11. S. Leyre, F.B. Leloup, J. Audenaert, G. Durinck, J. Hofkens, G. Deconinck, P. Hanselaer, Determination of the bulk scattering parameters of diffusing materials. Appl. Optics **52**(18), 4083–4090 (2013)

12. S. Leyre, Y. Meuret, G. Durinck, J. Hofkens, G. Deconinck, P. Hanselaer, Estimation of the effective phase function of bulk diffusing materials with the inverse adding-doubling method. Appl. Optics **53**(10), 2117–2125 (2014)
13. Z. Liu, S. Liu, K. Wang, X. Luo, Measurement and numerical studies of optical properties of YAG: Ce phosphor for white light-emitting diode packaging. Appl. Opt. **49**(2), 247–257 (2010)
14. S.A. Prahl, M.J.C. van Gemert, A.J. Welch, Determining the optical properties of turbid media by using the adding-doubling method. Appl. Opt. **32**(4), 559–568 (1993)
15. W. Saeys, M.A. Velazco-Roa, S.N. Thennadil, H. Ramon, B.M. Nicola, Optical properties of apple skin and flesh in the wavelength range from 350 to 2200 nm. Appl. Opt. **47**(7), 908–919 (2008)
16. P.F. Smet, A.B. Parmentier, D. Poelman, Selecting conversion phosphors for white light-emitting diodes. J. Electrochem. Soc. **158**(6), R37–R54 (2011)
17. W.-S. Song, S.-H. Lee, H. Yang, Fabrication of warm, high CRI white LED using non-cadmium quantum dots. Opt. Mater. Express **3**(9), 1468–1473 (2013)
18. G.G. Stokes, On the intensity of the light reflected from or transmitted through a pile of plates. Proc. Roy. Soc. London **11**, 545–556 (2008)
19. D. Sahin, B. Ilan, Radiative transport theory for light propagation in luminescent media. J. Opt. Soc. Am. A: **30**(5), 813–820 (2013)
20. W.G.J.H.M. van Sark, Luminescent solar concentrators—a low cost photovoltaics alternative. Renew. Energ. **49**, 207–210 (2013)
21. W.J. Wiscombe, On initialization, error and flux conservation in the doubling method. J. Quant. Spectrosc. Radiat. Transfer **16**, 637–658 (1976)
22. S. Ye, F. Xiao, Y.X. Pan, Y.Y. Ma, Q.Y. Zhang, Phosphors in phosphor-converted white light-emitting diodes: recent advances in materials, techniques and properties. Mat. Sci. Eng. R **71**(1), 1–34 (2010)
23. D. Yudovsky, L. Pilon, Modeling the local excitation fluence rate and fluorescence emission in absorbing and strongly scattering multilayered media. Appl. Opt. **49**(31), 6072–6084 (2010)

Chapter 7
An Optical System for Comparing the Speeds of Starlights

Jingshown Wu, Yen-Ru Huang, Shenq-Tsong Chang, Hen-Wai Tsao, San-Liang Lee and Wei-Cheng Lin

Abstract The constancy of the speed of light is the second hypothesis of Einstein's special relativity theory proposed in 1905. Since then science and technology have advanced very much, which can be used to reexamine the century old hypothesis. We proposed a novel method and implemented an optical system accordingly to compare the speed of starlight with the well-known speed of light from a terrestrial source, *c*. The system consists of a transmitter and a receiver. The transmitter modulated starlight, terrestrial red and infrared lights into pulses simultaneously. After travelling a distance, these pulses were detected by the receiver. A high speed oscilloscope is used to record the arrival times of these pulses, where the terrestrial infrared pulse and the red pulse are used as the trigger and the reference signals. During the measurement, we employed a terrestrial white light travelling along the exact path of the starlight to calibrate the system. We also carefully reduce the errors during the measurement and the data processing, and get some results in these years. We find that comparing with the terrestrial white light pulse, the starlight pulses arrived at the receiver with various degrees of delays. The values of the time delays are likely related to the relative radial velocities of the stars. The result implies that the measured apparent speed of starlight is not constant.

J. Wu (✉) · Y.-R. Huang · H.-W. Tsao
Department of Electrical Engineering, Graduate Institute of Photonics and Optoelectronics, National Taiwan University, Taipei 10617, Taiwan
e-mail: wujsh@ntu.edu.tw; wujsh@cc.ee.ntu.edu.tw

J. Wu · Y.-R. Huang · H.-W. Tsao
Graduate Institute of Communication Engineering, National Taiwan University, Taipei 10617, Taiwan

S.-T. Chang · W.-C. Lin
Instrument Technology Research Center, National Applied Research Laboratories, Hsin-Chu 30076, Taiwan

S.-L. Lee
Department of Electronic Engineering, National Taiwan University of Science and Technology, Taipei 10617, Taiwan

P.A. Ribeiro and M. Raposo (eds.), *Photoptics 2014*,
Springer Proceedings in Physics 177, DOI 10.1007/978-3-319-27321-1_7

7.1 Introduction

The speed of light is an important physical parameter which is used to estimate other physical parameters such as mass, time, space, energy, etc. In 1676, Römer investigated the eclipses of Io, Jupiter's nearest moon, and estimated that the speed of light was about 214,000 km/s [1, 2]. In 1728, Bradley observed aberration of Draconi. He gave a value for the speed of light of 301,000 km/s [1]. Both measurements used light from extraterrestrial sources. In 1849, Fizeau used a chopper and a distant mirror to measure the speed of light on the terrestrial. He estimated the speed of light equal to 3.153 × 108 m/s [1, 2]. In 1862, Foucault employed a rotating mirror instead of a chopper. He obtained a value of the speed of light about 298,000 ± 500 km/s [1, 2]. In 1878, Michelson constructed the famous Michelson interferometer to measure the effect of ether on the speed of light. He obtained a null result [3]. During 1880 and 1882, Michelson made many series of measurements and obtained the value 299,853 ± 60 km/s [1]. In the latter half of the nineteenth century, many measurements using the velocity of electromagnetic radiation or the ratio of electromagnetic to electrostatic units were conducted. The results are very similar to the previous ones [1, 2]. Currently, the recommended measured value of the speed of light on the earth, c, is equal to 299,792.5 km/s [2].

In 1905, Einstein published his special theory of relativity based on the following two postulates [3]: (1) The laws of physics are the same in all inertial frames. (2) The speed of light in vacuum is constant regardless of any reference frame.

In 1908, Ritz assumed that the speed of light might be influenced by the motion of the source [4],

$$c' = c + u, \tag{7.1}$$

where c is the speed of light from a resting source, i.e. the well-known value, u is the relative velocity between the source and the detector, c' is the apparent speed of light from the moving source. In this paper, we use the star as the light source and place the detector on the earth, so the light source and the detector have relative motion.

Table 7.1 shows the radial velocities, magnitudes, spectrum bands, right ascensions, declinations, and distances of Capella, Betelgeuse, Arcturus, Aldebaran, and Vega from the sun [5–7]. The data in Table 7.1 come from different references. They may have small variation.

Figure 7.1 is a sketch of a celestial sphere and positions of the stars. The orbital speed of the earth, V_e, is about 30 km/s which is on the ecliptic plane. Let V_s denote the radial velocity of the star from the sun and $\overline{AB}$ be the projection of the radial line of the star on the ecliptic plane. θ is the angle between V_e and $\overline{AB}$, φ is the angle between V_s and $\overline{AB}$. So the projected orbital velocity of the earth on V_s is $V_e \cos\theta \cos\varphi$. The relative radial velocity of the star and the earth V_r is $V_s - V_e \cos\theta \cos\varphi$.

Table 7.1 The data of Capella, Betelgeuse, Arcturus, Aldebaran, and Vega

Star	Capella	Betelgeuse	Arcturus	Vega	Aldebaran
Apparent magnitude	0.91/0.76 (B-V)	0.58 (V)	−0.04 (V)	0.03 (V)	0.85 (V)
Stellar classification	G8 III/GI III	M2 Iab	K2 III	A0 V	K5 III
Right ascension	5 h 16 min 41 s	5 h 55 min 10 s	14 h 15 min 39 s	18 h 36 min 56 s	4 h 35 min 55 s
Declination	+45°59′52″	+7°24′25″	+19°10′56″	+38°47′01″	+16°30′33″
Radial velocity V_s (km/s)	29.65	21.91	−5.19	−13.9	54.26
Distance (light year/parse)	42.5 ± 0.5/13.04 ± 0.03	643 ± 146/197 ± 45	36.7 ± 0.3/11.24 ± 0.09	25.3 ± 0.1/7.76 ± 0.03	65 ± 0.1/20.0 ± 0.4
Relative radial velocity (km/s) (March 18, 2010)	56.47	49.56	−20.77	−27.10	82.43

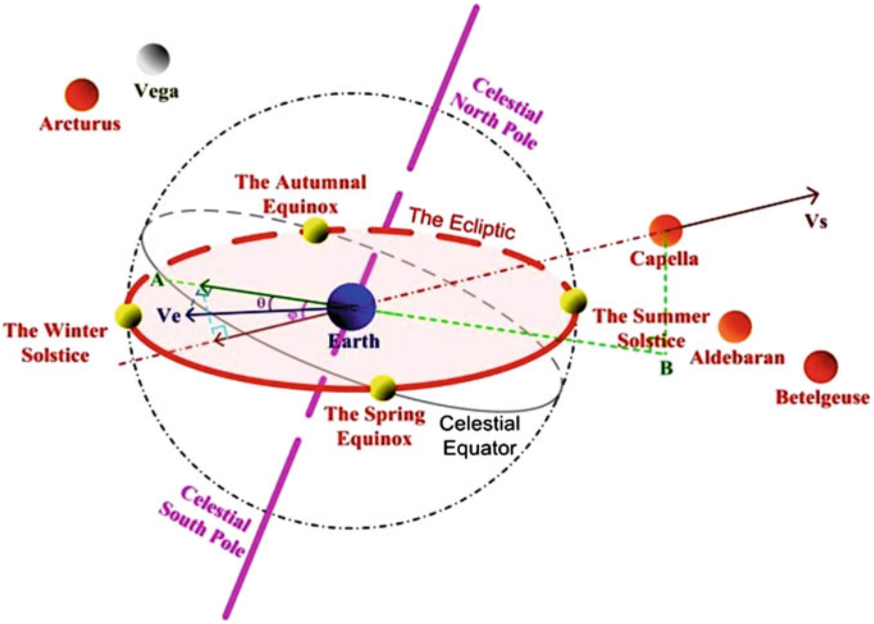

Fig. 7.1 The sketch of celestial sphere, positions of Capella, Betelgeuse, Arcturus, Aldebaran, and Vega (not on scale), the radial velocities of Capella and the earth, and θ and φ

7.2 System Design

Some of physical parameters are dimensionless, others are dimensional and their numerical values depend entirely on the units in which they are defined. The speed of light is dimensional and expressed in terms of length per unit time. To measure the speed of light, we need a rule and a watch. Especially to measure the speed of light emitting from a moving source, we encounter the simultaneity problem. Conventionally the detector and the moving source are considered in two different reference frames. In 1892, H.A. Lorentz proposed the Lorentz Transformation as follows [3]:

If the relative motion of the two reference frames is along their x and x' axes, the first frame with the space and time units x' and t' moves to the right with speed relative to the second frame with space and time units x and t, then

$$x' = \frac{(x - vt)}{\sqrt{1 - v^2/c^2}} \tag{7.2}$$

$$t' = \frac{(t - vx/c^2)}{\sqrt{1 - v^2/c^2}} \tag{7.3}$$

$$y' = y \tag{7.4}$$

$$z' = z \tag{7.5}$$

$$x = \frac{(x' + vt')}{\sqrt{1 - v^2/c^2}} \tag{7.6}$$

$$t = \frac{(t' + vx'/c^2)}{\sqrt{1 - v^2/c^2}} \tag{7.7}$$

$$y = y' \tag{7.8}$$

$$z = z' \tag{7.9}$$

where v is the relative speed of these two reference frames.

In our design, we can avoid using the units transformation and simultaneity problem. We compare the apparent speed of starlight with the well-known value, c. Therefore, we only use the space and time units on the earth, in other words, we have one rule and one clock. Also because the speed of light is about 3×10^8 m/s which is extremely fast, the speed of an ordinary moving light source on the earth is much less the speed of light. To investigate the influence of the speed of a moving light source on the light speed measurement is a difficult task. However the universe provides the experimental environment.

Our measurement system consists of a transmitter and a distant receiver. At the transmitter, we used a telescope to collect the light from Capella, Betelgeuse, Arcturus, Aldebaran, and Vega. These stars are bright and have large relative radial velocities with respect to the earth around the Spring Equinox. Then we modulated the starlight, terrestrial 635 nm red light, and 1550 nm infrared light into pulses simultaneously. After travelling a distance, d, these pulses arrived at the receiver. The red light travelled along almost the same path of the starlight. So we were able to use the red light and the 1550 nm infrared pulses as the reference and trigger signals. We used the terrestrial white light which travelled along exactly the same path of the starlight to calibrate the system.

If the speed of light is constant, the travelling time of starlight pulses and the terrestrial white light pulses from the transmitter to the receiver should be the same as

$$t_1 = d/c \tag{7.10}$$

If Ritz's assumption is valid and the speed of starlight has deviated from the well-known value, c, then the time taken for the starlight pulses travelling from the transmitter to the receiver is given by

$$t_2 = d/(c - V_r) \tag{7.11}$$

where V_r is the relative velocity of the star and the earth.

7.3 System Description

Based on the design principle and concept described in the previous section, we have two different designs: one using a rotating mirror and a slit to modulate the continuous light beam into pulses and the other employing an optical chopper.

7.3.1 *The Optical System Using a Rotating Mirror and a Slit*

Figure 7.2 shows the schematics of the system layout [8–12]. At the transmitter, for the starlight path, we used the one-meter telescope of the Lulin Observatory to collect the starlight. One end of a five-meter fiber with core diameter of 68 μm and the numerical aperture about 0.0729 was placed at the focal point of the telescope to guide the starlight. The other end of the fiber was fixed at the focal point of the off-axis parabolic mirror, P1, which made the ray collimating. It was then reflected by the rotating mirror, M1, and was incident upon the off-axis parabolic mirror, P2. A 100 μm wide slit was located at the focal point of P2 and another off-axis parabolic mirror, P3. When the rotating mirror M1 spun, the light would scan across

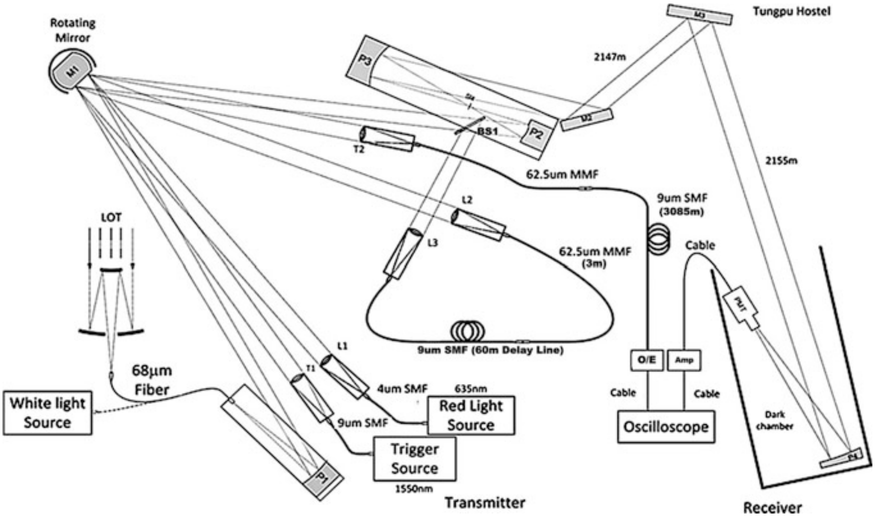

Fig. 7.2 The schematics of the optical system using rotating mirror

the slit to produce light pulses. The pulses were reflected by P3 to the planar mirrors, M2 and M3, where M3 was located at the Tungpu Hostel about 2147 m from the Lulin Observatory. The collimating ray from M3 travelled 2155 m back to the Lulin Observatory to reach the 30 cm off-axis parabolic mirror, P4. A photo-multiplier tube (PMT) was placed at the focal point of P4. Therefore, the total travel distance, d, was 4302 m.

For the path of the reference red light, a laser with a wavelength of 635 nm and a 4 μm single mode fiber pigtail was used as the reference light source. The end of the fiber was located at the focal point of the lens, L1. The collimating ray from L1 was incident to the rotating mirror, M1, and then the lens, L2, with a standard 62.5 μm multimode fiber connected a 9 μm single mode fiber located at the focal point. The 62.5 μm fiber acted as a slit and guided the pulses. The total length of this fiber link was 63 m, which separated the red light and starlight pulses by about 300 ns on the oscilloscope screen when M1 spun at 17,929 rpm. The other end of the single mode fiber of the link was placed at the focal point of the lens, L3. Then the collimating ray from L3 was combined with the starlight by a beam combiner BS1. Thereafter the red light and the starlight pulses travelling along the same path were received by the PMT to convert them into electrical pulses which could then be recorded by the oscilloscope. For the trigger signal, a 1550 nm laser with an Erbium doped fiber amplifier and a 9 μm single mode fiber pigtail was used as the trigger source. The end of the pigtail fiber was placed at the focal point of the lens, T1. The collimating ray from T1 was incident to M1 and then the lens, T2. At the focal point of T2, we had a standard 62.5 μm multimode fiber which acted as a slit and guided the pulses through the 3085-m single mode fiber to the receiver. A photodetector was employed to convert the infrared pulses to electrical pulses which were used as the trigger signal for the oscilloscope.

7.3.2 The Optical System Employing a Chopper

When we use the rotating two-facet mirror and a slit as a modulator, the reflected beam from the mirror M1 scans over the slit to product the pulses while the rotating mirror spun. The spindle which drives the rotating mirror may have wobble and the angular velocity deviation. Here we propose the optical system using a chopper as the modulator [12]. In this system the light beam is fixed. When the chopper spins the light beam is modulated into pulses. Figure 7.3 is the schematics of the optical system using a chopper. The starlight is collected by the telescope and guided by the 68 μm fiber whose output end is placed at the focal point of P1. The reflected collimating beam is incident to M1, M12 and P2. The focal point of P2 and P3 is at the slit of the chopper. The reflected collimating beam from P3 then is incident to the planner mirror M2 and transmits over 4.3 km to P4. The PMT is located at the focal point of P4. The 1550 infrared is collimated by the lens L1 and then combined by the beam splitter, BS1, with the starlight main path. After the chopper, part of the 1550 nm light is separated by the P90 beam splitter and through the lens L2 and

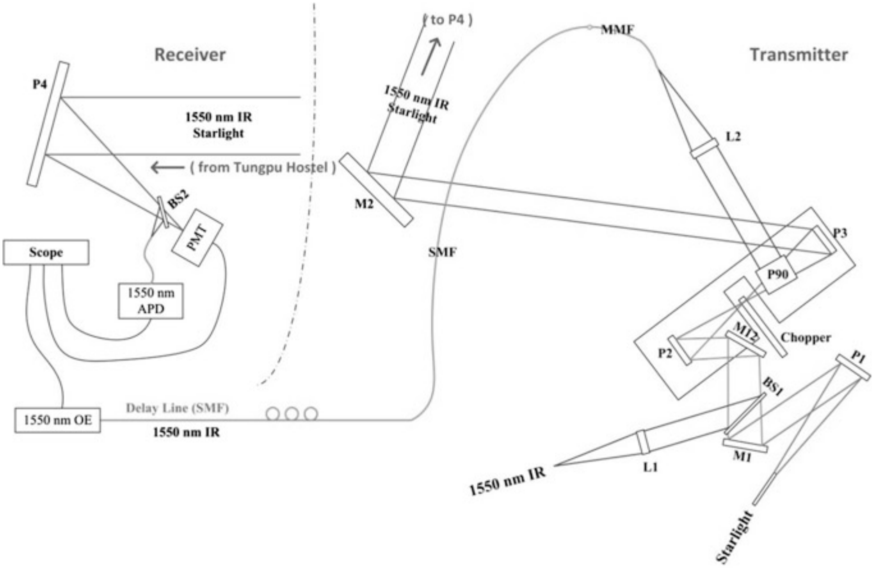

Fig. 7.3 The schematics of the optical system using chopper

incident to the multimode fiber connected to the 3.8 km single mode fiber delay line. At the end of the single mode delay line, the 1550 nm optical/electrical converter converts the optical signal to the electrical signal. The rest part of 1550 nm travels along with the starlight and reaches the receiver where the beam splitter BS2 and an Avalanche Photon-Diode are used to separate the 1550 nm light and converts to the electrical signal. When the chopper spins, the starlight and the 1550 nm infrared are modulated into pulses simultaneously. The two 1550 nm pulses at the receiver can be used as the trigger and the reference signals. In this system, the chopper is a very important element, which must be light weight and easy to have dynamically balanced. We have used titanium alloy and composite carbon fiber to fabricate the chopper. However the preparation is still on-going.

7.4 Measurement Results

We used the optical system using the rotating mirror and the slit to perform the measurement in November 2009, March 2010, March 2012, and March 2013. In order to minimize the error due to deviation of the spindle speed, we carefully aligned the parabolic mirrors and the lenses P1, P2, T1, T2, L1 and L2, such that the three beams from P1, T1, and L1, after reflected from the rotating mirror M1, were simultaneously incident to the slit after P2, the focal points of T2 and L2, respectively.

Because the optical power of the starlight was very low (in the order of a few nanowatts or less), the PMT operated in the photon counting mode which generated spikes instead of full waveforms. On the oscilloscope screen, the maximum amplitudes of dark current and thermal noises were 0.024 V and very small compared to the spikes and trigger pulses. To avoid accumulation of noises, we first choose a threshold at 0.025 V and set all recorded data smaller than the threshold to zero. If there are spikes in the frame, we classify it as a valid frame, otherwise we discard it. To reconstruct the starlight and the red light pulse waveforms, after taking a moving average of length 100 on the trigger pulse of each valid frame, we calculate the centroid (center of gravity) by the weighted time average method. Then we adjust the time axes of the frames by aligning the centroids of the trigger pulses for 2000 valid frames and simultaneously accumulate spikes of the starlight and red light to form the waveforms of the starlight and the red light pulses. Because the PMT operated in the photon counting mode, we only take the peak value of the spike during the accumulation process. We apply Gaussian fitting to the red light waveform to obtain the centroid. After finishing this process for the entire set of starlight measurement frames, we align the centroids of the fitted red light pulses to reconstruct the complete waveforms of the starlight and the red light pulses. We follow the same procedure to reconstruct the pulse waveforms of the terrestrial white light and the red light. Finally we again use Gaussian fitting to estimate the centroids of the starlight, white light, and red light pulses. We applied different fitting methods and obtained a similar result.

In the spring of 2013, we used the similar setup as shown in Fig. 7.2 to measure the speed of starlight, where we omitted the red light and used the 1550 nm as the trigger and the reference signals. We obtained the similar result as the previous ones.

Table 7.2 summarizes the estimated arrival time delays respect to the white light for Aldebaran, Capella, Arcturus, and Vega measured in 2013. Table 7.3 summarizes the average delays of the starlight measured in 2010, 2011, 2012, and 2013. Note that if the starlight pulses arrive at the receiver earlier than the terrestrial white light pulses, the delay value is negative, e.g. the Vega pulses.

The pulses of Aldebaran, Capella, and Betelgeuse have positive delays and that of Vega and Arcturus have negative delays. As shown in Table 7.1, the relative radial velocities of Aldebaran, Capella, and Betelgeuse are positive, but that of

Table 7.2 The estimated time delays of starlight measured in 2013

Aldebaran	Capella	Arcturus	Vega
2.13 ns (March 08)		0.74 ns (March 08)	−1.32 ns (March 08)
2.16 ns (March 09)		−1.46 ns (March 09)	−1.93 ns (March 09)
3.76 ns (March 10)			
	1.21 ns (March 12)	0.58 ns (March 12)	
	1.51 ns (March 15)		−1.19 ns (March 15)
	1.64 ns (March 16)		

Table 7.3 The average delays of starlight measured in 2010, 2011, 2012 and 2013

	Delays (ns)			
	2010	2011	2012	2013
Aldebaran				2.68
Capella	2.28	2.41	4.57	1.45
Betelgeuse	1.19	1.80		
Arcturus	−0.45	−4.01		−0.19
Vega	−1.35	−7.40		−1.48

Vega and Arcturus are negative. Because we had laid the equipment on the floor of the Lulin Observatory, the ambient temperature and the relative humidity made the floor contraction or expansion which affected the measurement. The errors of delays of Arcturus in 2011, Vega in 2011, and Capella in 2012 are large.

7.5 System Error Analysis

In this section, we investigate possible factors that may cause measurement errors. Ideally the white light delays should be a constant value relative to the red light. Practically we laid the system on the concrete floor of the Lulin Observatory. The changes of temperature and relative humidity made the concrete floor expansion or contraction. Therefore the relative positions of the components changed slightly which affected the value of the white light delay with respect to the red light. In addition, the white light is much stronger than the starlights. So the fitting error is very small. We use the white light delays for establishing the quadratic fitting curve to estimate the thermal effect.

Every night we recorded the temperature and relative humidity. For example, Figs. 7.4 and 7.5 show the temperature and relative humidity from 16:00 March 18 to 05:00 March 19, 2010. To estimate the effect of temperature and humidity

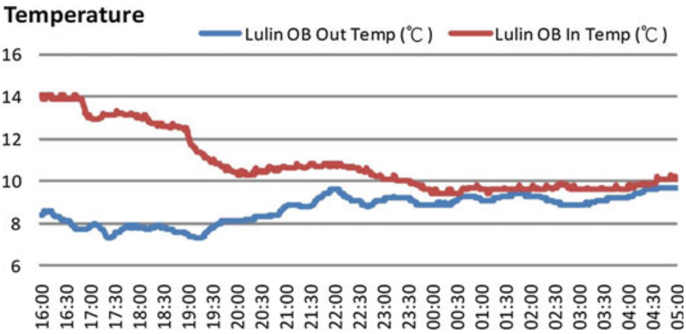

Fig. 7.4 The inside and outside temperatures of the building from 16:00 March 18 to 05:00 March 19, 2010

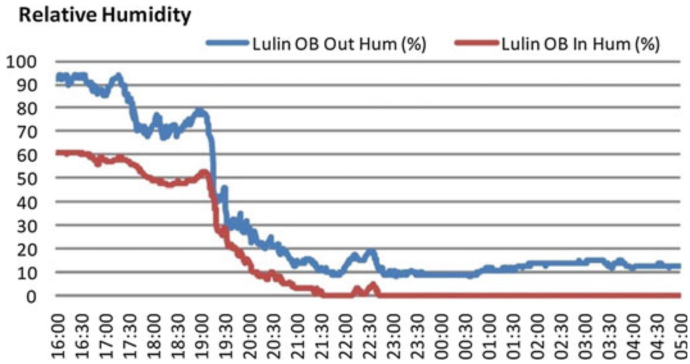

Fig. 7.5 The inside and outside relative humidity of the building from 16:00 March 18 to 05:00 March 19, 2010

changes on our measurement, we set the center of the floor as the origin of the polar coordinates. For convenience, to calculate the floor contraction, we assume that all stages move along their own radial coordinates, R, respectively. We can define that Δt is the difference of temperature in the period, α is the thermal expansion coefficient, so there is a displacement of $R \propto \Delta t$ along the radial coordinate, and a tilt angle of each stage also occurred at the same time because the displacements in the two ends of these stages are not exactly the same.

We estimate that the floor temperature changed accordingly through air convection with a delay of about one hour, and the relative humidity of floor changed with a delay of about three hours. Then we let the rotating mirror spin at about 17,929 rpm. Therefore we can calculate the varying degrees of arrival times shown as Fig. 7.6. The lower relative humidity of floor may make the thermal expansion coefficient smaller, so we can see the curve dropped from about 01:00 March 19, 2010. However, during the measurement, we employ a local white light to calibrate

Fig. 7.6 The estimated change of arrival time interval from 20:00 March 18 to 05:00 March 19, 2010

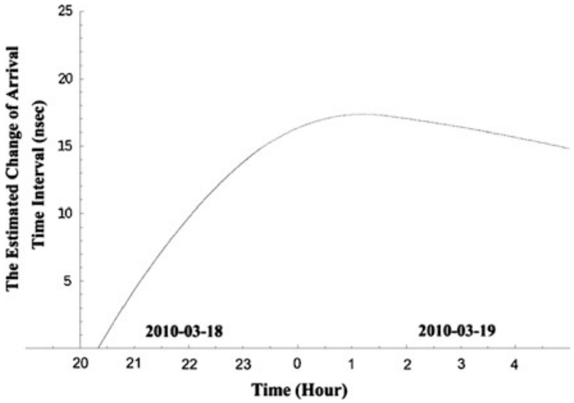

the system, so we can reduce the error. Each night the temperature and humidity change differently. So the form of the curve is different.

As mentioned above, the changes of temperature and humidity will affect the delays of the white light and starlights with respect to the red light and the trigger signals. However, the concrete floor expands or contracts slowly even the temperature and humidity fluctuate more rapidly. During the measurement, we alternatively measured the starlights and the white light. Then we could estimate the starlights delays.

The optical intensities over the cross sections of the outputs of the 9 and 4 μm single mode fibers are Gaussian distributed, so there is no speckle. The starlights with some very fine absorption lines and the white light have broadband spectra. So no speckle occurs at the output of the 5-m 68 μm fiber, which is verified experimentally. The spectrum of Capella is smooth except some absorption lines from the atmosphere which is shown in Fig. 7.7. The white light spectrum is positively smooth from an incandescent lamp light source shown as Fig. 7.8. Then we can estimate the effect of the air dispersion on our measurement. The refractive index of air under given conditions of wavelength, humidity, pressure, and temperature can be expressed as [13, 14]

$$n = n_{tp} - 10^{-10}[(292.75)(T + 273.15)]\left[3.7345 - \frac{0.0401}{\lambda^2}\right]\left(\frac{RH}{100}\right)P_{SV} \quad (7.12)$$

where n_{tp} is the refractive index of air at temperature very near 19.6 °C, T is the temperature in Celsius, λ is the wavelength in μm, RH is the relative humidity in percent, and P_{SV} is the saturation water vapor pressure in pascal. The detailed description of (7.12) is given in [13, 14].

The air pressure was about 0.75 atm at the Lulin Observatory. We divided the spectra of white light source and stars from 400 to 800 nm into 400 slices. Each slice has a spectral width of 1 nm which can be used to calculate the refractive index

Fig. 7.7 The measured spectrum of Capella

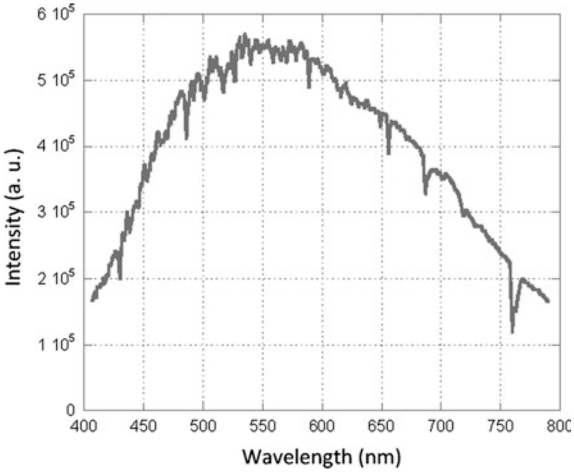

Fig. 7.8 The measured spectrum of the white light

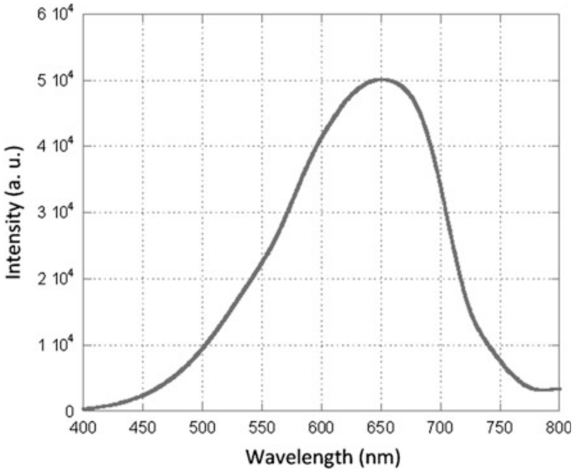

at different spectrum. The relative humidity and temperature change in the periods of measuring the adjacent two data. Using (7.12), we can calculate the errors of arrival time intervals, and get the maximum error from the air dispersion effect. For example, the estimated arrival time delay with respect to the white light for Capella is 3.9208 ns measured in the night of March 18, 2010. To estimate the dispersion error of Capella in that night, we calculate the theoretical difference of the dispersive pulses from Capella and the adjacent white light. The temperature and relative humidity have been recorded as Figs. 7.4 and 7.5, we find that the theoretical air dispersion errors for Capella are all in the range from −13.63 to −14.44 ps, and then we add the difference to the measured value 3.9208 ns to obtain the possible delays from 3.9344 to 3.9352 ns. Similarly for Vega measured in the night of March 18, 2010, we find that the air dispersion errors are in the range from −192.21 to 192.21 ps, and then we add the difference to the measured value −3.2150 ns to obtain the possible delays from −3.4072 to −3.0228 ns. In addition, we also calculate the effect of speed variation of the rotating mirror, PMT response time, amplifier bandwidth, and jitter of the oscilloscope. Totally they only induced a few sub-nanoseconds deviation.

7.6 Conclusions

In this paper, we presented a novel method to measure the speeds of starlight. This method compares the travelling times of these starlights and the local white light from the transmitter to the receiver. Such that physical unit transformation, clock synchronization and definitions of dimension units problems can be avoid. This system utilizes the existing telescope of the observatory, the orbiting speed of the earth, and the radial velocities of stars. Comparing the measured apparent speeds of

Aldebaran, Capella, Betelgeuse, Arcturus, and Vega with the well-known speed of light from a rest source, *c*, we find that Aldebaran, Capella, and Betelgeuse have positive delays, while Vega and Arcturus have negative delays. Note that Aldebaran, Capella, and Betelgeuse have positive relative radial velocities, Vega and Arcturus have negative relative radial velocities, i.e. Aldebaran, Capella, and Betelgeuse are leaving away from the earth and Vega and Arcturus are approaching to the earth. The result implies the measured apparent speed of starlight likely relates to the relative motion of the source and the detector.

Acknowledgements The authors are grateful for Professor Wen-Ping Chen, Director Hung-Chin Lin, and the staff of the Lulin Observatory of National Central University to provide the facilities and the necessary help. This work was supported in part by Excellent Research Projects of National Taiwan University and the Nation Science Council, Taiwan, under Grants 98R0062-06, NSC 100-2221-E-002-035- and NSC 101-2221-E-002-002.

References

1. K.D. Froome, L. Essen, *The Velocity of Light of Radio Waves* (Academic Press, New York, USA, 1969)
2. J.H. Sanders, *The Velocity of Light* (Pergamon Press Ltd., Oxford, UK, 1965)
3. A.P. French, *Special Relativity* (W.W. Norton & Company Inc., New York, USA, 1968)
4. W. Ritz, Amn. de Chim, et de Phys. **13**, 145–275 (1908)
5. G. Torres, A. Claret, P.A. Young, Astrophys. J. **700**, 1349 (2009)
6. R.E. Wilson, *General Catalogue of Stellar Radial Velocities* (Carnegie Institution of Washington Publication, Washington, D. C., USA, 1963)
7. SIMBAD Astronomical Database, (from http://simbad.u-strasbg.fr/simbad/.)
8. J. Wu, S.-T. Chang, H.-W. Tsao, Y.-R. Huang, S.-L. Lee et al., Testing the constancy of the velocity of light. Am. Phy. Soc. (2012) (April Meeting, Atlanta, USA)
9. Y.-R. Huang, J. Wu, W.-C. Lin, S.-T. Chang, S.-L. Lee, H.-W. Tsao et al., *An Optical System of Comparing the Speeds of Lights from Moving Stars* (ODF 12, Saint-Petersburg, Russia, 2012)
10. J. Wu, S.-T. Chang, H.-W. Tsao, Y.-R. Huang, S.-L. Lee et al., *A Method of Comparing the Speed of Starlight and the Speed of Light from a Terrestrial Source* (SPIE Optics + Photonics 2013, San Diego, USA, 2013)
11. Y.-R. Huang, J. Wu, S.-T. Chang, H.-W. Tsao, S.-L. Lee, W.-C. Lin, *Measurement of Differences and Relativity between Speeds of Light from Various Stars* (APPC 12, Chiba, Japan, 2013)
12. J. Wu, Y.-R. Huang, S.-T. Chang, H.-W. Tsao, S.-L. Lee, W.-C. Lin, *The Novel Optical System of Measuring the Speed of Starlight* (PHOTOPTICS 2014, Lisbon, Portugal, 2014)
13. B. Edlén, Metrologia **2**, 71–80 (1966)
14. J.A. Stone, J.H. Zimmerman, *Index of Refraction of Air* (NIST web page) (http://emtoolbox.nist.gov/Wavelength/Abstract.asp)

Chapter 8
Performance Evaluation of Optical Noise-Impaired Multi-band OFDM Systems Through Analytical Modeling

Pedro E.D. Cruz, Tiago M.F. Alves and Adolfo V.T. Cartaxo

Abstract The performance evaluation through analytical modeling of virtual carrier-assisted direct-detection single-sideband multi-band orthogonal frequency division multiplexing (MB-OFDM) systems dominantly impaired by amplified spontaneous emission noise is presented. An analytical expression is obtained for the bit error ratio (BER) of these systems, using the analytical relationship between the electrical signal-to-noise ratio and the optical signal-to-noise ratio. In order to analyse the accuracy of the analytical expression, the BER estimates provided by the analytical model are compared with the ones obtained using numerical simulation and the exhaustive Gaussian approach. Excellent agreement between the BER estimates is verified when distortion does not affect significantly the performance of the MB-OFDM signal.

8.1 Introduction

Orthogonal frequency division multiplexing (OFDM) has been widely appointed as a powerful solution to provide capacity granularity and switching capabilities in optical networks [1–3]. Flexible bandwidth allocation was also identified as one of the main advantages of OFDM-based networks [4, 5]. Optical communication systems have also exploited the advantages of high spectral efficiency and resilience to linear fiber effects that OFDM can offer [4, 6]. Two different optical OFDM

P.E.D. Cruz (✉) · T.M.F. Alves · A.V.T. Cartaxo
Department of Electrical and Computer Engineering, Instituto Superior Técnico,
Optical Communications and Photonics Group, Instituto de Telecomunicações,
Universidade de Lisboa, Av. Rovisco Pais, 1, 1049-001 Lisbon, Portugal
e-mail: pedro.cruz@lx.it.pt

T.M.F. Alves
e-mail: tiago.alves@lx.it.pt

A.V.T. Cartaxo
e-mail: adolfo.cartaxo@lx.it.pt

P.A. Ribeiro and M. Raposo (eds.), *Photoptics 2014*,
Springer Proceedings in Physics 177, DOI 10.1007/978-3-319-27321-1_8

flavors have been considered in the literature: (i) coherent-detection, where a local oscillator, hybrid couplers and several photodetectors are employed at the optical receiver, and (ii) direct-detection, where only one photodetector is required at the receiver. For systems where cost is of primary concern, such as in metropolitan networks, OFDM systems employing direct-detection are preferred [7].

Although optical OFDM systems have been widely studied, the implementation of multi-band OFDM (MB-OFDM) using direct-detection is a relatively new concept [8, 9]. A high-speed (>100 Gb/s) MB-OFDM system using a direct-detection optical OFDM superchannel (several OFDM bands) with dual carriers at both sides of the superchannel is proposed in [8] for long-haul networks. In that work, an analytical form to get the optimum carrier-to-signal power ratio is obtained in optical back-to-back, where only linear noise is considered. This kind of analytical formulation is of special interest as it allows obtaining a first estimate of system performance without requiring extensive numerical simulations to acquire the results. Although the system presented in [8] has high spectral efficiency, it is quite challenging to implement this MB-OFDM system in flexible metropolitan networks mainly due to huge requirements for the receiver front-end bandwidth. The optical OFDM superchannel proposed in [9], which is a variant of the MB-OFDM direct-detection long-haul system of [8], proposes the use of multiple carriers along the superchannel. In [9], a carrier supports a few OFDM bands, targeting ultra-high capacity with more relaxed receiver front-end bandwidth requirements, when comparing with the system of [8]. These two MB-OFDM systems [8, 9] have proposed and demonstrated effective direct-detection solutions for long-haul networks. This paper considers a different MB-OFDM system, where one carrier supports one OFDM band. In this system, the pair OFDM band-carrier is selected by optical filtering before direct detection, reducing the required bandwidth of the front-end receiver significantly, when comparing with the receiver bandwidth requirements of the systems presented in [8, 9]. This MB-OFDM system presents some challenges that require investigation, such as the crosstalk originated by the finite selectivity of the optical filters or the effect of increasing the spectral efficiency by reducing the gap between the carrier and the OFDM band on the system performance.

In this work, the performance of an amplified spontaneous emission (ASE) noise-impaired direct-detection single-sideband (SSB) MB-OFDM system employing a virtual carrier per OFDM signal is analytically modeled, by using the bit error ratio (BER) as figure of merit. Operation in optical back-to-back is considered, as optical fiber impairments should not present remarkable influence on the performance of SSB systems.

8.2 System Description

The model considered to describe the MB-OFDM system in optical back-to-back is presented in Fig. 8.1.

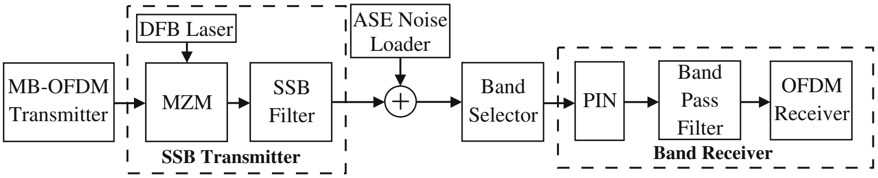

Fig. 8.1 MB-OFDM system model in optical back-to-back. *ASE* amplified spontaneous emission; *DFB* distributed feedback; *MZM* Mach-Zehnder modulator; *PIN* positive-intrinsic-negative; *SSB* single-sideband

The radiofrequency (RF) MB-OFDM signal generated at the MB-OFDM transmitter is composed by N_B OFDM signals (or bands) and N_B RF carriers (or virtual carriers—VCs), as depicted in Fig. 8.2.

The MB-OFDM system considers one VC per OFDM band. Each pair band-VC does not interfere in frequency with the corresponding neighboring pairs. The virtual-carrier-to-band gap (VBG) is selected in order to avoid the signal-signal beat interference (SSBI) originated by the photodetector square-law. A MB-OFDM system design with the VC at a higher frequency than the corresponding OFDM band is considered. At the SSB transmitter, the optical signal is generated by a distributed feedback (DFB) laser and the MB-OFDM signal modulates that optical signal using a chirpless Mach-Zehnder modulator (MZM), biased at quadrature point. The optical signal at the MZM output is then filtered by a SSB filter, creating a SSB signal. This allows overcoming the chromatic dispersion-induced power fading impairment caused by the square-law photodetection of a double-sided optical signal transmitted along a dispersive medium. After SSB filtering, an ASE noise loader adds optical noise to the MB-OFDM signal. After ASE noise addition, the band and VC to be dropped at the receiver are selected by the band selector (BS) optical filter. The band receiver is composed by a positive-intrinsic-negative (PIN) photodetector, a band pass filter (BPF) and an OFDM receiver. The PIN converts the optical signal to an electrical signal. The BPF removes the out-of-band noise and filters the received OFDM signal, and the OFDM receiver digitally-converts and demodulates the electrical signal.

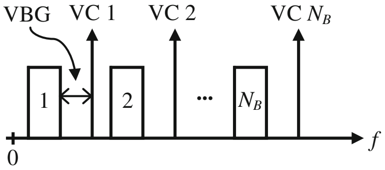

Fig. 8.2 Simplified scheme of a MB-OFDM signal, with N_B bands and N_B VCs. *VBG* virtual-carrier-to-band gap

8.3 Analytical Modeling

In this section, the analytical modeling of the signal and noise power along the MB-OFDM system is performed. The main objective is to obtain analytical expressions for the optical signal-to-noise ratio (OSNR) and the electrical signal-to-noise ratio (ESNR) at the BPF output. With these expressions, fast BER estimates can be obtained to provide insight on the performance of SSB MB-OFDM systems employing direct-detection.

The RF signal at the MZM input, $\upsilon_{RF}(t)$, can be written as:

$$\upsilon_{RF}(t) = \underbrace{[s_b(t) + A_\upsilon s_\upsilon(t)]}_{s_e(t)} \frac{V_{RMS,imp}}{V_{RMS,s_e(t)}}, \tag{8.1}$$

with

$$s_b(t) = \sum_{n=1}^{N_B} \frac{s_{b,n}(t)}{V_{RMS,s_{b,n}(t)}}, \tag{8.2}$$

and

$$s_\upsilon(t) = \sum_{n=1}^{N_B} \frac{s_{\upsilon,n}(t)}{V_{RMS,s_{\upsilon,n}(t)}}, \tag{8.3}$$

where $s_b(t)$ is the sum of all up-converted N_B OFDM band signals, A_υ is the amplitude of each VC, $s_\upsilon(t)$ is the sum of all N_B VCs, $s_{b,n}(t)$ is the nth OFDM band, $V_{RMS,s_{b,n}(t)}$ is the root-mean-square (RMS) voltage of $s_{b,n}(t)$, $s_{\upsilon,n}(t)$ is the nth VC, $V_{RMS,s_{\upsilon,n}(t)}$ is the RMS voltage of $s_{\upsilon,n}(t)$, $s_e(t)$ is the MB-OFDM signal, $V_{RMS,s_e(t)}$ is the RMS voltage of $s_e(t)$, and $V_{RMS,imp}$ is the RMS voltage imposed to the MB-OFDM signal at the MZM input. As a note, $\upsilon_{RF}(t)$ can be written as:

$$\upsilon_{RF}(t) = s_{b,e}(t) + s_{\upsilon,e}(t), \tag{8.4}$$

with

$$\begin{cases} s_{b,e}(t) = \frac{V_{RMS,imp}}{V_{RMS,s_e(t)}} s_b(t), \\ s_{\upsilon,e}(t) = \frac{V_{RMS,imp} A_\upsilon}{V_{RMS,s_e(t)}} s_\upsilon(t), \end{cases} \tag{8.5}$$

and the mean power of $\upsilon_{RF}(t)$, p_{RF}, is given by:

$$p_{RF} = V^2_{RMS,imp}. \tag{8.6}$$

The output electrical field of a chirpless MZM, $e_{MZM}(t)$, can be expressed as:

$$e_{MZM}(t) = E_i \cos\left\{\frac{\pi}{2V_\pi}\left[-V_b + \upsilon_{RF}(t)\right]\right\} \exp(j2\pi\nu_0 t), \tag{8.7}$$

where E_i is the optical field at the MZM input, V_b is the MZM bias voltage, V_π is the voltage required to switch between the maximum and the minimum of the MZM power transmission characteristic, and ν_0 is the optical frequency.

Considering a linearized MZM by applying the Taylor series first-order approximation around zero with respect to $\upsilon_{RF}(t)$, and that the MZM is biased at quadrature point ($V_b = V_\pi/2$), the linearized output field, $e_{MZM,l}(t)$, can be written as:

$$e_{MZM,l}(t) = E_i\left[\frac{\sqrt{2}}{2} + \frac{\sqrt{2}}{4}\frac{\pi}{V_\pi}\upsilon_{RF}(t)\right] \exp(j2\pi\nu_0 t). \tag{8.8}$$

Using (8.4) and (8.5), and knowing that:

$$\begin{cases} \left\langle |s_b(t)|^2 \right\rangle = \left\langle |s_\upsilon(t)|^2 \right\rangle = N_B, \\ V^2_{RMS,s_e(t)} = N_B(1 + A^2_\upsilon), \end{cases} \tag{8.9}$$

the mean power at the linearized MZM output, $p_{MZM,l}$, can be expressed as:

$$p_{MZM,l} = \underbrace{\frac{E_i^2}{2}}_{p_o} + \underbrace{\frac{1}{8}\frac{\pi^2}{V_\pi^2}E_i^2\frac{V^2_{RMS,imp}}{1 + A^2_\upsilon}}_{p_b} + \underbrace{\frac{1}{8}\frac{\pi^2}{V_\pi^2}E_i^2\frac{V^2_{RMS,imp}}{1 + A^2_\upsilon}A^2_\upsilon}_{p_\upsilon}, \tag{8.10}$$

where p_0 is the optical carrier mean power, p_υ is the mean power of all the VCs, and p_b is the mean power of all the OFDM bands.

Two important power ratios can be determined from (8.10), which are the virtual-carrier-to-band power ratio (VBPR) and the optical-carrier-to-band power ratio (OBPR). These ratios are important because they have a significant impact on the performance of the MB-OFDM signal. The VBPR is given by:

$$\mathrm{VBPR} = \frac{p_\upsilon}{p_b} = \frac{p_{\upsilon,n}}{p_{b,n}} = A^2_\upsilon, \tag{8.11}$$

and the OBPR can be written as:

$$\mathrm{OBPR} = \frac{p_o}{p_b} = \frac{4V_\pi^2(1 + \mathrm{VBPR})}{\pi^2 V^2_{RMS,imp}}, \tag{8.12}$$

where $p_{\upsilon,n} = p_\upsilon/N_B$ and $p_{b,n} = p_b/N_B$ are the mean power of the VCn and the OFDM band n, respectively.

After electro-optical conversion, SSB filtering is performed and the lower sideband and lower VC are removed. After some calculations, the mean power at the SSB filter output, p_{SSB}, can be expressed as:

$$p_{SSB} = p_o + \frac{p_\upsilon}{2} + \frac{p_b}{2}. \tag{8.13}$$

Afterwards, an ASE noise loader is added to the signal at the SSB filter output. Hence, it is important to define the OSNR after noise loading (NL).

Considering that the ASE noise is zero-mean additive-white-Gaussian and is present in the parallel (||) and perpendicular (⊥) polarization directions, and that the signal field at the SSB filter output is polarized in the parallel direction, the low pass equivalent (LPE) of the field after NL, $\mathbf{e}_{NL}(t)$, can be expressed as:

$$\mathbf{e}_{NL}(t) = \left[e_{SSB,\|}(t) + n_{I,\|}(t) + j\,n_{Q,\|}(t)\right]\mathbf{u}_\| + \left[n_{I,\perp}(t) + j\,n_{Q,\perp}(t)\right]\mathbf{u}_\perp, \tag{8.14}$$

where $e_{SSB,\|}(t)$ is the OFDM signal field at the SSB filter output in the $\|$ polarization defined by $\mathbf{u}_\|$, $n_{I,\|}(t)$ and $n_{Q,\|}(t)$ are the I and Q noise components in the $\|$ polarization, respectively, and $n_{I,\perp}(t)$ and $n_{Q,\perp}(t)$ are the I and Q noise components in the $\perp$ polarization defined by $\mathbf{u}_\perp$, respectively.

Assuming that each one of the four noise components has a constant power spectral density (PSD) given by S_{ASE}, the optical noise mean power in a bandwidth B_N after NL, $p_{n,NL}$, can be expressed as:

$$p_{n,NL} = 4S_{ASE}B_N. \tag{8.15}$$

Usually, B_N corresponds to a reference bandwidth of 0.1 nm, which is approximately 12.5 GHz.

The OSNR is defined as the ratio between the signal power after NL, $p_{s,NL}$ (which is equal to the signal power at the SSB filter output, p_{SSB}), and the noise mean power, $p_{n,NL}$, in the reference bandwidth B_N, after NL. Considering (8.13) and (8.15), the OSNR is then expressed as:

$$\text{OSNR} = \frac{p_{s,NL}}{p_{n,NL}} = \frac{p_{SSB}}{p_{n,NL}} = \frac{p_o + \frac{p_\upsilon}{2} + \frac{p_b}{2}}{4S_{ASE}B_N}. \tag{8.16}$$

After ASE noise loading, the BS is used to select the OFDM band and VC that will be photodetected (dropped). The BS is an ideal optical filter, with transfer function $H_{BS,n}(f)$ and impulse response $h_{BS,n}(t)$, that only selects the nth OFDM signal and the nth VC. The LPE of $H_{BS,n}(f)$ can be written as:

$$H_{BS,n}(f) = \text{rect}\left(\frac{f - f_x}{B_o}\right), \tag{8.17}$$

where B_0 is the BS bandwidth and f_x is the center frequency of the BS given by:

$$f_x = \frac{f_{\max} + f_{\min}}{2} = \frac{f_{\upsilon,n} + \left(f_{RF,n} - \frac{B_E}{2}\right)}{2}, \tag{8.18}$$

where $f_{\upsilon,n}$ is the nth VC frequency, $f_{RF,n}$ is the nth band central frequency, $f_{\max}$ and $f_{\min}$ are the maximum and minimum frequencies of the passband of the BS, respectively, and B_E is the OFDM signal bandwidth.

The LPE of the signal at the BS output, $\mathbf{e}_{BS,n}(t)$, can be expressed as:

$$\begin{aligned} \mathbf{e}_{BS,n}(t) &= \mathbf{e}_{NL}(t) \circledast h_{BS,n}(t) \\ &= \left[\mathbf{e}_{BS,n,\|}(t) + n'_{I,\|}(t) + jn'_{Q,\|}(t)\right]\mathbf{u}_{\|} + \left[n'_{I,\perp}(t) + jn'_{Q,\perp}(t)\right]\mathbf{u}_{\perp}, \end{aligned} \tag{8.19}$$

where $\circledast$ denotes the convolution operation, $e_{BS,n,\|}(t)$ is the field, at the BS output, of the nth OFDM signal and nth VC in the $\|$ polarization, $n'_{I,\|}(t)$ and $n'_{Q,\|}(t)$ are the filtered I and Q noise components in the $\|$ polarization, respectively, and $n'_{I,\perp}(t)$ and $n'_{Q,\perp}(t)$ are the filtered I and Q noise components in the $\perp$ polarization, respectively. The field $e_{BS,n,\|}(t)$ is given by:

$$\begin{aligned} e_{BS,n,\|}(t) = \frac{\sqrt{2}}{4}\frac{\pi}{V_\pi}E_i \Bigg[& \frac{V_{RMS,imp}}{V_{RMS,s_e(t)}V_{RMS,s_{b,n}(t)}} s_{b,n}(t) \\ & + \frac{V_{RMS,imp}A_\upsilon}{V_{RMS,s_e(t)}V_{RMS,s_{\upsilon,n}(t)}} s_{\upsilon,n}(t)\Bigg] \exp(j2\pi\nu_0 t), \end{aligned} \tag{8.20}$$

with

$$s_{b,n}(t) = s_{I,n}(t)\cos(2\pi f_{RF,n}t) - s_{Q,n}(t)\sin(2\pi f_{RF,n}t), \tag{8.21}$$

and

$$s_{\upsilon,n}(t) = \sqrt{2}\cos(2\pi f_{\upsilon,n}t + \phi_\upsilon), \tag{8.22}$$

where $s_{I,n}(t)$ is the low pass in-phase (I) component of the OFDM signal of band n, $s_{Q,n}(t)$ is the low pass quadrature (Q) component of the OFDM signal of band n, and ϕ_υ is the VC initial phase.

The field $e_{BS,n,\|}(t)$ has a mean power, $p_{BS,n}$, given as follows:

$$p_{BS,n} = \frac{p_\upsilon + p_b}{2N_B} = \frac{p_{\upsilon,n}}{2} + \frac{p_{b,n}}{2}. \tag{8.23}$$

After band selection, the signal is photodetected. The PIN model used in this work is a square modulus function with responsivity R_λ of 1 A/W. The photocurrent at the PIN output, $i_{PIN,n}(t)$, can be written as:

$$i_{PIN,n}(t) = |\mathbf{e}_{BS,n}(t)|^2 = \left| e_{BS,n,\|}(t) + n'_{I,\|}(t) + jn'_{Q,\|}(t) \right|^2 + |n'_{I,\perp}(t) + jn'_{Q,\perp}(t)|^2. \tag{8.24}$$

After some calculations, the PIN output current can be separated in two groups: the signal-dependent current and the noise-dependent current. The signal dependent current, denoted as $i_{s,PIN}(t)$, is given by:

$$\begin{aligned} i_{s,PIN}(t) = \frac{1}{8}\frac{\pi^2}{V_\pi^2}E_i^2 \times \Bigg[& \frac{1}{4}\left(\frac{V_{RMS,imp}}{V_{RMS,s_{b,n}(t)}V_{RMS,s_e(t)}}\right)^2 \left[s_{I,n}^2(t) + s_{Q,n}^2(t)\right] \\ & + \frac{\sqrt{2}}{2}\frac{V_{RMS,imp}^2 A_\upsilon}{V_{RMS,s_{b,n}(t)}V_{RMS,s_{\upsilon,n}(t)}V_{RMS,s_e(t)}^2} s_{PIN}(t) \\ & + \frac{1}{2}\left(\frac{V_{RMS,imp}A_\upsilon}{V_{RMS,s_{\upsilon,n}(t)}V_{RMS,s_e(t)}}\right)^2 \Bigg], \end{aligned} \tag{8.25}$$

with

$$s_{PIN}(t) = s_{I,n}(t)\cos\left[2\pi\left(f_{\upsilon,n} - f_{RF,n}\right)t\right] + s_{Q,n}(t)\sin\left[2\pi\left(f_{\upsilon,n} - f_{RF,n}\right)t\right]. \tag{8.26}$$

The first term of $i_{s,PIN}(t)$ is the SSBI, the second term is the received OFDM signal, and the third term is the direct-current (DC) component. The Fourier transform of $i_{s,PIN}(t)$, $I_{s,PIN}(f)$, is given by:

$$\begin{aligned} I_{s,PIN}(f) = \frac{1}{8}\frac{\pi^2}{V_\pi^2}E_i^2 \times \Bigg[& \frac{1}{4}\left(\frac{V_{RMS,imp}}{V_{RMS,s_{b,n}(t)}V_{RMS,s_e(t)}}\right)^2 S_d(f) \\ & + \frac{\sqrt{2}}{2}\frac{V_{RMS,imp}^2 A_\upsilon}{V_{RMS,s_{b,n}(t)}V_{RMS,s_{\upsilon,n}(t)}V_{RMS,s_e(t)}^2} S_{PIN}(f) \\ & + \frac{1}{2}\left(\frac{V_{RMS,imp}A_\upsilon}{V_{RMS,s_{\upsilon,n}(t)}V_{RMS,s_e(t)}}\right)^2 \delta(f) \Bigg], \end{aligned} \tag{8.27}$$

with $S_d(f) = \mathscr{F}\{s_{I,n}^2(t) + s_{Q,n}^2(t)\}$ and $S_{PIN}(f) = \mathscr{F}\{s_{PIN}(t)\}$, where $\mathscr{F}\{\cdot\}$ denotes the Fourier transform. The noise-dependent current, denoted as $i_{n,PIN}(t)$, where the noise-noise beat terms were neglected, can be expressed as:

$$i_{n,PIN}(t) = e_{BS,n,\|}(t)\left[n'_{I,\|}(t) - jn'_{Q,\|}(t)\right] + \left\{e_{BS,n,\|}(t)\left[n'_{I,\|}(t) - jn'_{Q,\|}(t)\right]\right\}^*. \tag{8.28}$$

In order to obtain the noise PSD at the PIN output, $S_{n,PIN}(f)$, the Fourier transform of the auto-correlation function of $i_{n,PIN}(t)$ must be evaluated. After performing some calculations, $S_{n,PIN}(f)$ is given by:

$$S_{n,PIN}(f) = 2S_{ASE}\left[\left|H_{BS,n}(f + f_{\upsilon,n})\right|^2 + \left|H_{BS,n}(-f + f_{\upsilon,n})\right|^2\right]p_{BS,n}. \tag{8.29}$$

After photodetection, a BPF is used to remove the SSBI and the DC component from the photodetected signal. The BPF transfer function, $H_{BPF}(f)$, is given by:

$$H_{BPF}(f) = \mathrm{rect}\left(\frac{f - f_{RF,n} + f_{\upsilon,n}}{B_E}\right) + \mathrm{rect}\left(\frac{f + f_{RF,n} - f_{\upsilon,n}}{B_E}\right), \tag{8.30}$$

where B_E is the BPF bandwidth, which is equal to the OFDM signal bandwidth. The Fourier transform, $I_{s,BPF}(f)$, of the signal at the BPF output, can be expressed as:

$$I_{s,BPF}(f) = I_{s,PIN}(f)H_{BPF}(f), \tag{8.31}$$

which is approximately given by:

$$I_{s,BPF}(f) \approx \frac{1}{8}\frac{\pi^2}{V_\pi^2}E_i^2\frac{\sqrt{2}}{2} \times \frac{V_{RMS,imp}^2 A_\upsilon}{V_{RMS,s_{b,n}(t)}V_{RMS,s_{\upsilon,n}(t)}V_{RMS,s_e(t)}^2}S_{PIN}(f)H_{BPF}(f). \tag{8.32}$$

After some calculations, the mean power of $I_{s,BPF}(f)$, $p_{s,BPF}$, can be written as:

$$p_{s,BPF} = \frac{p_{\upsilon,n}p_{b,n}}{2}. \tag{8.33}$$

The noise power at the BPF output can be obtained from the PSD of the noise at the PIN output (8.29) as:

$$p_{n,BPF} = \int_{-\infty}^{+\infty} S_{n,PIN}(f)\left|H_{BPF}(f)\right|^2 \mathrm{d}f = 4p_{BS,n}S_{ASE}B_E, \tag{8.34}$$

where B_E is the bandwidth of the low pass filter at the receiver (which has the greatest frequency limitation). The ESNR is defined as the ratio between the signal power, $p_{s,BPF}$, and the noise mean power, $p_{n,BPF}$, at the BPF output. Considering (8.33) and (8.34), the ESNR is then given by:

$$\mathrm{ESNR} = \frac{p_{s,BPF}}{p_{n,BPF}} = \frac{\frac{p_{\upsilon,n}p_{b,n}}{2}}{\left(\frac{p_{\upsilon,n} + p_{b,n}}{2}\right)4S_{ASE}B_E}. \tag{8.35}$$

8.4 Performance Evaluation Metric

Figure of merit used in this study to categorize the system performance is the BER, which can be estimated as a function of the ESNR with the following expression [8]:

$$\mathrm{BER} = \frac{1 - \frac{1}{\sqrt{M}}}{\log_2(\sqrt{M})} \operatorname{erfc}\left(\sqrt{\frac{3\,\mathrm{ESNR}\,\log_2(\sqrt{M})}{(M-1)\log_2(M)}} \right), \tag{8.36}$$

where erfc(·) is the complementary error function, and M is the number of distinct symbols of the quadrature amplitude modulation format. Knowing that $p_o/p_{b,n} = N_B \times \mathrm{OBPR}$, $p_v/p_{b,n} = N_B \times \mathrm{VBPR}$, $p_b/p_{b,n} = N_B$, and using (8.35) and (8.16), the ESNR can be expressed as:

$$\mathrm{ESNR} = \frac{1}{N_B} \frac{2}{(2 \times \mathrm{OBPR} + \mathrm{VBPR} + 1)} \frac{\mathrm{VBPR}}{(\mathrm{VBPR} + 1)} \frac{B_N}{B_E} \mathrm{OSNR}. \tag{8.37}$$

Some important conclusions can be derived from (8.37). Keeping OBPR and VBPR constant, the ESNR of one band is inversely proportional to N_B, which means that transmitting more than one band will require an OSNR increase proportional to the number of bands to achieve the same performance as when only one band is transmitted. An increase of VBPR (that also results in an OBPR increase, as the OBPR depends on the VBPR) will also lead to a higher required OSNR, to achieve the same performance obtained with low VBPR. The power attributed to the OFDM band decreases and the power assigned to the VC increases, meaning lower ESNR.

8.5 Numerical Results

The effectiveness of the proposed analytical model for MB-OFDM systems is assessed by comparing its estimates with the ones of numerical simulation using MATLAB. The OSNR that leads to a BER = 10^{-3} (OSNR_{req}) and the BER itself are used as figures of merit. To assess the analytical method (AM) accuracy, the BER obtained with the AM is compared with the BER retrieved from numerical simulation (NS) using the exhaustive Gaussian approach (EGA) [10]. In the analysis, each OFDM symbol has 128 subcarriers, each OFDM band has a bit rate of 5 Gb/s and a bandwidth of 2.5 GHz, the maximum total bit rate (assuming a maximum of 4 bands) is 20 Gb/s, and the following parameters are fixed: $M = 4$, $V_\pi = 5\mathrm{V}$, $B_E = 2.5$ GHz, $B_N = 12.5$ GHz, GHz, $f_{RF,n} \in [2.25, 8.25, 14.25, 20.25]$ GHz and $f_{v,n}$ [6, 12, 18, 24] GHz with $n \in [1\text{–}4]$.

The linearized MZM with the relationship between the applied voltage and field at the MZM output given by (8.8) is used in the numerical results. A particular study, in which a real MZM is considered in the simulation, is also performed and explicitly mentioned. The target of this particular study is to assess the validity range of the AM in presence of MZM distortion. With the real MZM, is important to impose that the VC frequencies are multiple of $f_{\upsilon,1}$ (in this work, $f_{\upsilon,1} = 6$ GHz), in order to guarantee that the inter-modulation products of the VCs do not interfere with the OFDM bands.

The number of bands affects significantly the performance of the MB-OFDM system, as it was concluded through analysis of (8.37). Figure 8.3 shows the OSNR_{req} as function of $V_{RMS,imp}$ for N_B = [1, 2, 4], obtained with the AM and with NS. A VBPR of 15 dB is imposed. Figure 8.3 shows that the AM results have excellent agreement with the ones obtained with NS. Figure 8.3 also demonstrates that when N_B doubles, the OSNR_{req} increases 3 dB. Figure 8.3 shows also that increasing $V_{RMS,imp}$ leads to a OSNR_{req} decrease, which is valid for this system because it does not exhibit MZM distortion.

Another parameter besides N_B that influence significantly the performance results is the VBPR. Figure 8.4 shows the OSNR_{req} as function of $V_{RMS,imp}$ for VBPR = [3, 9, 15] dB, with the AM and with NS. The MB-OFDM system has four bands (N_B = 4). Figure 8.4 shows an excellent agreement between the AM results and the NS results. Figure 8.4 also shows that increasing VBPR leads to an increase of the OSNR_{req}. This increase is higher for higher VBPRs.

In the results of Figs. 8.3 and 8.4, the VBG is selected in order to avoid the SSBI overlapping with the received OFDM band. However, it is important to verify the resilience of the AM when PIN distortion interferes with the information-bearing signal, as a smaller VBG means more spectral efficiency. Figure 8.5 shows the BER as function of the VBG width in GHz, for VBPR = [3, 9, 15] dB and $V_{RMS,imp} = 1500$ mV. The OSNR is 22.4 dB for VBPR = 3 dB, 25.9 dB for VBPR = 9 dB and 31.1 dB for VBPR = 15 dB. With these OSNR levels and as the AM does not take into account the PIN distortion, the BER obtained using the AM is 10^{-3} for all VBG widths. Therefore, Fig. 8.5 only shows the NS results.

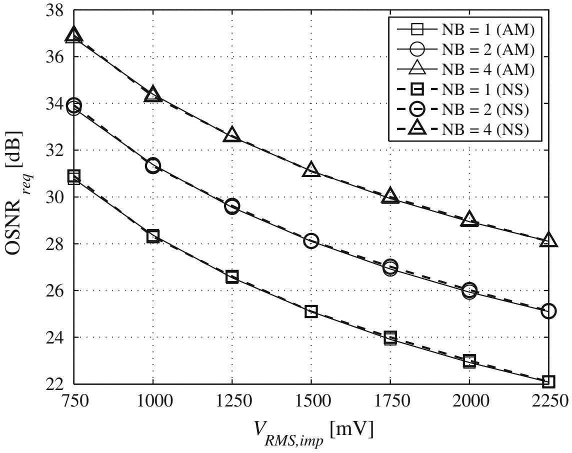

Fig. 8.3 OSNR_{req} as function of $V_{RMS,imp}$ for $N_B = [1, 2, 4]$, with AM (*solid lines*) and NS (*dashed lines*), with a fixed VBPR of 15 dB

Fig. 8.4 OSNR$_{req}$ as function of $V_{RMS,imp}$ for VBPR = [3, 9, 15] dB, with AM (*solid lines*) and NS (*dashed lines*), and with $N_B = 4$

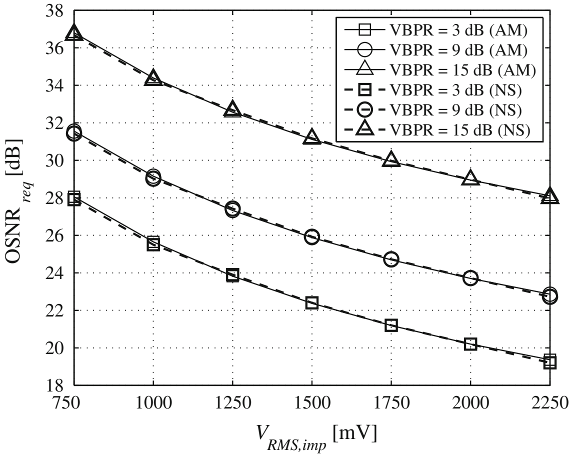

Figure 8.5 shows that the SSBI caused by the PIN affects the performance when the VBG width is lower than the bandwidth of the OFDM signal, as the SSBI spectrum overlaps the OFDM signal spectrum. Figure 8.5 shows also that the BER degrades more substantially for lower VBPRs. This is because lower VBPR levels leads to more SSBI power.

The results shown in Figs. 8.3, 8.4 and 8.5 present the effects of ASE noise and PIN distortion on the performance. However, the effects of MZM distortion were not considered in the simulation in those results as a linearized MZM is assumed in the analytical formulation. To illustrate the impact of MZM nonlinearity on the required OSNR and assess the validity range of the AM presented in this work, a real MZM described by (8.7) is considered in the simulation.

Figure 8.6 shows the OSNR$_{req}$ as function of the $V_{RMS,imp}$, for VBPR = [3, 9, 15] dB, and for the first band which is the most affected by MZM distortion. The

Fig. 8.5 BER as function of the VBG width, for VBPR = [3, 9, 15] dB and $V_{RMS,imp} = 1500$ mV, with NS. With the AM, the BER is 10^{-3} for all VBG widths

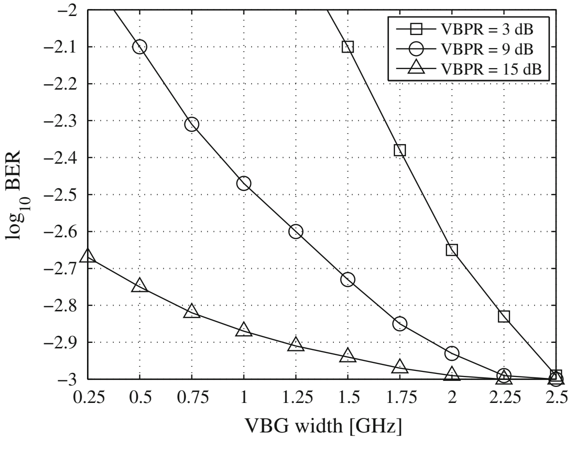

Fig. 8.6 OSNR_{req} as function of the $V_{RMS,imp}$, for VBPR = [3, 9, 15] dB. A MB-OFDM system with 4 bands ($N_B = 4$) is considered. A real MZM is considered in the simulation

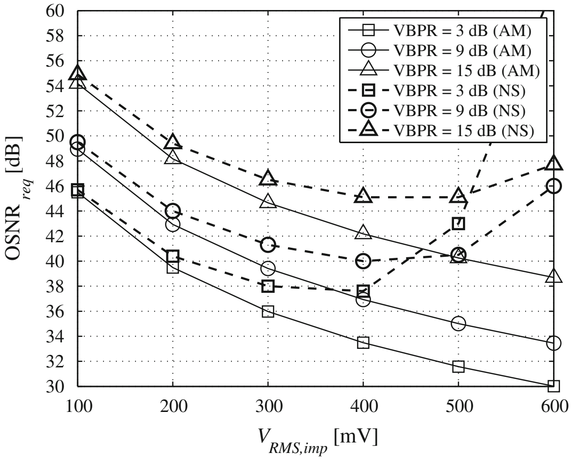

MB-OFDM system has four bands (N_B = 4), and a VBG width of 2.5 GHz is imposed. Figure 8.6 shows that the MZM distortion causes a performance degradation as the RMS voltage increases. For RMS voltages around 400 mV, the minimum OSNR_{req} is obtained. From the simulation results, the minimum OSNR_{req} for VBPR = 3 dB is 38 dB, for VBPR = 9 dB is 40 dB, and for VBPR = 15 dB is 45 dB. The error committed by the AM in the minimum OSNR_{req} is approximately 4 dB for VBPR = 3 dB and for VBPR = [9, 15] dB is approximately 3 dB. The analytical modeling of this work assumes noise-impaired MB-OFDM systems. Hence distortion-impaired systems are not well described by this model. This occurs for $V_{RMS,imp}$ higher than approximately 200 mV, which in modulation index ($V_{RMS,imp}/V_\pi$ in percentage) is 4 %.

8.6 Conclusions

An analytical model for performance evaluation of ASE noise-impaired direct-detection SSB MB-OFDM systems has been proposed. The effectiveness of the analytical model has been verified through comparison with numerical simulation using the EGA to evaluate the BER. Excellent agreement in the BER results when MZM and PIN distortion do not interfere with the MB-OFDM signal has been shown. When PIN distortion is affecting the MB-OFDM signal, the analytical model provides more accurate estimates for high VBPRs. When MZM distortion is interfering with the MB-OFDM signal, the analytical model presents a deviation in the required OSNR not exceeding 1 dB, for modulation indexes lower than 4 %. The analytical modeling for distortion-impaired MB-OFDM systems, as well as the MB-OFDM system optimization in order to achieve the best required OSNR, will be reported elsewhere.

Acknowledgements The work of Pedro Cruz was supported by Fundação para a Ciência e a Tecnologia from Portugal under Contract SFRH/BD/85940/2012 and by projects MORFEUS-PTDC/EEI-TEL/2573/2012 and PEst-OE/EEI/LA0008/2013.

References

1. N. Cvijetic, OFDM for next-generation optical access networks. J. Lightw. Technol. **30**, 384–398 (2012)
2. S. Blouza, J. Karaki, N. Brochier, E. Rouzic, E. Pincemin, B. Cousin, Multi-band OFDM for optical networking, Paper presented at the Int. Conf. Comput. Tool. doi:10.1109/EUROCON.2011.5929191
3. K. Christodoulopoulos, I. Tomkos, E. Varvarigos, Elastic bandwidth allocation in flexible OFDM-based optical networks. J. Lightw. Technol. **29**, 1354–1366 (2011)
4. J. Armstrong, OFDM for optical communications. J. Lightw. Technol. **27**, 189–204 (2009)
5. W. Shieh, OFDM for flexible high-speed optical networks. J. Lightw. Technol. **29**, 1560–1577 (2011)
6. A. Lowery, L. Du, J. Armstrong, Orthogonal frequency division multiplexing for adaptive dispersion compensation in long haul WDM systems. Paper presented at the Opt. Fiber Commun. Conf., paper PDF39 (2006)
7. S. Kim, K. Seo, J. Lee, Spectral efficiencies of channel-interleaved bidirectional and unidirectional ultradense WDM for metro applications. J. Lightw. Technol. **30**, 229–233 (2012)
8. W. Peng, I. Morita, H. Takahashi, T. Tsuritani, Transmission of high-speed (>100 Gb/s) direct-detection optical OFDM superchannel. J. Lightw. Technol. **30**, 2025–2034 (2012)
9. Z. Li, X. Xiao, T. Gui, Q. Yang, R. Hu, Z. He, M. Luo, C. Li, X. Zhang, D. Xue, S. You, S. Yu, 432-Gb/s direct-detection optical OFDM superchannel transmission over 3040-km SSMF. IEEE Photon. Technol. Lett. **25**, 1524–1526 (2013)
10. T. Alves, A. Cartaxo, Extension of the exhaustive Gaussian approach for BER estimation in experimental direct-detection OFDM setups. Microw. Opt. Technol. Lett. **52**, 2772–2775 (2010)

Part II
Photonics

Chapter 9
Delayed Luminescence in Relation to the Germination and Vigour of Coffee Seeds: Initial Series with *C. Arabica* Samples

Cristiano M. Gallep, Lilian Padilha, Mirian P. Maluf and Sttela D.V.F. da Rosa

Abstract Ultra-weak delayed luminescence measurements on coffee seeds were run for samples submitted to different post-harvest treatments or in seed lots with different vigour levels obtained by accelerated aging, and both were induced to germinate afterwards. Parameters of hyperbolic decay fitting were correlated to the correspondent germination vigour, with a linear relation found for the initial value as well as for the decay velocity. These preliminary data point to further, broader validation for this non-invasive, non-destructive test for seed's viability analyses.

9.1 Introduction

The coffee seed normally presents high germination potential just after appropriate harvest and desiccation. However, it also loses its physiological quality very rapidly under common storing conditions. Therefore, it is not possible to have viable seeds, i.e. able to germinate, for more than some months [1].

Some techniques may improve seed's viability on long term, by improving storing conditions [2, 3], or controlling the re-hydration process [4] or even inducing low-temperature hibernation [5].

Although some progress was achieved in this sense the usual way for checking seeds' viability and vigour is to allow them to germinate, i.e. losing so the hibernation condition. Furthermore, the results from germination tests are only available in 30 days after imbibition. So, new strategies able to save time are crucial in

---

C.M. Gallep (✉)
Applied Photonics Lab, School of Technology, University of Campinas, Limeira, SP, Brazil
e-mail: gallep@ft.unicamp.br

L. Padilha · M.P. Maluf · S.D.V.F. da Rosa
Brazilian Agricultural Research Corporation, Embrapa/Coffee Unit, Brasilia, DF, Brazil
e-mail: lilian.padilha@embrapa.br

P.A. Ribeiro and M. Raposo (eds.), *Photoptics 2014*,
Springer Proceedings in Physics 177, DOI 10.1007/978-3-319-27321-1_9

determining the proper actions for the conservation and commercialization of coffee seeds. In order to distinguish between viable and not viable seeds, and so enable an optimization of seed's storage conditions, a quick and non-destructive method is demanded, as well for other types of sensitive seeds.

The biophotonic phenomena, i.e. the ultra-weak delayed luminescence and spontaneous emission found in living organisms, with detected intensity of 10–1000 photons/cm^2 s, has been studied by many multi-disciplinary groups all over the world, in a broad variety of themes [6]. This peculiar luminescence holds much longer than the usual bio-fluorescence, and is found far from normal thermal black-body emission, covering the entire visible spectrum and the near IR and UV [7].

Correlations between the ultra-weak delayed luminescence (DL) behaviour and the germination capacity were found already for barley [8], soybean [9], rice [10] and wheat [11] seeds. A first, small trial with coffee seeds were performed by the first author ten years ago at IIB facilities (Neuss, Germany), with some indicative results of good correlation between the DL parameters and the germination capacity of tested seeds [12]. At that time, just three different lots were tested, with medium and high germination capacity.

Here, preliminary series of ultra-weak DL measurements of coffee seeds are presented in relation to their germination rate and total seedling elongation measured in the hypocotyl-radicle axis. Seeds submitted to different post-harvest treatments and seed lots with different vigour levels were tested for delayed luminescence, and induced to germinate afterwards.

The germination performance was established after 15 and 30 days and correlated to DL parameters. Good correlation was found between the germination vigour and the initial intensity and the decay velocity of the correspondent DL curves.

9.2 Materials and Methods

Initially, the DL of nine groups of coffee seeds (*Coffea Arabica*), harvested in June/2011 and treated in different conditions, were analysed in terms of hyperbolic decay in May/2013, and further induced to germinate in controlled conditions.

These seeds were harvest, processed and stored in controlled conditions at Federal University of Lavras (UFLA, MG, Brazil). The different seed groups ('A' series) are presented at Table 9.1—if mucilage is removed mechanically or by fermentation, if drying was done in drying machine, in shadow or under sun-light, and the moisture content achieved after drying (12 % or 35 %).

In a second series of tests, 'B', nine seed lots from Seed Analysis Laboratory-UFLA were submitted to accelerated ageing test (42 °C, 100 % relative humidity, for 48 h) to produce lots with different vigour levels, as presented at Table 9.2. Germination tests were run before and after the seed aging to evaluate the seed performance. DL tests were run in June/2013.

Table 9.1 Coffee seed groups ‘A’—different post-harvest treatments

Group	Post-harvest treatment	Moisture content (%)
A7	mechanical removal of mucilage, mechanical dryer	12
A9	mechanical removal of mucilage, dried in shadow	12
A11	mechanical removal of mucilage, sun-dried	12
A13	removal of mucilage by fermentation, mechanical dryer	12
A14	removal of mucilage by fermentation, mechanical dryer	35
A15	removal of mucilage by fermentation, dried in shadow	12
A16	removal of mucilage by fermentation, dried in shadow	35
A17	removal of mucilage by fermentation, sun-dried	12
A18	removal of mucilage by fermentation, sun-dried	35

Table 9.2 Coffee seed groups ‘B’—accelerated aging test

Sample	Germination rate (%)		Rating (vigour)
	Initial	Aged[a]	
1	74	41	Low
2	86	83	High
3	85	78	High
4	78	77	Medium
5	78	80	High
6	71	75	Medium
7	76	75	Medium
8	82	80	High
9	82	89	High

[a] Accelerated aging test: seeds under 48 °C/100 % R.H. for 48 h

Random samples of 50 g were taken from each seed group for the ultra-weak DL measurements and stored in dark to avoid artefacts. The experimental setup for DL tests are shown at Fig. 9.1; it is a dark chamber with photon-count module (photomultiplier tube + electronics) and a fiber optic ring connect to external light source (halogen lamp) by a fiber cable and electrical-mechanical shutter, all automatic controlled by software; it includes also temperature control for samples using fluid flow [13].

Each group of seeds was arranged in the chamber in order to complete the sample holder, which was stabilized in temperature($T = 21 \pm 1$ °C) to avoid seed stress. The DL measurements used photon-count mode in 100 µs time-windows for 20 thousand points (total = 2 s) and were taken after twenty-second exposure to white light (160 lux), and repeated sequentially ten times for each sample. A delay of 370 ms occurs between the end of excitation and photon-count start due technical limitation.

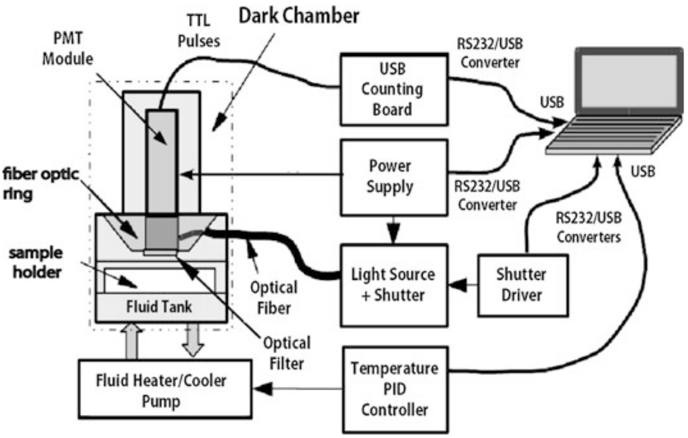

Fig. 9.1 Setup for DL measurements in biosamples—(*top*) chamber, illumination and controls schematics; (*bottom*) picture of prototype

The 10-repetition DL data was averaged and the curve was fitted by generic hyperbolic-like decay, formulated by:

$$a + b/(1 + c.t)^d \tag{9.1}$$

where t is related to time, $a + b$ is the curve's initial value (t = 0), a is its final value ($t = \infty$), c is related to the decay velocity for small t and d is related to enhancement in velocity decay, more pronounced for great values of t.

After all samples had been measured two hundred seeds were taken from each lot and induced to germinate in a controlled chamber (T = 30 ± 1 °C, humidity >70 %) for 30 days. For that, each group of 200 were divided in 4 × 50 seeds, and each sub-group disposed in rolls of paper towels moistened with water equivalent to 2 and 1/2 times the dry paper substrate weight. At the 15th day after start and at the end, at the 30th day, seeds of 'A' series was analyzed in terms of hypocotyl-radicle axis growth, measuring each seedling elongation; effective germination rate was determined for 'A' and 'B' series.

9.3 Results and Discussion

The DL time profiles of all groups of the first series of tests (Table 9.1) are shown at Fig. 9.2, as well as their correspondent hyperbolic decay fitting ($R^2 > 0.995$) parameters: a, b, c and d. It is clear from Fig. 9.2 that groups A7, A11 and A13 present higher initial value than the other groups. Group A17 time profile is also distinguishable from the remaining curves, with small increase from 1 to 100 ms.

Fig. 9.2 DL data for groups A7 to A18 (*left*)—10 test average time profile; (*right*) parameters of hyperbolic decay fitting ($R^2 > 0.995$)

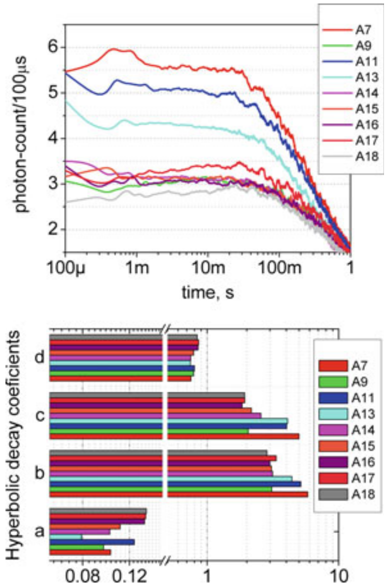

These facts are so reflected in the *b* parameter of their DL. It is also noted that the *c* parameter is also higher for the A7, A11 and A13 samples, meaning that their DL intensity decay faster that the other groups, as can be seen also in the time profiles form 10 to 100 ms. The A15 time profile is also noticed to have small increase at the beginning, i.e. t < 1 ms, as occurring for the curves of A7, A11 and A13.

The remaining groups—A9, A14, A16 and A18—have similar time profiles, with small initial value (~ 3) and regular decay velocity, i.e. similar *c* factor. The germination data—seedling's elongation incidence, in a total of 200 seeds/group—at the 15th and 30th day are presented at Fig. 9.3 for the viable groups; the ones not displayed had no seedling development at all, i.e. zero seeds alive. It is noted that groups A7 and A13 present the higher development of all, followed by A11 and, with much lower development, by A15 and, much lower, A17. The A9 had few seedlings developed.

By summing all seedlings' length the total elongation is obtained for each group, for both the 15th and 30th day after imbibition. This numbers were so plotted against the correspondent *b* and *c* parameters, and these datagrams are shown at Fig. 9.4. Good linear correlation was found between the hyperbolic fitting parameters and the total seedling elongation for both the 15th and 30th day data, with $R^2 > 0.85$ in all cases.

The data obtained for the second, B series of aged seeds (Table 9.2) were analyzed in similar manner as done for the A series, but using just the total germination rate at the 30th day, instead of the hypocotyl-radicle axis growth used before. In this case with most of lots with very good germination, the DL curves

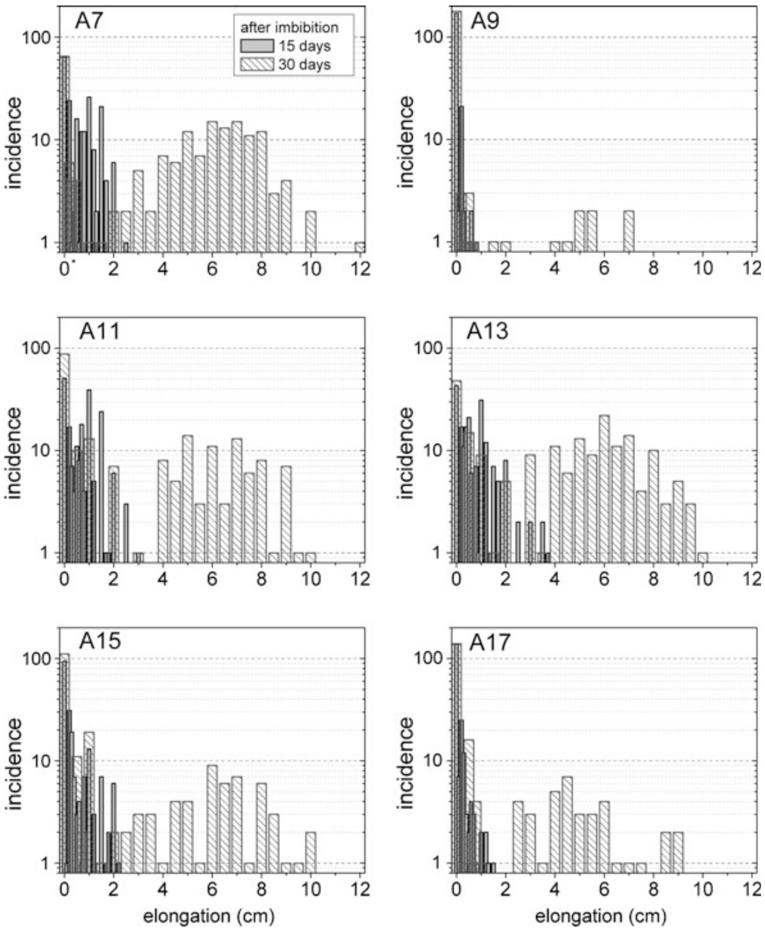

Fig. 9.3 Seedling's length for series A (Table 9.1) for viable groups at the 15th and 30th days after imbibition—each group has 200 seeds total

were not so different for longer *t*, making harder the hyperbolic decay fitting to converge. So, the parameter *d* was fixed [$d = 1$, (9.1)] to promote a lower standard deviation for the *c* parameter. The germination rate at the 30th day related to the *b* and *c* factors are plotted at Fig. 9.5.

Even after aging, lots of B series presented high germination rate (>75 %), and very similar DL curves—only exception is sample #1, with 40 % germination rate. With so, parameters *b* and *c* presented much smaller variation than that obtained for the A series. Even though the datagrams of Fig. 9.5 could be fitted by a linear relation ($R^2 > 0.75$).

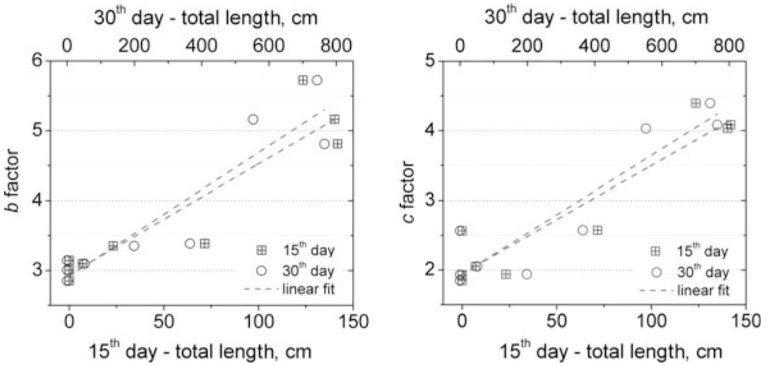

Fig. 9.4 Seedling's total length at the 15th and 30th day versus the hyperbolic decay fitting parameters—(*left*) the *b* factor and (*right*) the *c* factor; *dashed line* correspond to linear regression ($R^2 > 0.85$)

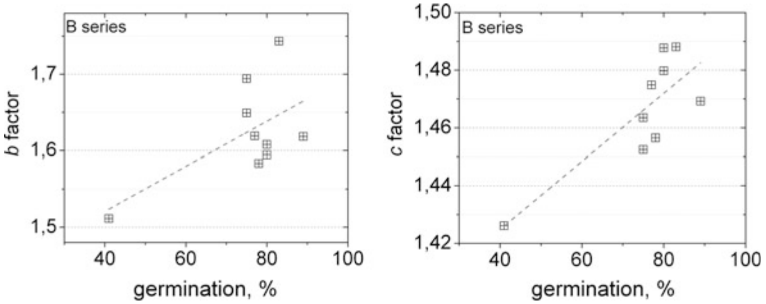

Fig. 9.5 Germination rate at the 30th day versus the hyperbolic decay fitting parameters—(*left*) the *b* factor and (*right*) the *c* factor ($d = 1$); *dashed line* correspond to linear regression ($R^2 > 0.75$)

9.4 Conclusions

The ultra-weak delayed luminescence time profiles of two series of nine groups of coffee seeds with different germination capacity were studied in terms of hyperbolic decay parameters, and good correlations were found between the DL initial value and the decay velocity versus the germinating vigour—i.e., total seedling elongation at the 15th and 30th day after imbibition.

The first, preliminary series 'A' used old samples (2011), already with vigour depreciated by the long storage time in natural conditions, and so just few groups presented significant germination while four of them were almost dead.

The second series 'B', using very fresh samples (2013) with high germination capability even after aging treatment, was less diverse in terms of DL parameters than series 'A', even though a linear relation was found when considering constant the exponential factor (d = 1).

Although limited in number and range of seed quality, the preliminary data here presented show that the DL measurements of coffee seeds may be used as a fast, non-invasive, non-destructive test to verify sample's viability, and so help in improving post-harvest treatment, storing methods and maybe also beverage quality.

Until now, our preliminary results indicate that DL presents good correlation for low quality seeds. Coffee beans have both embryo and endosperm alive, but the largest proportion is defined by endosperm. As the germination is related to the embryo development more studies are needed improve the knowledge about the seed quality behavior in relation to DL measurements. Next series of experiments would replicate this type of analysis but using a single lot of fresh seed samples (<1 year), which may present high physiological quality, and from which sub-lots would be separated and artificially stressed (aged) in effective manner, in order to have samples with intermediate vigour. With all samples taken from the same lot and underwent different aging treats it is expected to have better view of the relation between germination, vigour and the DL parameters.

Acknowledgements Authors are grateful to the Brazilian Coffee Research Consortium (Embrapa Coffee/UFLA/IAC) for providing the seed samples, to CNPq (*Conselho Nacional de Pesquisa*), to FAPESP (*Fundação de Amparo à Pesquisa do Estado de São Paulo*, #04/10146-3) for partial laboratory support, and to the technical staff supporting LaFA/FT.

References

1. M.T. Eira, E.A. Silva, R.D. De Castro, S. Dussert, C. Walters, J.D. Bewley, H.W. Hilhorst, Coffee seed physiology. Braz. J. Plant Physiol. **18**(1), 149–163 (2006)
2. E. Couturon, Maintaining the viability of coffee seeds by checking their water-content and storage-temperature. Cafe Cacao **24**(1), 227–232 (1980)
3. T.D. Hong, R.H. Ellis, Optimum air-dry seed storage environments for arabica coffee. Seed Sci. Technol. **20**(3), 547–560 (1992)
4. S. Dussert et al., Beneffícial effect of post-having osmoconditioning on the recovery of cryopreserved coffee (*Coffea* spp.) seeds. Cryo-Lett. **21**(1), 47–52 (2000)
5. S. Dussert, N. Chabrillange, G. Rocquelin, F. Engelmann, M. Lopez, S. Hamon, Tolerance of coffee (*Coffea* spp.) seeds to ultra-low temperature exposure in relation to calorimetric properties of tissue water, lipid composition, and cooling procedure. Physiol. Plant **112**(4), 495–504 (2001)
6. M. Kobayashi, H. Inaba, Photon statistics and correlation analysis of ultraweak light originating from living organisms for extraction of biological information. Appl. Opt. **32**(1), 183–192 (2000)
7. Michal Cifra, Pavel Pospíšil, Ultra-weak photon emission from biological samples: Definition, mechanisms, properties, detection and applications. J. Photochem. Photobiol. B Biol. (2014). doi:10.1016/j.jphotobiol.2014.02.009
8. Y. Yan, F.A. Popp, G.M. Rothe, Correlation between germination capacity and biophoton emission of barley seeds (*Hordeum vulgare L.*). Seed Sci. Technol. **31**(2), 249–258 (2003)

9. L. Lanzanò, L. Sui, E. Costanzo, M. Gulino, A. Scordino, S. Tudisco, F. Musumeci, Time-resolved spectral measurements of delayed luminescence from a single soybean seed: effects of thermal damage and correlation with germination performance. Luminescence **24**(6), 409–415 (2009)
10. Y. Yong, W. Jun, Ultra-weak bioluminescent and vigour of irradiated rice. Int. J. Agric. Biol. Eng. **3**(1), 85–90 (2010)
11. J. Wang, Y. Yu, Relationship between ultra-weak bioluminescence and vigour or irradiation dose of irradiated wheat. Luminescence **24**(4), 209–212 (2009)
12. C.M. Gallep, E. Conforti, M.T. Braghini, M.P. Maluf, Y. Yan, F.A. Popp, Ultra-weak delayed luminescence in coffee seeds (*Coffea arabica* and *C. canephora*) and their germination potential: some indications for a photonic approach in seed viability, in *Proceeding of 11th Brazilian Symposium of Microwave and Optoeletronics* (2004)
13. E. Bertogna, S.R. dos Santos, J.E.S. Paterniani, E. Conforti, C.M. Gallep, Compact, automatic set-up for ultra-weak photon emission measurements in organisms. SBMO/IEEE MTTS International Microwave and Optoelectronics Conference (IMOC), pp. 449–452. doi:10.1109/IMOC.2011.6169247 (2011)

Chapter 10
Optical Fibre Probe with Lateral Interface

Makoto Tsubokawa

Abstract This paper proposes a novel optical fibre probe containing a scattering layer that is capable of sensing the surrounding light through the lateral surface of the fibre. The performance of the probe in sensing various target objects in free space and water environment has been evaluated by ray-trace simulation. For the probe of diameter 1 mm and length 50 mm, the normalised power, which is defined as the ratio of the signal power to the source power, was obtained within 0.1–0.01 % for the target object over a surrounding space with a radius of $\sim$20 mm. Besides, the probe exhibits sharp directional property with an angular diameter of $\sim$10° in the radial direction. Utilizing this functionality, the probe with the spiral-shaped scattering part will enable the sensing of target objects that are spatially distributed along a fibre axis with a minimum detectable gap of less than 2 mm.

10.1 Introduction

Because of their thin structure and ease of fabrication, there have been many studies on light concentrators with acceptance top/side surfaces of planar waveguides/optical fibres. Most of them are relevant to the well-known luminescent solar concentrator [5, 9, 15]; in contrast, simple concentrator that directly collect illumination light have not been fully explored because of their low efficiency [6, 14]. However, this simple scheme appears to be attractive for optical sensor applications because it may produce versatile applications by expanding the optical interface from a point to the surface. As an interesting example, the integration of optical fibres into textile structures called photonic textiles has been proposed to realize multifunctional sensors such as wearable photodetectors (PDs) or direction sensors of light beams [1, 3, 11]. We are currently studying this technique to enable

---

M. Tsubokawa (✉)
Waseda University, Kitakyusyu, Japan
e-mail: tsubokawa.m@waseda.jp

P.A. Ribeiro and M. Raposo (eds.), *Photoptics 2014*,
Springer Proceedings in Physics 177, DOI 10.1007/978-3-319-27321-1_10

their application as thin optical probes used to sense the surroundings. In general, such optical probes need to incorporate micro-lens systems or several optical fibres, and should sweep over the target space because a point detector only gets a point image [2, 4, 8, 10, 12, 16]. If the detection through the side-surface interface is applicable, it may not only simplify the sweep mechanism but also enable us to realize passive optical probes without the need for precise lens systems.

In this study, we show a new design of thin fibre-optic probe with a side surface interface, and evaluate basic characteristics by performing ray-trace simulations [7]. Both light source (LS) for illuminating target objects and a PD are attached to the end of an optical fibre, and the light propagation through a side surface is adjusted by a Mie scattering layer embedded in the optical fibre. We show the output signal of the probe as a function of the size, position and materials comprising the target object, and finally evaluate the spatial distribution of the target and its resolution.

10.2 Fibre-Optic Probe Model

Figure 10.1 shows the probe model consisting of two serially concatenated guides and sensor parts. The parameters used in our simulation for the waveguide and light source are listed in Table 10.1. The guide part has a two-layered structure with an outer coating as an absorber in which the core guiding input light from a light source is embedded in the bottom of the cladding in addition to a normal core. A light source and PD are attached to the end face of each core. The sensor part has the scattering part at the bottom in the cladding, which is connected to the bottom core in the guide part. Light scattering is observed in the scattering part (width D) composed of a cluster of air particles with a particle number density ρ. The width D is defined as the arc length corresponding to the width of the focus zone for normal incident light and is calculated using the size and refractive indices of the optical fibre. The minimal arrangement of the scattering part effectively generates light components in the direction of the target and suppresses excess loss during propagation along the fibre. Because of reducing D, the high index fibre is used in the simulation. Input lights are scattered in the sensor part and a portion of them reaches the target object owing to the lens effect in cylindrical optical fibre. Lights reflected at the target partially re-enter the optical fibre, and are either scattered again and transmitted to the PD or are escaped to the outside. As shown in Fig. 10.1, we assume the square target object of $w_1 \times 2w_2 \times \delta w$ at distances d_1 and d_2 above the sensor part. Angles ψ is the angular diameter of the target. For simplicity, we assume the bottom surface of the target plane is a 96 % reflector as a reference. Here we define the normalised received power η_{probe} as the ratio of light power that reaches the PD's surface by way of the target plane to the light power of the source. In our model, η_{probe} estimated by the ray-trace simulation gives results that are equivalent to the case using incoherent light without interference effects. Under the Mie scattering model used in this simulation, the wavelength dependence

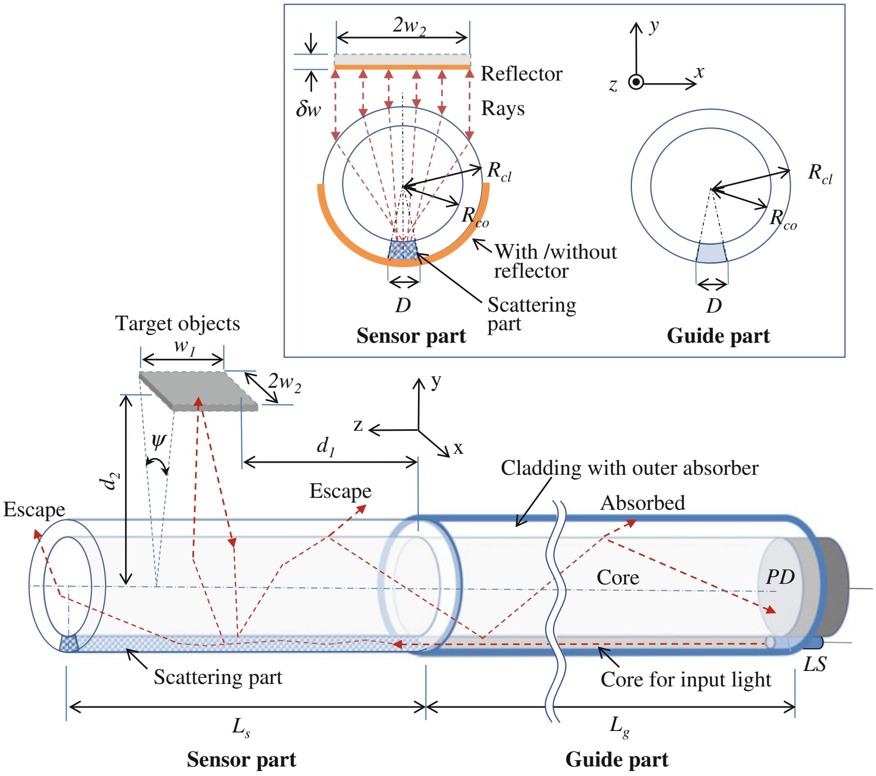

Fig. 10.1 Fibre-optic probe model

Table 10.1 Parameters of fibre-optic probe

Optical fibre	Sensor part	Guide part
Core radius R_{co}	0.5 mm	0.5 mm
Cladding radius R_{cl}	0.55 mm	0.55 mm
Refractive index of core	1.83	1.83
Refractive index of core for input light	1.86	1.86
Refractive index of cladding	1.86	1.46
Particle radius r (material)	250 nm (air)	None
Particle number density ρ	2.3×10^8 mm^{-3}	None
Width of scattering part D (Central angle)	0.07 mm (7.5°), 0.3 mm (31°)	
Length L_s, L_g	50 mm	50 mm
Light source and photodetector		
Wavelength	550 nm	
Polarisation	Random	
Source position	Embedded in end of core for input light	
Photodetector	Area detector attached on core end face	

Refractive indices of 1.86 (LaSFN9), 1.83 (LaSFN40), 1.46 (SiO_2) are assumed [13] is almost negligible over a broadband spectrum such as natural light; therefore, we use a monochromatic source of 550 nm wavelength with a random polarisation instead of a broadband light source.

10.3 Simulation Results

10.3.1 *Normalised Received Power* η_{probe}

Figure 10.2 shows η_{probe}, which is dependent on the distance d_2 and width w_2. Here $d_1 = 0$ and $w_1 = L_s = 50$ mm. The particle number density ρ is assumed to be 2.3×10^8 mm^{-3} because η_{probe} has a maximum for this model in our simulation. Larger ρ causes not only larger scattering efficiency but also excess loss in light propagation along a fibre. Under this condition, 22 and 36 % of the source power arrive at the target plane through the sensor part with and without the 96 % reflector, respectively. Although these are due to scattering and lens effect in a fibre, it is fairly high efficiency without imaging optics. We can see in Fig. 10.2 that η_{probe} does not vary much for $d_2 \leq 2$ mm, but above 2 mm, it tends to decrease. If the incident angle distribution to the target object is uniform, the number of round-trip rays between the sensor part and the target is roughly proportional to a half of the angular diameter $\psi(d_2)/2$, and then $\eta_{probe} \propto \psi(d_2)/2 = 2\tan^{-1}[w_2/2d_2]$. In fact,

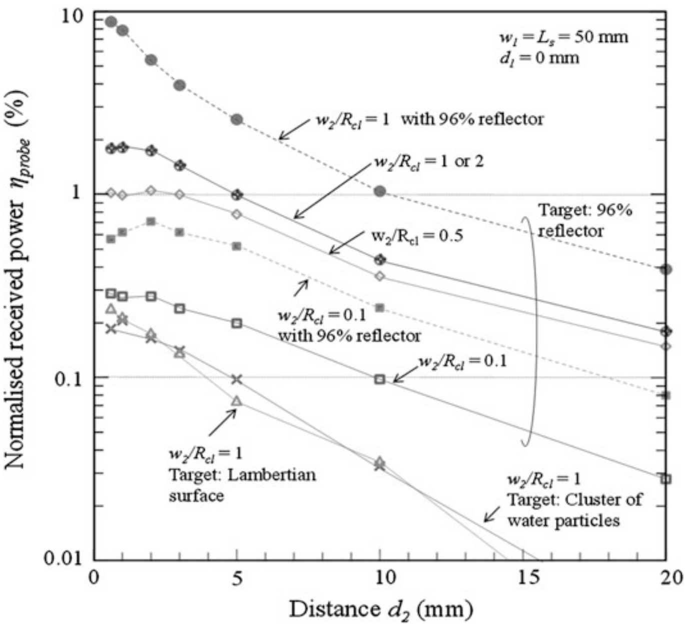

Fig. 10.2 Normalised received power η_{probe} as a function of distance d_2 and width w_2/R_{cl}

the downward curves in Fig. 10.2 indicate the presence of a slightly small slope compared to the variation of $\psi(d_2)/2$ because light components with nearly normal incidence dominate owing to the lens effect in optical fibre. On the other hand, η_{probe} decreases at a rate smaller than w_2/R_{cl} because light components other than normal incidence can re-enter the sensor part when $w_2/R_{cl} < 1$. Regarding the received power, for example, η_{probe} is approximately 0.3 and 1.8 % for $w_2/R_{cl} = 0.1$ and 1, respectively, at d_2 = 2 mm, when the sensor part has no reflector. These values are much smaller than the rate of light power that reaches the target plane as mentioned above, which suggests that the optical loss after reflection at the target plane is significant in our model. Actually, 3–4 dB loss is observed only at the boundary between the sensor and guide parts, which remains an issue. When the 96 % reflector is attached to the sensor part, η_{probe} was more than doubled, i.e. 0.7 and 5 % for $w_2/R_{cl} = 0.1$ and 1, respectively, at d_2 = 2 mm. In Fig. 10.2, we also plot curves for different type of targets—the Lambertian reflector and cluster of water particles as a Mie scattering object (δw = 0.5 mm, r = 250-nm). They indicate that η_{probe} is smaller and more steeply decrease as compared to the case of a simple target with a reflector. These are seen as the results from the spread of the reflection angle and lower reflectivity at the target object.

Next, the dependence of η_{probe} on the target length w_1 and position d_1 along a fibre axis is shown in Fig. 10.3. Another scale of the power ratio of $(\eta_{probe}-\eta_{bias})/\eta_{probe}$ has also been plotted, where η_{bias} is defined as the ratio of light power that reaches the PD's surface in the absence of the target object to the light power of the source. We can see that η_{probe} is nearly proportional to w_1 and it exponentially decreases with

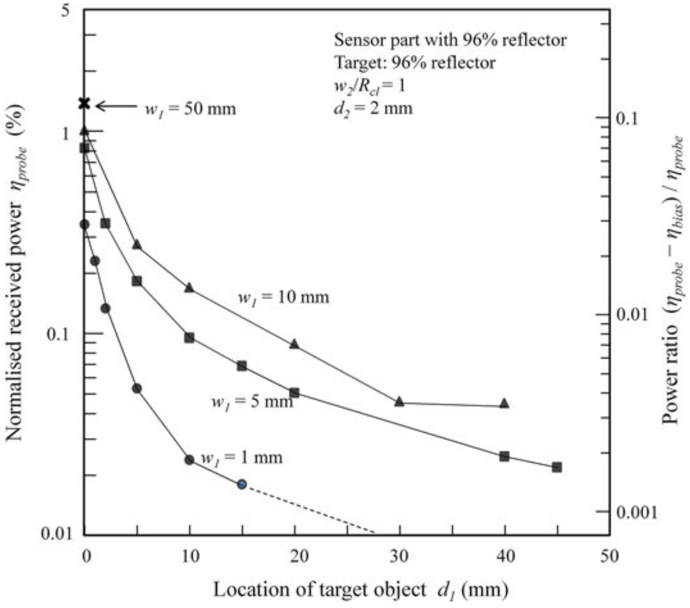

Fig. 10.3 Normalised received power η_{probe} as a function of location d_1 and length w_1

an increase in d_1. This is because the spread of the incidence angle in the y–z plane has a similar influence on targets of different w_1, and an increase in d_1 remarkably reduces the transmission loss along the sensor part. From these results, we can estimate the location when the target size is given, and vice versa. In fact, if we need to simultaneously sense both size and location without a sweep operation, an additional scheme is required. We discuss this issue in the next section. As shown in Fig. 10.3, the power ratio of $(\eta_{probe}–\eta_{bias})/\eta_{probe}$ is relatively small (0.1–0.01). Although it is similar to the signal to noise ratio, the signal component of the η_{probe} can be obtained by determining the separation from η_{bias}, as it is almost constant regardless of the target. Enhancing $(\eta_{probe}–\eta_{bias})/\eta_{probe}$ becomes one of the important issues in suppressing the influence of the shot noise during the actual experiments.

10.3.2 Evaluation Under Water Environment

Next, we consider a case involving the use of our model in water, e.g. probe biological cells in the body. Because the refraction angle becomes small under water conditions, we designed another probe structure with width D calculated to be 0.3 mm according to the definition. Figure 10.4a, b show the η_{probe} as a function of distance d_2 under the water condition. Here target objects of 1.1 × 50 mm are (a) 96 % reflector and (b) examples of Mie models and biological objects with $\delta w = 1$ mm.

We see in Fig. 10.4a that η_{probe} is obviously improved at $D = 0.3$ mm compared to $D = 0.07$ mm in the short d_2 region for the case with/without reflector on the sensor part. For a distance of $d_2 > 5$ mm, the advantage decreases when using the sensor part without the reflector. This is because the number of round-trip rays between the fibre and the target is enhanced by the scattering part with an optimum D (= 0.3 mm). However, the propagation loss owing to the excess scattering along a fibre also tends to increase with increase in d_1. This loss effect is mitigated by positioning a reflector on the sensor part. In Fig. 10.4b, we see that the skin dermis shows a higher reflectivity compared to the epidermis and Mie model of air particles (LightTools, Synopsys, Inc.). These results mainly indicate the differences of the reflectivity of the objects, which are useful when discerning target objects.

10.3.3 Evaluation of Spatially Distributed Targets

When an optical needle probe with a point detector is applied to sense a 3D space, it usually needs to be swept over the target plane; moreover, the time/frequency domain immersion or optical coherence tomography (OCT) techniques are usually applied to resolve the depth information. Here we focus on the approach that is used to simplify the sweep operation and set aside the techniques of immersion or OCT. Because our method can extract the information of an object arranged linearly along

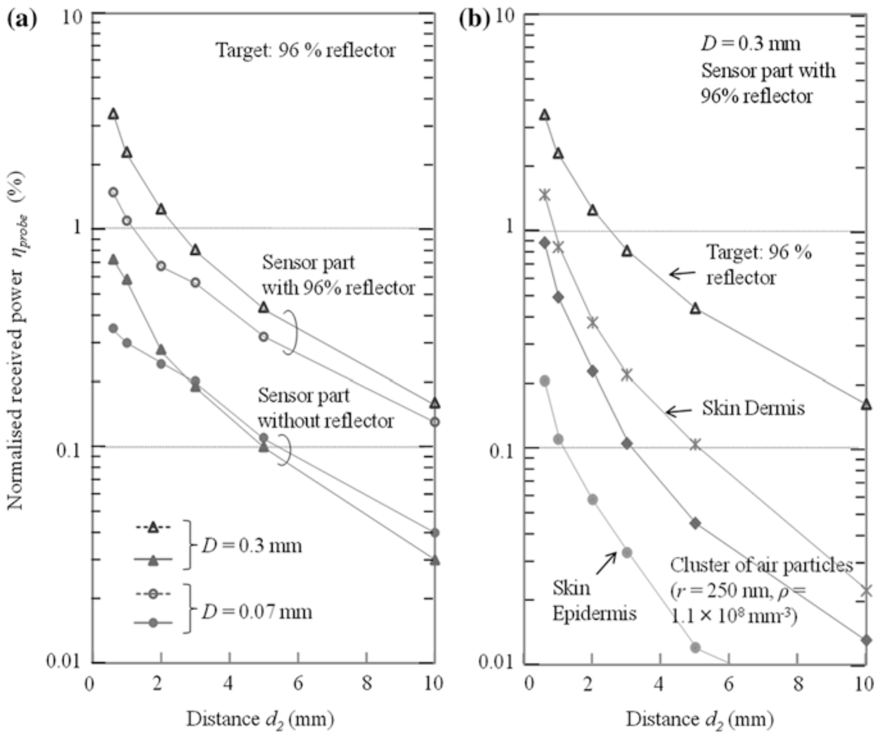

Fig. 10.4 Normalised received power η_{probe} as a function of d_2 under water conditions. The thickness δw of skin dermis, epidermis and cluster of air particles are 1 mm

the probe, the linear distribution of an object may be detected without a complex sweep operation. Figure 10.5 shows the sensor part, which has a spiral-shaped scattering part embedded in cladding. This is the same structure as the 360° twisted sensor part in Fig. 10.1.

Initially, we analysed the directional property of the simple fibre-optic probe with straight scattering part, shown in Fig. 10.1. Figure 10.6 shows the radar chart of η_{probe} plotted as a function of θ_{fibre}, the angle at which the probe is rotated with respect to the reflector. The measurements were performed assuming 96 % mirror target of 50 × 1.1 mm, d_2 = 2 mm and D = 0.07 mm. As can be easily predicted from the geometric structure of the sensor part, η_{probe} indicates the distinct directional property of the target in the direction opposite to the scattering part (180°). The full width at half maximum of the peak is $\sim$10°. This result implies that the probe is capable of observing the surrounding light distribution as a function of the incident angle in the x–y plane.

Next, supposing the twisted sensor part, the sensor is capable of sensing the target plane that is continuously twisted at an angle θ_{TP}, as shown in Fig. 10.5. This could be ascribed to the sharp directional property of the sensor, as mentioned above. Here, θ_{TP} = $360 d_1/L_s$°. From a different viewpoint, we can detect the

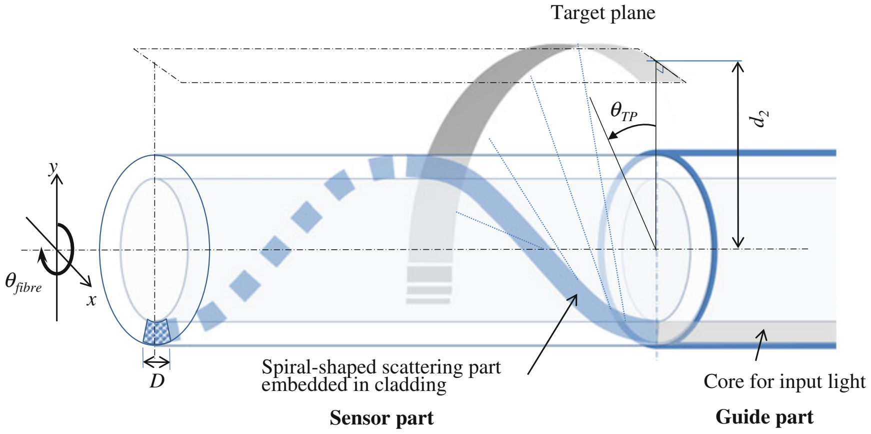

Fig. 10.5 Fibre-optic probe with spiral-shaped scattering part

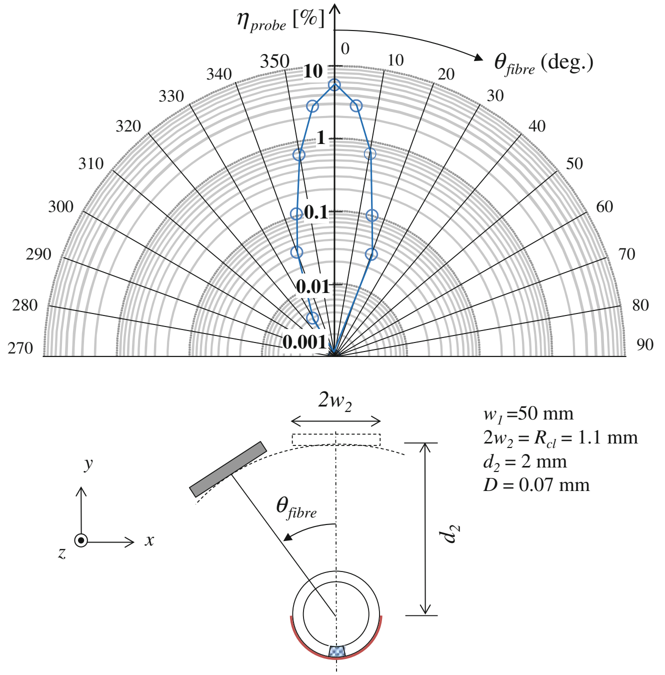

Fig. 10.6 Radar chart of normalised received power η_{probe} in straight sensor part

distribution of the target plane positioned above the sensor part (parallelogram of dash-dotted line) when the optical fibre is rotated by $0° \leq \theta_{fibre} < 360°$, where $\theta_{fibre} = -\theta_{TP}$. Figure 10.7 shows the normalised received power η_{probe} as a function of θ_{fibre}. The reflector is similarly twised with the scattering part on the sensor

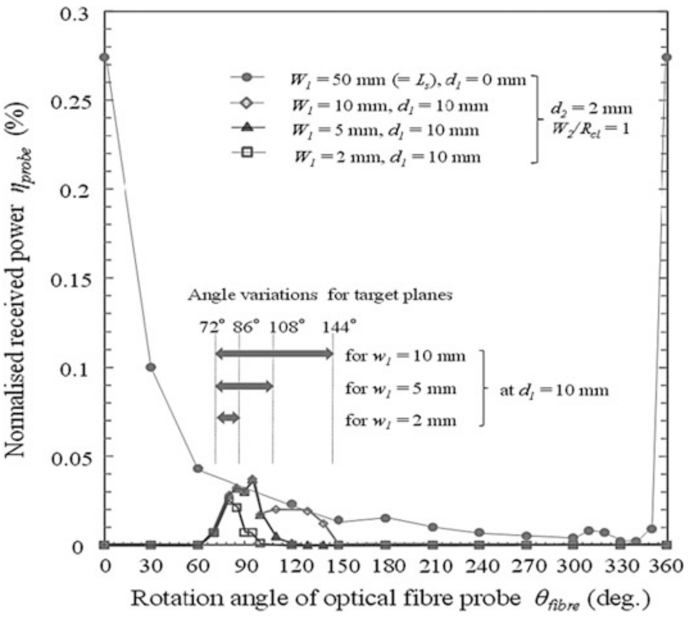

Fig. 10.7 Normalised received power η_{probe} in the twisted sensor part as a function of the angle of rotation θ_{fibre}

part. The curve with filled circles indicates η_{probe} for the target of $w_1 = 50$ mm, $w_2/R_{cl} = 1$, $d_1 = 0$ mm and $d_2 = 2$ mm, which corresponds to the maximum η_{probe} at θ_{fibre}. The curve shows a steep decline with an increase in θ_{fibre} because of the constant value of ρ along the fibre axis. This tendency is similar to the results for $1 < w_1 < 5$ mm, shown in Fig. 10.3. The peak width of ~26° at $\theta_{fibre} = 0°$ is broader than that shown in Fig. 10.6, as the centre of the lightning area on the target exhibits a certain angular spreading along the z-axis due to the spiral form of the scattering part. Three curves obtained for targets of $w_1 = 2$, 5 or 10 mm at $d_1 = 10$ mm are also shown in Fig. 10.7, and the angles of peak locations and widths of three peaks are roughly estimated to be 80°, 90° and 110° and 15°, 28° and 60°, respectively. On the other hand, the four angles of edge locations in the target are calculated to be 72°, 86°, 108° and 144°, as shown in Fig. 10.7. As is seen, the peak locations are in good agreement with each other, and that the peak width well reflects the target length w_1. As the three curves are segments of the maximum curve (filled circle symbols), the peak position and width corresponding to larger w_1 tend to be fuzzy. Nevertheless, they are relatively precise for $w_1 \leq 5$ mm.

Finally, we evaluate two targets arranged in tandem with a small gap δd to check the spatial resolution. From Fig. 10.7, the angle resolution of ~15° is predicted for two targets of length 2 mm. Figure 10.8 shows η_{probe} for two targets with $\delta d = 2$ and 1 mm, respectively. Here, $w_1 = 2$ mm and $w_2/R_{cl} = 1$. Two peaks in the curve for $\delta d = 2$ mm are clearly observed, and the peak interval is estimated to be 4.2 mm for

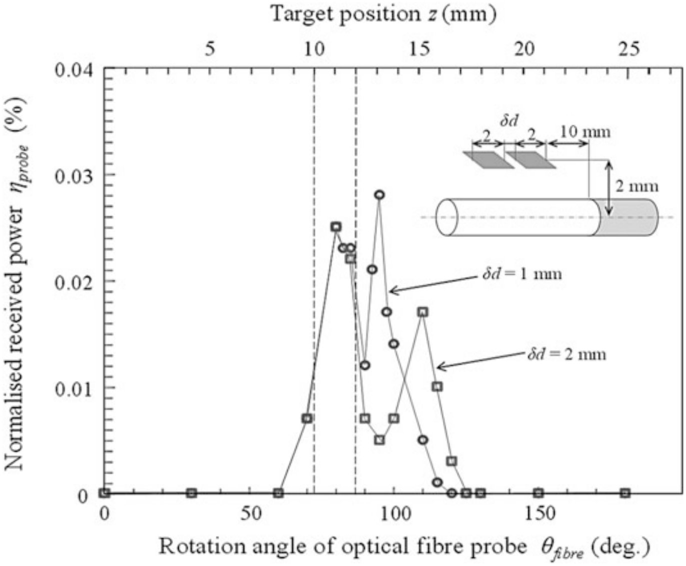

Fig. 10.8 Curves of normalised received power η_{probe} for the targets with a small gap. Two target planes where $w_1 = 2$ mm, $w_2/R_{cl} = 1$, $d_1 = 10$ mm and $d_2 = 2$ mm are arranged in tandem with a gap δd of 1 and 2 mm

an angle difference of 30°. Because the peak location indicates the centre of the target, the peak interval is approximately given by $\delta d + w_1$ and δd is almost the same as real gap of 2 mm. For the case of $\delta d = 1$ mm, we also find two peaks with an interval of 15°, corresponding to 2.1 mm, which is slightly smaller than the expected value of 3 mm (= $\delta d + w_1$), and is caused by the peak shift effect due to the overlapping of different height pulses. Consequently, under this condition, the spatial resolution for the gap is estimated to be slightly less than 2 mm.

10.4 Conclusions

We proposed a simple fibre-optic probe with a side-surface interface against a target space, and evaluated the basic performance by performing ray-trace simulations. Our model has a needle shape of approximately 1-mm diameter and 50-mm length, which enables us to detect the normalised light power of 0.01–10 % of the source power when target objects are located in a surrounding cylinder space with an ~20-mm radius. Under water conditions, the sensitivity was easily improved by adjusting the size of the scattering part. Moreover, by using the directional property of the probe twisted by 360°, the targets distributed along the fibre axis with a minimum detectable gap of less than 2 mm could be measured.

In our future work, we firstly aim to improve the signal level by optimizing the probe structure and materials, for example, the shape of the fibre and particle number density distribution of the scattering parts may bring about desirable effects such as narrow focus area and smooth sensitivity along a fibre. As next step aim, we need to incorporate a key technique such as the OCT technique for our method to resolve radially distributed targets.

Acknowledgements Part of the research presented in this paper has been done under JSPS KAKENHI Grant Number 25420346.

References

1. A.F. Abouraddy, Towards multifunctional fibres that see, hear, sense and communicate. Nat. Mater. **6**, 336–347 (2007)
2. R.R. Ansari, Microemulsion characterization by the use of a noninvasive backscatter fibre optic probe. Appl. Opt. **32**, 3822–3827 (1993)
3. G. Cho (ed.), in *Smart clothing technology and applications*. (CRC Press, 2010), pp. 115–134
4. J.S. Dam, Fibre-optic probe for noninvasive real-time determination of tissue optical properties at multiple wavelengths. Appl. Opt. **40**, 1155–1164 (2001)
5. O. Edelenbosch, Luminescent solar concentrators with fibre geometry', OSA Opt. Express **21**, 503–513 (2013)
6. J.M. Kim, Optical efficiency-concentration ratio trade-off for a flat panel photovoltaic system with diffuser type concentrator. Sol. Energy Mater. Sol. Cells **103**, 35–40 (2012)
7. LightTools, Synopsys Inc. http://www.opticalres.com. Accessed 20 May 2013
8. D. Lorenser, Ultrathin side-viewing needle probe for optical coherence tomography. Opt. Lett. **36**, 3894–3896 (2011)
9. K.R. Mcintosh, Theoretical comparison of cylindrical and square-planar luminescent solar concentrators. Appl. Phys. B **88**, 285–290 (2007)
10. D. Piao, Endoscopic, rapid near-infrared optical tomography. Opt. Lett. **31**, 2876–2878 (2006)
11. M. Rothmaier, Photonic textiles for pulse oximetry. Opt. Express **16**, 12973–12986 (2008)
12. D.D. Sampson, Microscope-in-a-needle technology for deep-tissue 3D imaging, in *Proceedings of the International Conference on Information Photonics*, pp. 1–2
13. Schott Glass Inc. http://www.schott.com/advanced_optics/us/abbe_datasheets/schott_datasheet_all_us.pdf. Accessed 20 Dec 2014
14. M. Tsubokawa, A novel Fibre-optic concentrator with scattering pars. IEICE Trans. Electron. E97-C:93–100 (2014)
15. W.G.J.H.M. Van Sark, Luminescent solar concentrators—a review of recent results. Opt. Express **16**, 21773–21792 (2008)
16. Q. Wang, Measurement of internal tissue optical properties at ultraviolet and visible wavelengths: Development and implementation of a fibreoptic-based system. Opt. Express **16**, 8685–8703 (2008)

Part III
Lasers

Chapter 11
Compressor Design for a 30 fs-300 J 10 PW Ti:Sapphire Laser: Divided-Compressor with an Object-Image-Grating Self-tiling Tiled Grating

Zhaoyang Li, Tao Wang, Guang Xu and Yaping Dai

Abstract A 30 fs-300 J Ti:sapphire laser requires a optimized compressor to compress the 2.7 ns/30 nm deep chirped long pulse to 30 fs. We proposed a compressor design, which reduces the grating number, grating size, vacuum compression chamber cubage and system complexity, by using a divided-compressor structure and an object-image-grating self-tiling method.

11.1 Introduction

Femtosecond 10 PW (petawatt) lasers are being planned and constructed recently worldwide. For example in China a 30 fs-300 J 10 PW laser based on Ti:sapphire is right now under plan in China. This system will use the well-known chirped-pulse amplification (CPA) technique to support its output capability [1].

The primary design of the system linear chirped ratio is around 2.7 ns/30 nm. Therefore, the pulse compression process will be challenged by several problems, including large-size gratings, long compression distance, and huge vacuum compression chamber [2]. In this paper, we attempt to give a basic compressor design to solve the above problems.

Z. Li (✉) · T. Wang · Y. Dai
Shanghai Institute of Laser Plasma, Jiading, Shanghai, China
e-mail: zzyylee@gmail.com

G. Xu
Shanghai Institute of Optics and Fine Mechanics, Jiading, Shanghai, China

P.A. Ribeiro and M. Raposo (eds.), *Photoptics 2014*,
Springer Proceedings in Physics 177, DOI 10.1007/978-3-319-27321-1_11

11.2 Compressor Structure

The primary parameter of the positive chirped pulse after the amplification chain is given by Table 11.1. And the compressor should compress the 400 J, 2.7 ns chirped pulse to less than 30 fs.

In order to reduce the vacuum chamber, as shown in Fig. 11.1, the treacy compressor [3] will be divided into two compressors: a double-pass and a single-pass grating pairs are used as the 1st stage and the 2nd stage compressors, which are located in air and a vacuum chamber, respectively. The compression pulse from the 1st stage compressor is delivered via a fused silica window into the vacuum chamber and is further compressed by the 2nd stage compressor.

The thickness of the fused silica window is designed as 20 mm to balance the air pressure and the nonlinear effect. The compressed duration of the 1st stage compressor is a key parameter, which need to be shorter enough to reduce the 2nd stage compressor, as well as the vacuum chamber, but longer enough to avoid the pulse distortion, fused silica damage, air ionization, and so on. Generally, the requirement

Table 11.1 Beam parameter after the amplification chain

Centre wavelength	800 nm
FWHM	30 nm
Single pulse energy	400 J
Duration	2.7 ns
Beam diameter	Φ150 mm

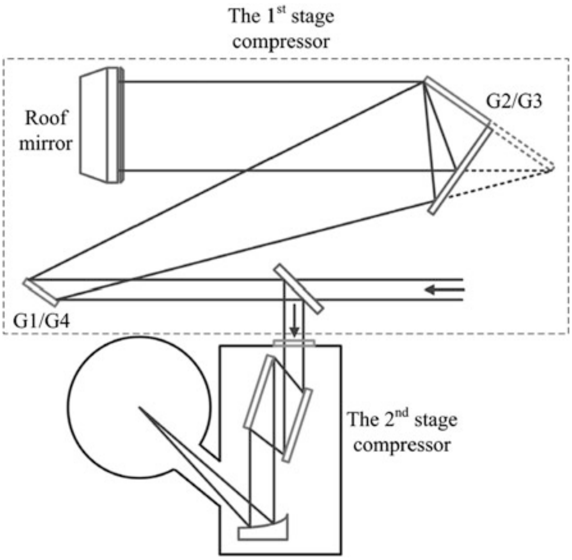

Fig. 11.1 Divided-compressor design

Fig. 11.2 B integral and beam breakup distance versus duration

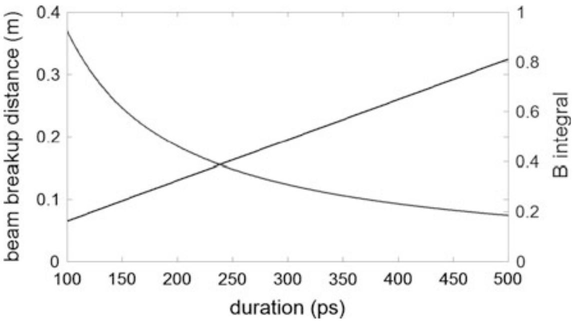

of the pulse temporal and spatial distortion by self-phase modulation (B integral) and self-focusing is high. Therefore, the B integral should be as small as possible, and the beam breakup distance must be much longer than the window thickness. The beam breakup distance can be given by

$$z = \frac{G}{n_2 k I} \tag{11.1}$$

where G is a coefficient from 3 to 10 depended on different conditions. Here we choose 3 to leave the largest margin.

The evolution of B integral and beam breakup distance for pulse duration is given by Fig. 11.2, and the 300 ps is chosen. Accordingly, the B integral is 0.3, and the beam breakup distance is 0.2 m. The intensity is 6 GW/cm^2 which is below the 10 GW/cm^2 threshold of air ionization, and the fluence is 1.84 J/cm^2 that is below the 20 J/cm^2 threshold of fused silica damage for a 300 ps pulse [4].

11.3 Parameter Optimization

11.3.1 The 1st Stage Compressor

Beside of the output parameters of a laser beam from the amplification chain, there are many other parameters determine the geometry of a treacy compressor, such as unclipping spectrum range, part-clipping spectrum range, grating groove density, grating size, slant distance of grating pair, beam incident angle, and so on. The grating groove density and the incident angle are two basic parameters which influence the other ones, and in this section we will calculate parameters of the 1st stage compressor by choosing a suitable grating groove density and an optimized incident angle.

The unclipping spectrum range of our design is set as 90 nm around the centre wavelength to allow the FWHM passing without clipping. As shown in Fig. 11.3, the design of a treacy compressor must satisfy some limitation conditions:

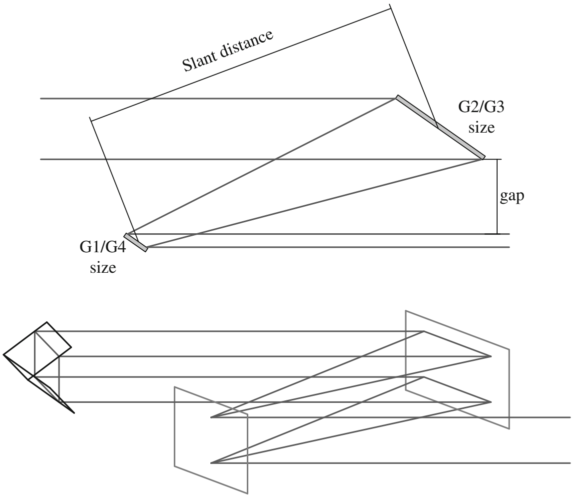

Fig. 11.3 Grating compressor structure

- Grating equation;
- Grating-beam overlap;
- Sufficient wide spectrum window.

This design is based on the broad bandwidth 800 nm dielectric grating due to high damage threshold and wide spectral range [5, 6], therefore types of available groove density include 1200, 1480, 1740 and 1800 g/mm. Figure 11.4 shows the evolution of beam-grating gap, grating size (a tradition single-pass 4-grating compressor with the 1st, 2nd, 3rd, and 4th grating G1, G2, G3, and G4. The sets G1, G4 and G2, G3 have the same sizes, respectively.), and grating pair slant distance for various amounts of incident angle with different grating groove densities. And Fig. 11.5 gives the evolution of cut off wavelength of the part-clipping spectrum range for various values of incident angle with four types of grating groove density.

Our chosen principles of grating groove density and incident angle include: relatively large beam-grating gap, short length of grating and slant distance, and wide range of part-clipping spectrum range. And the optimized parameters are given by Table 11.2.

According to Martz's work, the high diffraction efficiency spectrum window of the broad bandwidth dielectric grating is relative to the incident angle, and the 52° incident angle could meet the requirement of 721–864 nm spectrum window.

To avoid the first grating damage where a short pulse is achieved, a large incident angle is preferred. The fluence with the optimized 52° incident angle is 1.13 J/cm^2 (below the 1.76 J/cm^2 damage threshold for a 120 ps pulse reported by Martz).

Fig. 11.4 Grating size, gap and slant distance for 1200, 1480, 1740 and 1800 g/mm versus incident angle

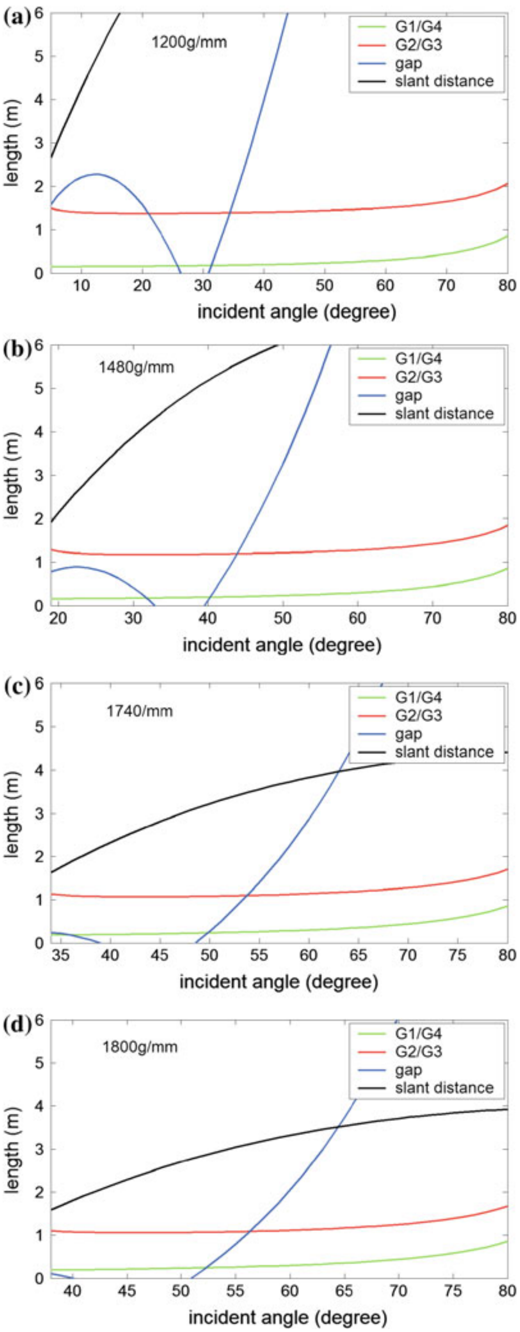

Fig. 11.5 Cut off wavelength of the part-clipping spectrum range for 1200, 1480, 1740 and 1800 g/mm versus incident angle

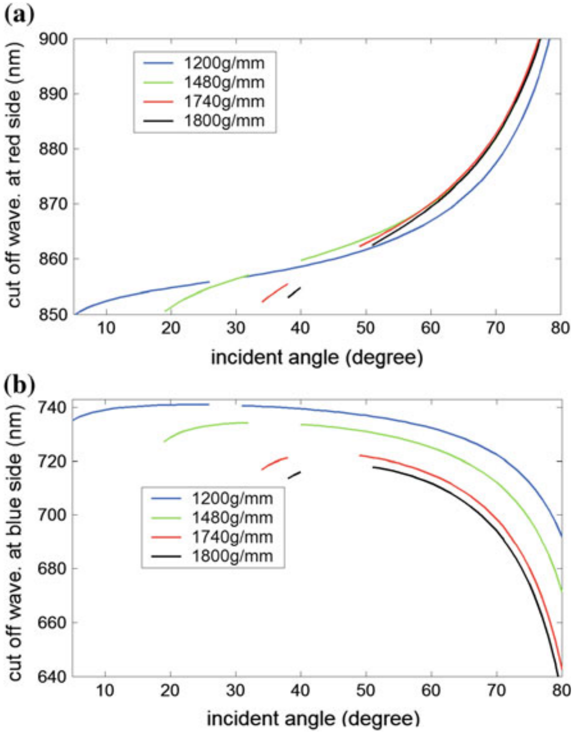

Table 11.2 Optimized 1st stage compressor parameter

Grating density (g/mm)	1740
Incident angle (°)	52
Grating size (m)	1.10
Slant distance (m)	3.37
Wavelength range (nm)	721–864

11.3.2 The 2nd Stage Compressor

The 2nd stage compressor needs to dechirp the rest chirp, and a 30 fs short pulse will be obtained after it. Hence, it is very easy to cause a grating damage. In femtosecond regime, the damage threshold of the broad bandwidth dielectric grating (0.18 J/cm^2 for a 120 fs pulse reported by Martz) is lower than that of the gold coated grating (0.6 J/cm^2). Thus, Horiba Jobin Yvon's gold coated gratings are used in the design of the 2nd stage compressor. The 0.6 J/cm^2 damage threshold determines the smallest incident angle is 71°. A 74° incident angle is chosen to make the fluence 0.5 J/cm^2. Because of the small spatial chirp, a single-pass parallel grating pair is designed as the 2nd stage compressor. And the other parameters are

1740 g/mm grating groove density, 0.336 m slant distance, 0.544 m grating size, 0.37 m grating-beam gap, and 95–1078 nm spectrum range.

11.3.3 Dispersion and B Integral

The non-equivalent incident angles of the 1st and 2nd stage compressors will lead to a big amount of uncompensated 3rd dispersion, and the nonlinearity effect within the fused silica window would introduce the self-phase modulation effect (B integral), hence these two factors will distort the compression pulse temporal profile.

Figure 11.6a shows the compression pulses with a single-stretcher and with a divided-stretcher, respectively. The incident angle and the grating groove density of the single-stretcher are equivalent to those of the 1st stage compressor. The 2nd dispersion of the single-stretcher-divided-compressor system could be compensated, but the 3rd dispersion cannot be eliminated completely. In this way, a divided-stretcher is designed to match the divided-compressor to compensate both the 2nd, 3rd, and 4th order dispersion. The incident angle, the grating groove density, and the chirped ratio of the divided-stretcher and those of the divided-compressor are matched exactly. Moreover, the divided-stretcher has another advantage: the smaller-stretcher can be precisely adjusted to match the 2nd

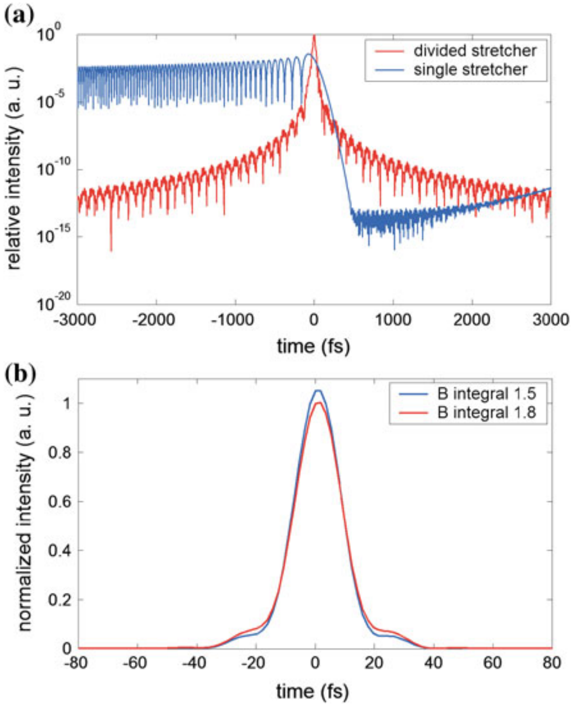

Fig. 11.6 **a** Compression pulse with and without 3rd dispersion compensation. **b** Compression pulse with and without extra 0.3 B integral

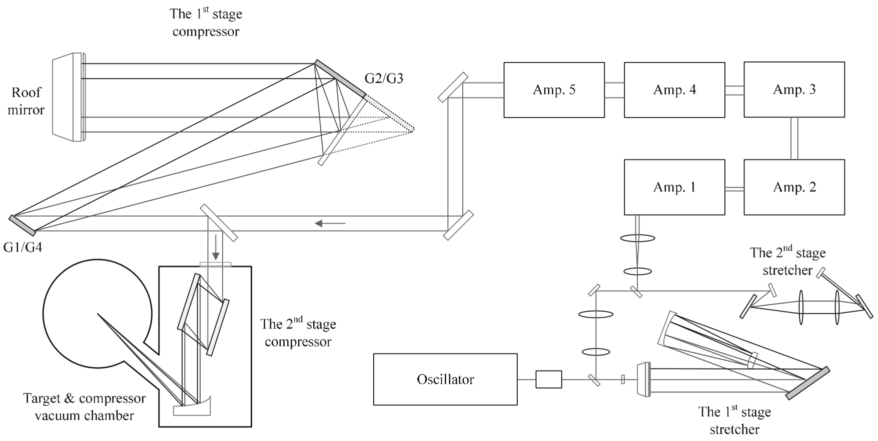

Fig. 11.7 Schematic of the final dispersion system

order dispersion of the whole system without changing the larger-stretcher and the divided-compressor. Therefore, the final dispersion design of system is given by Fig. 11.7.

Besides, we could also adjust the incident angle of the single-stretcher to compensate both the 2nd and the 3rd dispersion orders within the single-stretcher-divided-compressor system.

The control purpose of the B integral within the amplification chain is 1.5. Figure 11.6b shows the compression pulse with a 1.8 B integral added the influence of the fused silica window, and this distortion is acceptable.

11.4 Tiled Grating

The requirement size of the second grating in the 1st stage compressor is 1.1 m. However, the largest size of the available grating is 0.56 m. Therefore, the object-image-grating self-tiling method is used to double the effective grating size to 1.1 m, and the size of the corresponding mirror is 0.8 m [7].

The object-image-grating self-tiling method is a very easy way to enlarge the effective grating size, as shown in Fig. 11.8, which reduce the number of tiling errors within a tiled grating from 6 to only 3. Besides, the tiling condition monitoring of the proposed compressor design, as shown in Fig. 11.1, being very convenient, which can be achieved only by observing the distribution of the main beam focal spot. Unlike the traditional grating tiling, no additional monitoring lasers are needed in a compressor with only one tiled grating. And a similar

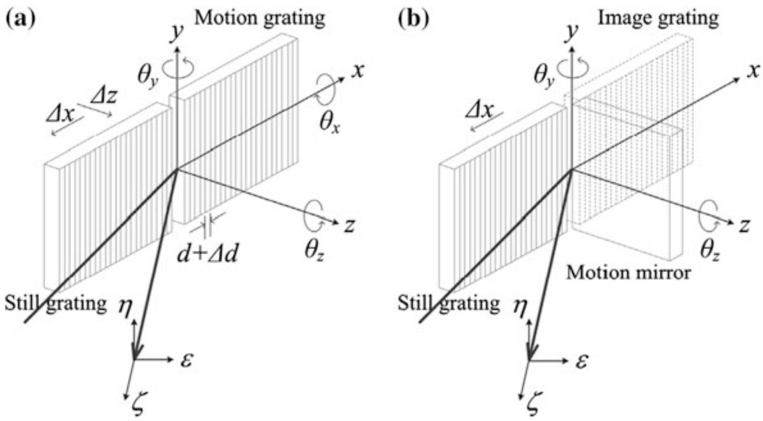

Fig. 11.8 Degrees of freedom within **a** a tradition grating tiling and **b** an object-image-grating self-tiling

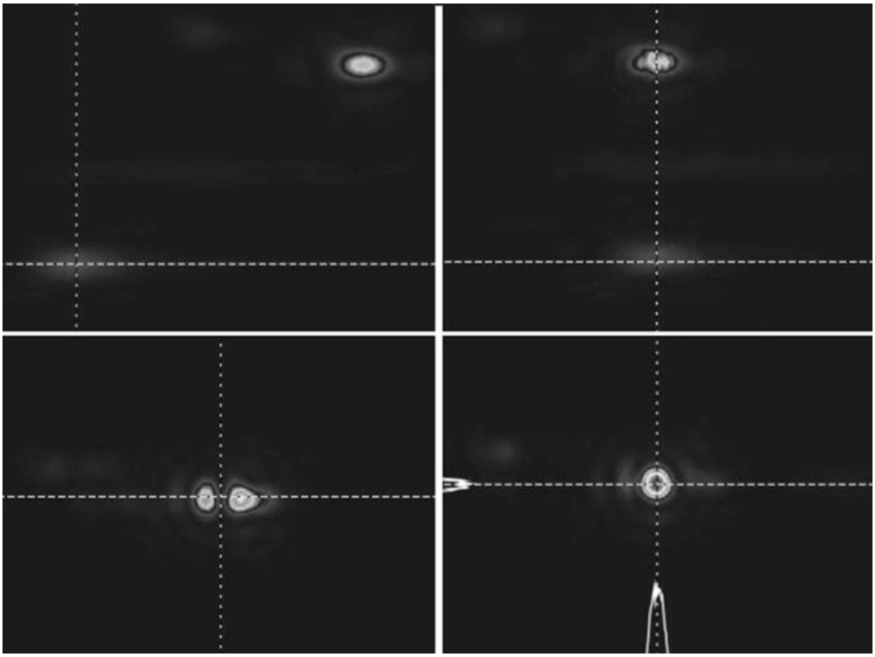

Fig. 11.9 Three steps to achieve the ideal tiling condition

demonstration experiment is shown in Fig. 11.9, we just need 3 steps to achieve an ideal object-image-grating self-tiling tiled grating by adjusting θy, θz, and Δx (illustrated by Fig. 11.8) one by one.

11.5 Conclusions

A divided-compressor was designed for a 30 fs-300 J 10 PW Ti:sapphire laser to compress the 2.7 ns/30 nm deep chirped laser pulse. This design is likely to satisfy the 30 fs-300 J compression requirement. The number and the size of gratings, the cubage of the vacuum compression chamber, and the complexity of the system were optimized.

Acknowledgements This work was supported by the National Natural Science Foundation of China under project 11304296.

References

1. P. Maine, D. Strickland, P. Bado, M. Pessot, G. Mourou, Generation of ultrahigh peak power pulses by chirped pulse amplification. IEEE J. Quantum Electron. **24**, 398 (1988)
2. D. Kramer, J. Novák, B. Rus, Hybrid compressor design for a 10PW laser, in *EPJ Web of Conferences*, vol 48, 00010 (2013)
3. E.B. Treacy, Optical pulse compression with diffraction gratings. IEEE J. Quantum Electron. QE-5, pp. 454 (1969)
4. B.C. Stuart, M.D. Feit, A.M. Rubenchik, B.W. Shore, M.D. Perry, Laser-induced damage in dielectrics with nanosecond to subpicosecond pulses. Phys. Rev. Lett. **74**, 2248 (1995)
5. D.H. Martz, H.T. Nguyen, D. Patel, J.A. Britten, D. Alessi1, E. Krous, Y. Wang, M. ALarotonda, J. George, B. Knollenberg, B.M. Luther, J.J. Rocca, C.S. Menoni, Large area high efficiency broad bandwidth 800 nm dielectric gratings for high energy laser pulse compression. Optics Express **17**, pp 23809 (2009)
6. J. Wang, Y. Jin, J. Ma, T. Sun, X. Jing, Design and analysis of broadband high-efficiency pulse compression gratings. Appl. Opt. **49**, 2969 (2010)
7. Z. Li, G. Xu, T. Wang, Y. Dai, Object-image-grating self-tiling to achieve and maintain stable, near-ideal tiled grating conditions. Opt. Lett. **35**, 2206 (2010)

Chapter 12
Propagation of a Short Subterahertz Pulse in a Plasma Channel in Air Created by Intense UV Femtosecond Laser Pulse

A.V. Bogatskaya, A.M. Popov and E.A. Volkova

Abstract The evolution of the electron energy distribution function in the plasma channel created in air by the third harmonic of the Ti:Sa-laser pulse of femtosecond duration is studied. It is shown that strong nonequilibrium of such a plasma leads to the possibility to use the channel for guiding and amplification of few-cycle electromagnetic pulses in subterahertz frequency range at the time of relaxation of the energy spectrum in air determined by the vibrational excitation of the nitrogen molecules. The refractive index and the gain factor as a function of time, electron concentration and frequency of the amplifying radiation are obtained. The propagation of few-cycle radio-frequency pulses through the amplifying medium is analyzed.

12.1 Introduction

An important feature of the plasma structure appearing in the field of an ultrashort laser pulse is its strong nonequilibrium. Such nonequilibrium can be used for a number of applications, in particular, for generation of XUV attosecond pulses and discussed by Agostini and Di Mauro [1] and Krausz and Ivanov [12]. The energy spectrum of photoelectrons appearing in multiphoton ionization of the gas under the conditions where the pulse duration is comparable or smaller than the average time interval between the electron—atomic collisions consists of a number of peaks corresponding to the absorption of a certain number of photons. Such an electron

---

A.V. Bogatskaya · A.M. Popov (✉)
Department of Physics, Lomonosov Moscow State University, Moscow 119991, Russia
e-mail: alexander.m.popov@gmail.com

A.V. Bogatskaya · A.M. Popov · E.A. Volkova
D.V. Skobeltsyn Institute of Nuclear Physics, Lomonosov Moscow State University,
Moscow 119991, Russia

A.V. Bogatskaya · A.M. Popov
P.N. Lebedev Physical Institute, RAS, Moscow 119991, Russia

P.A. Ribeiro and M. Raposo (eds.), *Photoptics 2014*,
Springer Proceedings in Physics 177, DOI 10.1007/978-3-319-27321-1_12

energy distribution function (EEDF) is characterized by the energy intervals with the inverse population. It was demonstrated by Bunkin et al. [7], that such a situation can be used to amplify electromagnetic radiation in a plasma.

The possibility to use the plasma channel created by a high intensity ultrashort pulse of a KrF excimer laser ($\hbar\Omega = 5\,\mathrm{eV}$) in xenon for the amplification of radio-frequency pulses was analyzed by Bogatskaya and Popov [4]. In this paper time dependences of the gain factor with various frequencies ω of the amplyfied radio-frequency radiation in the xenon plasma channel were obtained. The possibilty to amplify the subterahertz radiation in different gases was studied by Bogatskaya et al. [5]. It was demonstrated that the xenon plasma has some advantages as the amplifying medium in comparison with other rare and molecular gases.

In this paper we discuss the possibility of using of the plasma channel created in the atmospheric air as a waveguide for the transportation and amplification of the radio-frequency radiation. The evolution of the electron energy spectrum in the relaxing plasma created by the femtosecond laser pulse is examined using the Boltzmann kinetic equation and the refactive index as well as the gain factor of electromagnetic radiation in the plasma channel are calculated as a function of time and electronic concentration in dependence of frequency in subterahertz band. It is found that for definite range of the laser frequencies there exists also a rather short time interval when such a relaxing air plasma can be also used as an amplifying and guiding medium for radio-frequency ultrashort pulses. The propagation of such pulses through the amplifying medium is studied in the frames of slow varying amplitude approximation.

It should be mentioned that mechanism of the amplification of electromagnetic radiation in the plasma channel discussed in this paper is close from physical point of view to the effect of the negative absolute conductivity in the low temperature gas-discharge plasma predicted by Rokhlenko [16] and Shizgal and McMahon [17], experimentally detected by Warman et al. [18], and discussed in detail in reviews of Aleksandrov and Napartovich [3] and Dyatko [10].

12.2 Kinetics of Photoelectrons in a Plasma Channel Produced in Air by the Ultrashort UV Laser Pulse

To analyze the properties and evolution of the plasma channel created by a high intensity laser pulse of femtosecond duration, it is significant to take into account that the channel appears only due to the multiphoton ionization of molecules. In this case, the avalanche ionization of the gas molecules can be neglected. Moreover, for pulses with the duration of $\tau_p \sim 100\,\mathrm{fs}$, elastic collisions of electrons with molecules of the medium during the pulse can also be neglected. Indeed, the characteristic time of collisions of electrons with nitrogen or oxygen molecules in air at atmospheric pressure and room temperature ($T \approx 0.03\,\mathrm{eV}$) can be estimated as $T_c \approx 1/N\sigma v$, where $N \approx 2.5 \times 10^{19}\,\mathrm{cm}^{-3}$ is the density of the particles, $\sigma \sim 10^{-15}\,\mathrm{cm}^2$ is the elastic collision cross section, and $v \sim 10^8\,\mathrm{cm/s}$ is the velocity of electrons appearing in the photoionization process. Under these conditions one derives $T_c \sim 4 \times 10^{-13}\,\mathrm{s}$. This time exceeds the duration of the laser pulse. This means that the energy spectrum of photoelectrons by the end of the laser pulse is determined only by the photoionization of molecules of the gas and can be obtained from the solution of the problem of the ionization of a single atom or molecule in a strong laser field. The evolution of the spectrum caused by elastic, inelastic and electron-electron collisions, which is described by the Boltzmann kinetic equation, takes place in the postpulse regime. For this reason, under the conditions of interest, the problem of the ionization of the gas by laser radiation can be considered independently from the problem of the evolution of the spectrum of photoelectrons. The solution of the former problem is used as the initial condition for the latter one.

For the intensity range $I \leq 10^{13}\,\mathrm{W/cm}^2$ the ionization probability of O_2 molecules is a cubic function of the radiation intensity I for the third harmonic of the Ti: Sa laser: $w_i \sim I^3$. For the N_2 molecules we have four-photon ionization in this intensity range: $w_i \sim I^4$. For the moderate fields with the laser intensity of the third harmonic of the Ti:Sa laser $\sim 10^{11}$–10^{12} W/cm^2 in accordance with the perturbation theory the probability of the three-photon ionization is significantly larger than the four-photon ionization probability. So plasma channel is formed mainly by the three-photon ionization of O_2 molecules. Also in such fields the AC Stark shift of both bound levels and the continuum boundary can be neglected. Hence, the position of the first peak in the spectrum of photoelectrons corresponds to the energy $\varepsilon_0 = 3\hbar\Omega - I_i$, where $I_i \approx 12.08\,\mathrm{eV}$ is the ionization potential of the oxygen molecule, and Ω is the frequency of the laser radiation. The data collected by Delone and Krainov [9] and Couairon and Mysyrowicz [8] lead to the estimation of the degree of ionization in air as $\alpha = N_e/N \approx 10^{-7} \div 10^{-6}$ for the above mentioned intensity range and the laser pulse duration $\tau_p \sim 100$ fs. Here N_e is the electron density.

Analyzing the evolution of the energy spectrum, we assume that the plasma channel with a given degree of ionization and strongly nonequilibrium electron energy distribution function is formed at the initial (zero) instant of time. The electron energy distribution function (EEDF) is approximated by the Gaussian

$$n(\varepsilon, t = 0) = \frac{1}{\Delta\varepsilon\sqrt{\pi\varepsilon}} \exp\left(-\frac{(\varepsilon - \varepsilon_0)^2}{(\Delta\varepsilon)^2} \right). \qquad (12.1)$$

The width of the peak is determined by the pulse duration and for $\tau_p \sim 50-100$ fs can be estimated as $\Delta\varepsilon \approx 0.2\,\mathrm{eV}$. For the above mentioned intensity range above-threshold ionization peaks can be neglected.

This electron energy distribution function is normalized as

$$\int_0^\infty n(\varepsilon, t = 0)\sqrt{\varepsilon}\,\mathrm{d}\varepsilon = 1. \tag{12.2}$$

The quantity $n(\varepsilon, t)\sqrt{\varepsilon}$ is the probability density of the existence of the electron with the energy ε.

The temporal evolution of the initial spectrum (12.1) was analyzed using the kinetic Boltzmann equation for the EEDF in the two-term approximation. We also assumed that the radio-frequency field amplifying in the plasma is weak enough and does not contribute to the Boltzmann equation. Under above assumptions the kinetic equation was written in a form:

$$\frac{\partial n(\varepsilon, t)}{\partial t}\sqrt{\varepsilon} = Q_{ee}(n) + Q^*(n) + \sum_i \frac{2m}{M_i}\frac{\partial}{\partial \varepsilon}\left(v_{tr}^{(i)}(\varepsilon)\varepsilon^{3/2}\left(n(\varepsilon, t) + T\frac{\partial n(\varepsilon, t)}{\partial \varepsilon}\right)\right). \tag{12.3}$$

The details can be found in the review of Ginzburg and Gurevich [11], and monograph of Raizer [15].

Equation (12.3) has the form of the diffusion equation in the energy space. Here, T is the gas temperature (below, we take $T \approx 0.03\,\mathrm{eV}$), m is the mass of the electron, M_i (i = 1, 2) are the masses of the nitrogen and oxygen molecules respectively, and $v_{tr}^{(i)} = N_i\sigma_{tr}^{(i)}(\varepsilon)\sqrt{2\varepsilon/m}$ is the partial transport frequency, where $\sigma_{tr}^{(i)}(\varepsilon)$ is the transport scattering cross section for N_2 (i = 1) and O_2 (i = 2) molecules, $N_1 = 0.79 \times N$ and $N_2 = 0.21 \times N$ are the concentrations of N_2 and O_2 molecules in the air, $Q_{ee}(n)$ is the integral of electron-electron collisions, $Q^*(n)$ is the integral of inelastic collisions. These integrals are described in detail in the review of Ginzburg and Gurevich [11].

Equation (12.3) with the initial condition (12.1) was solved numerically using an explicit scheme in the energy range $\varepsilon = 0-5\,\mathrm{eV}$. The elastic and necessary inelastic cross sections for N_2 and O_2 molecules were taken from data obtained by Phelps [14] and Phelps and Pitchford [13]. The total transport cross section for the electrons in air is presented at Fig. 12.1. The most important for our consideration is the existence of the energy interval $\varepsilon = 1.5 \div 2.3\,\mathrm{eV}$ with the positive derivative $\mathrm{d}\sigma_{tr}/\mathrm{d}\varepsilon > 0$.

Among a lot of inelastic collisions of electrons with nitrogen and oxygen molecules the excitation of vibrational levels of the ground electronic state $N_2(X^1\Sigma^+)$ is of most importance. These cross sections are high enough in the energy range ~2–4 eV and contribute significantly to the temporal evolution of the EEDF discussed below.

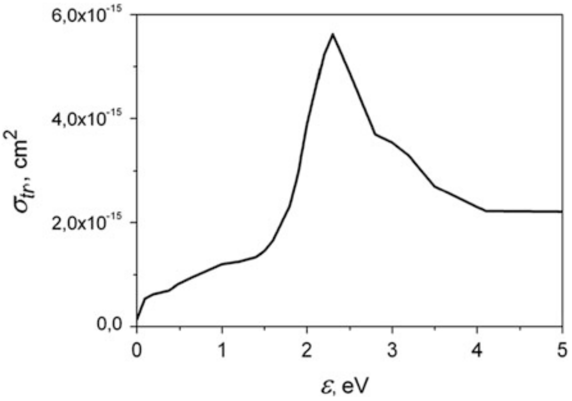

Fig. 12.1 Transport cross section for the electrons in air

The obtained from (12.3) EEDF makes it possible to calculate the temporal dependence of the electrodynamic properties of the plasma channel created by laser pulse. For example, the expression for the complex conductivity $\sigma(\omega) = \sigma'(\omega) + i\sigma''(\omega)$ at the frequency ω can be written in the form (for details see the reviews of Ginzburg and Gurevich [11] and Bunkin et al. [7]):

$$\sigma(\omega) = \frac{2}{3}\frac{e^2 N_e}{m}\int\limits_0^\infty \frac{\varepsilon^{3/2}(\nu_{tr}(\varepsilon) + i\omega)}{\omega^2 + \nu_{tr}^2(\varepsilon)}\left(-\frac{\partial n(\varepsilon, t)}{\partial \varepsilon}\right)\mathrm{d}\varepsilon. \tag{12.4}$$

The real part of this expression describes the dissipation of the energy of the electromagnetic wave in the plasma. For weakly ionized plasma the absorption coefficient at the frequency ω can be represented in the form:

$$\mu_\omega = \frac{4\pi\sigma'}{c} = \frac{2}{3}\frac{\omega_p^2}{c}\int\limits_0^\infty \frac{\varepsilon^{3/2}\nu_{tr}(\varepsilon)}{\omega^2 + \nu_{tr}^2(\varepsilon)}\left(-\frac{\partial n(\varepsilon, t)}{\partial \varepsilon}\right)\mathrm{d}\varepsilon, \tag{12.5}$$

where $\omega_p^2 = 4\pi e^2 N_e/m$ is the squared plasma frequency.

The imaginary part of the expression (12.4) determines the plasma refractive properties. The refractive index of the weakly ionized plasma can be written in a form:

$$n_\omega = 1 - \frac{2\pi\sigma''}{\omega} = 1 - \frac{1}{3}\omega_p^2\int\limits_0^\infty \frac{\varepsilon^{3/2}}{\omega^2 + \nu_{tr}^2(\varepsilon)}\left(-\frac{\partial n(\varepsilon, t)}{\partial \varepsilon}\right)\mathrm{d}\varepsilon. \tag{12.6}$$

In the case when $\nu_{tr}(\varepsilon) = const$ for any expression for the EEDF we derive well-known formulas (see, for example, the monograph of Raizer [15]) for refractive index and absorption coefficient in the weakly ionized plasma:

$$n_\omega = 1 - \frac{1}{2}\frac{\omega_p^2}{\omega^2 + \nu_{tr}^2}, \quad \mu_\omega = \frac{\omega_p^2 \nu_{tr}}{c(\omega^2 + \nu_{tr}^2)} \tag{12.7}$$

In particular, we note that the refractive index $n_\omega < 1$, i.e. plasma is optically less dense medium than the neutral gas.

In more general case when transport frequency is the function of the electron energy the refractive index and the absorption coefficient depends on the specific form of the electron energy distribution function. Typically EEDF decreases with the energy, i.e. $\partial n/\partial\varepsilon < 0$ and, consequently, both integrals in (12.5) and (12.6) are positive and, hence, $n_\omega < 1$, i.e. plasma remains to be optically less dense medium, and $\mu_\omega > 0$. However, in the process of the photoionization of atoms or molecules by short pulses, energy ranges with the positive derivative, $\partial n/\partial\varepsilon > 0$, appear to exist for the initial instant of time. Such energy intervals make a negative contribution to the integrals in (12.5) and (12.6). In particular, it was demonstrated by Bunkin et al. [7] that the integral in (12.5) can become even negative in the low-frequency range $\omega < \nu_{tr}$ in gases with the pronounced Ramsauer minimum for the EEDF with energy interval with positive derivative, $\partial n/\partial\varepsilon > 0$. In the papers of Bunkin et al. [7] and Bogatskaya et al. [5] it was found that for the plasma with the EEDF similar to (12.1) the amplification of the electromagnetic radiation with $\omega < \nu_{tr}$ will be possible, if the condition

$$\frac{\mathrm{d}}{\mathrm{d}\varepsilon}\varepsilon/\sigma_{tr}(\varepsilon) < 0 \tag{12.8}$$

is fulfilled. Typically, the condition $\omega < \nu_{tr}$ is satisfied for the subterahertz frequency range $\omega \leq 10^{12}\,\mathrm{s}^{-1}$. As about change the sign of the integral (12.6) for the EEDF defined by (12.1) it will take place for the gases with

$$\frac{\mathrm{d}}{\mathrm{d}\varepsilon}\varepsilon^{1/4}\Big/\sigma_{tr}(\varepsilon) < 0 \tag{12.9}$$

This inequality is much more soft and is performed for many gases.

Bogatskaya and Popov [4] demonstrated that the presence of the Ramsauer minimum in the transport cross section of xenon and as a consequence the rapidly increasing range of the $\sigma_{tr}(\varepsilon)$ can be responsible for the appearance of the amplification of electromagnetic radiation in the plasma created by multiphoton ionization by short laser pulse. Both N_2 and O_2 molecules do not characterized by the Ramsauer minimum. Nevertheless, the transport cross section for electron scattering on nitrogen molecule is characterized by large positive value of the derivative $\mathrm{d}\sigma_{tr}/\mathrm{d}\varepsilon$ in the energy range of ~1.5–2.3 eV. As a result, the condition (12.8) is

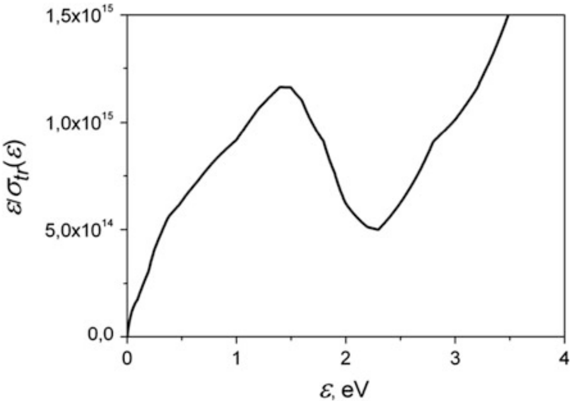

Fig. 12.2 The value $\varepsilon/\sigma_{tr}(\varepsilon)$ for electrons in air

satisfied in this range (see Fig. 12.2). It means that it is also possible to obtain the negative values of the absorption coefficient.

We would like to stress, that for the case under study integral in (12.6) can also become negative. It means, that the refractive index for such strongly nonequlibrium plasma will be greater than unity, $n_\omega > 1$ and plasma will become optically more dense medium than the nonionized gas. Thus, such a plasma channel can be considered as waveguide for both transportation and amplification of microwave radiation.

Results of the numerical simulations for the EEDF evolution in time in air are presented at Figs. 12.3 and 12.4 for two different energy positions of the initial photoelectron peak. As can be seen, for the initial energy of photoelectrons $\varepsilon_0 = 1.8\,\text{eV}$ (this energy value is very close to the ionization of oxygen molecules by the third harmonic of the Ti:Sa laser) the electron energy distribution function is characterized by pronounced maximum, which is gradually shifted toward lower

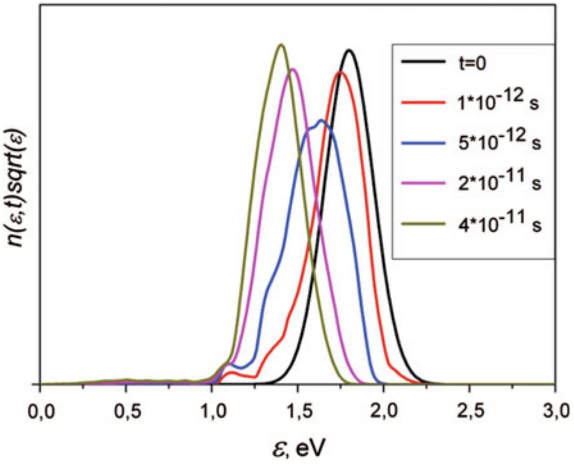

Fig. 12.3 The EEDF in air at various times after the creation of the plasma channel. Initial peak of photoelectrons is characterized by $\varepsilon_0 = 1.8\,\text{eV}$ and electron concentration $N_e = 10^{13}\ \text{cm}^{-3}$

Fig. 12.4 The EEDF in air at various times after the creation of the plasma channel. Initial peak of photoelectrons is characterized by $\varepsilon_0 = 2.2$ eV and electron concentration $N_e = 10^{13}$ cm^{-3}

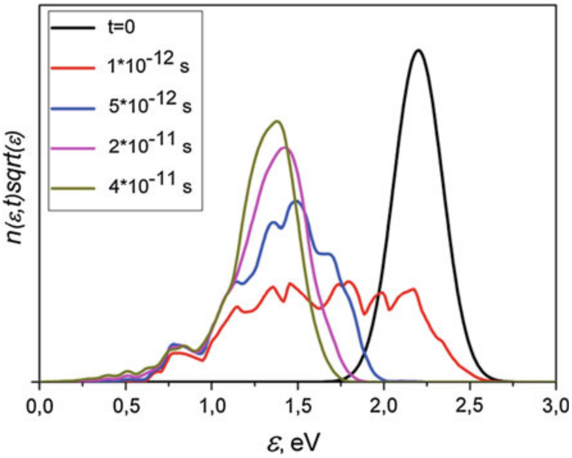

energies. While the average electron energy is more then ~1.5 eV (see the dependence at Fig. 12.2), it is naturally to expect the positive value of the gain factor. It should be emphasized that for larger energy of the initial photoelectrons $(\varepsilon_0 = 2.2\,\text{eV})$ the temporal evolution of the EEDF is quite different from that was discussed above (see Fig. 12.4). Due to significant value of the cross sections for the vibrational excitation of N_2 molecules by electrons with energies above ~2.0 eV the characteristic time of relaxation of the EEDF for $\varepsilon_0 = 2.2\,\text{eV}$ decreases dramatically and photoelectrons are found to be distributed over the energy range of $1.0{-}2.2\,\text{eV}$ even for the $t = 1$ ps. Later the Gaussian-type EEDF is formed again, but the average energy of photoelectrons for these instants of time is less 1.5 eV, and the positive value of the gain factor can not be achieved.

The electron energy distribution functions obtained in the numerical simulations were used to calculate the gain factor of electromagnetic radiation $(k_\omega = -\mu_\omega)$ in the air plasma for different values of the initial peak position and the frequency of the amplified radiation $\omega = 5 \times 10^{11}\,\text{s}^{-1}$. These data are presented at Fig. 12.5.

Fig. 12.5 Time dependence of the gain factor of the electromagnetic radiation with frequency 0.5 THz in the atmospheric air plasma channel for different energies of the photoionization peak

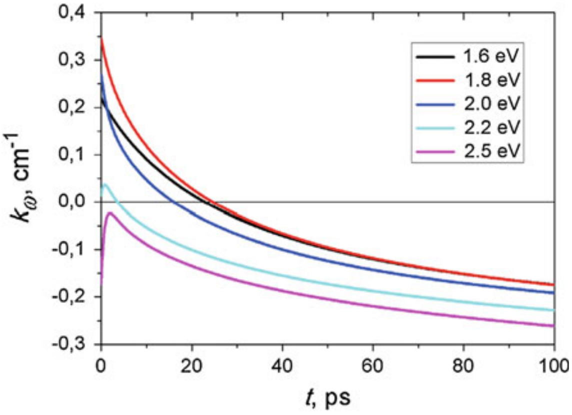

The data presented clearly demonstrate that the amplification of the radiation is possible if the energy of photoelectrons is less than ~ 2.25 eV. On the other hand, the energy of the initial photoelectron peak should not be less than 1.5 eV. The maximum value of the gain factor can be obtained for the initial photoelectron peak position $\varepsilon_0 = 1.8\,\text{eV}$.

Such energy of photoelectrons appears to exist for the three-photon ionization by the laser radiation with $\hbar\Omega \approx 4.63\,\text{eV}$ which is very close to the third harmonics of the Ti:Sa laser. Even for such value of ε_0 the gain factor is found to be positive during approximately 25 ps. It means that the plasma channel in air can be used for amplification of only extremely short few-cycled radio-frequency pulses. For example, for $\omega = 5 \times 10^{11}\,\text{s}^{-1}$ it is possible to amplify the pulses of two or three cycle duration. For higher frequencies of amplified radiation the gain factor drops dramatically as the condition $\omega < \nu_{tr}$ is not satisfied already.

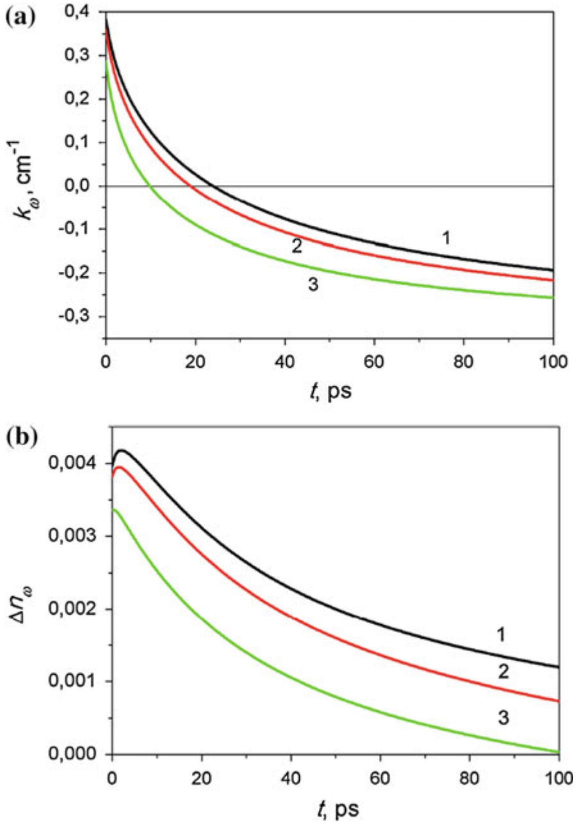

Fig. 12.6 Time dependencies of the gain factor (**a**) and refractive index (**b**) for the RF radiation with frequencies (THz) 0.2 (1), 0.5 (2), 1 (3) in the plasma channel for the initial photoelectron peak position $\varepsilon_0 = 1.8$ eV. Electron concentration $N_e = 10^{13}\ \text{cm}^{-3}$

The results of simulation for gain factors and refractive indexes $\Delta n_{\omega} = n_{\omega} - 1$ for initial peak position at 1.8 eV and for different frequencies of the radio-frequency (RF) field are presented at Fig. 12.6. It can be seen that increasing of the RF frequency results in shortening of the time interval can be used for guiding and amplification of the microwave radiation. On the other hand for microwave field frequencies up to 10^{12} W/cm^2 the time interval for positive value of $\Delta n_{\omega} = n_{\omega} - 1$ is several times larger than the interval for positive gain factor.

12.3 Propagation and Amplification of the Radio-Frequency Pulses in the Plasma Waveguide

As it is known, propagation of the electromagnetic radiation in the medium is described by the wave equation:

$$\nabla^2 \vec{E} - \frac{1}{c^2}\frac{\partial^2 \vec{E}}{\partial t^2} = \frac{4\pi}{c^2}\frac{\partial \vec{j}}{\partial t}. \tag{12.10}$$

Here $\vec{E}$ is the electric field strength, $\vec{j}$ is the density of the electric current in the plasma.

To analyze the process of microwave pulse propagation qualitatively we use the optical parabolic approximation for the solution of (12.10) (for details see the monograph of Akhmanov and Nikitin [2]). According to this approximation for the pulse propagation along z-direction E should be represented as

$$\vec{E}(\vec{r}, t) = \vec{E}_0(\rho, z, t) \cdot \exp(i(kz - \omega t)) \tag{12.11}$$

Here E_0 is the envelope of the radio-frequency pulse, and $k = \omega / c$ is the wave number.

If we neglect the temporal dispersion, the expression for $\vec{j}$ can be written in a form $\vec{j} = \sigma \vec{E}$. Here σ is the conductivity determined by expression (12.4). In this paper we assume that the radio-frequency pulse is linearly polarized and its intensity is weak enough and do not contribute to the temporal evolution of the EEDF in the plasma channel. As the electronic density in the plasma channel is low enough, the refractive index at the frequency $\omega = 5 \times 10^{11}$ s^{-1} is close to unity and it is possible to assume that the radio-frequency pulse propagates in the channel with the speed of light. After some approximations one can obtain the folowing equation for the E_0:

$$ik\left(\frac{\partial E_0}{\partial z} + \frac{1}{c}\frac{\partial E_0}{\partial t}\right) = -\frac{1}{2}\nabla_{\perp}^2 E_0 - \Delta n_{\omega}(t - z/c)k^2 E_0 + \frac{i}{2}k_{\omega}(t - z/c)kE_0 \tag{12.12}$$

The first term in the right part in (12.12) stands for the diffraction divergence of the electromagnetic field, the second one describes the plasma focusing (defocusing) features and the third term represents the absorption (amplification) process. Actually, the amplification duration τ corresponds to the amplification distance of about $c \cdot \tau \sim 1$ cm. So the laser pulse creates the air plasma channel characterized by amplifying «trail» (see Fig. 12.7). If we launch the laser pulse and the few-cycled RF pulse just one after another simultaneously, the last one will continually locate in the amplifying zone of the laser pulse.

It can be seen from (12.12) that in the case $n_\omega > 1$ the plasma channel will partly suppress the diffration divergence of the RF radiation. If the condition

$$(n_\omega - 1)k^2R^2 > 1 \tag{12.13}$$

(here R is the plasma channel radius) is satisfied the channel looks like the waveguide and can transport the radiation without divergence. For $\omega = 5 \times 10^{11}\,\mathrm{s}^{-1}$ and $k = \omega/c \approx 16.7\,\mathrm{cm}^{-1}$ and $\Delta n_\omega \sim 0.0035$ (see Fig. 12.6) the guiding regime of propagation will be realized for $R > 1$ cm.

For the guiding regime of the RF pulse propagation corresponding to the compensation of the divergence term in (12.12) by focusing term the (12.12) can be rewritten in a form

$$\frac{\partial E_0(z,\tau)}{\partial z} = \frac{1}{2}k_\omega(\tau)E_0(z,\tau), \tag{12.14}$$

where the new retardation time is introduced: $\tau = t - z/c$. From (12.14) one obtains:

$$E_0(z,t) = \Phi(t - z/c)\exp\left(\frac{1}{2}k_\omega(t - z/c)z\right). \tag{12.15}$$

Fig. 12.7 Spatial structure of radio (*1*) and laser (*2*) pulses for a given instant of time. *Dash curves* are the spatial profiles of the gain factor and refractive index

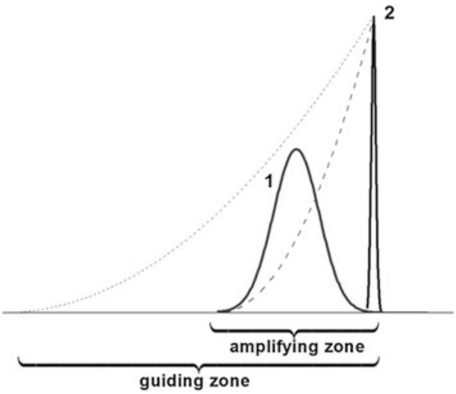

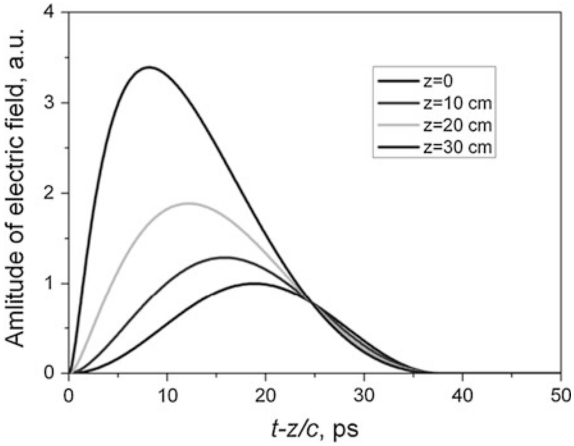

Fig. 12.8 Time dependence of the electric field strength in the amplifying pulse for different propagation lengths

Here Φ is the initial envelope of the RF pulse. We assume that it has the Gaussian form and temporal duration of three optical cycles. Figure 12.8 shows that the significant increase of the radio-frequency pulse amplitude can be obtained during its propagation despite the short time of amplification.

To conclude the discussion of radio frequency pulse guiding and amplification in a plasma channel we would like to stress that (12.12) and (12.14) are obtained in the optical parabolic approximation. It was demonstrated by Brabec and Krausz [6] that this approximation can be applied for the propagation of the pulse of few duration cycles only qualitatively.

12.4 Conclusions

In this paper it has been shown that a plasma channel created in the atmospheric air by the third harmonic of the Ti:Sa laser can be used for amplification and guiding of few-cycle electromagnetic pulses in subterahertz frequency range. Despite the short time duration of the positive gain factor there is an opportunity to reach significant amplification by the simultaneous launching of the laser and few-cycle RF pulses with approximately the same propagation velocity.

Acknowledgements This work was supported by the Russian Foundation for Basic Research (project no. 15-02-00373). Numerical modeling was performed on the SKIF-MSU Chebyshev supercomputer.

References

1. P. Agostini, L.F. Di Mauro, Rep. Prog. Phys. **67**, 813–855 (2004)
2. S.A. Akhmanov, S.Y. Nikitin, *Physical Optics* (Oxford, 1997)
3. N.L. Aleksandrov, A.P. Napartovich, Phys. Usp. **36**, 107–128 (1993)
4. A.V. Bogatskaya, A.M. Popov, JETP Lett. **97**, 388–392 (2013)
5. A.V. Bogatskaya, E.A. Volkova, A.M. Popov, Quantum Electron. **43**, 1110–1117 (2013)
6. Th Brabec, F. Krausz, Phys. Rev. Lett. **78**, 3282–3285 (1997)
7. F.V. Bunkin, A.A. Kazakov, M.V. Fedorov, Sov. Phys. Usp. **15**, 416–435 (1972)
8. A. Couairon, A. Mysyrowicz, Phys. Rep. **441**, 47–189 (2007)
9. N.B. Delone, V.P. Krainov, *Multiphoton processes in atoms* (Springer, Berlin, 1994)
10. N.A. Dyatko, J. Phys. Conf. Ser. **71**, 012005 (14 pp) (2007)
11. V.L. Ginzburg, A.V. Gurevich, Sov. Phys. Usp. **3**, 115–146 (1960)
12. F. Krausz, M. Ivanov, Rev. Mod. Phys. **81**, 163–234 (2009)
13. A.V. Phelps, L.C. Pitchford, Phys. Rev. A **31**, 2932–2949 (1985)
14. A.V. Phelps, JILA Information Center Report No. 26. University of Colorado (1985)
15. Y.P. Raizer, *Laser—Induced Discharge Phenomena* (Consultants Bureau, New York, 1977)
16. A.V. Rokhlenko, Sov. Phys. JETP **48**, 663–665 (1978)
17. S. Shizgal, D.R.A. McMahon, Phys. Rev. A **32**, 3669–3680 (1985)
18. J.M. Warman, U. Sowada, M.P. de Haas, Phys. Rev. A **31**, 1974–1976 (1985)

Author Index

P.A. Ribeiro and M. Raposo (eds.), *Photoptics 2014*,
Springer Proceedings in Physics 177, DOI 10.1007/978-3-319-27321-1

Subject Index

P.A. Ribeiro and M. Raposo (eds.), *Photoptics 2014*,
Springer Proceedings in Physics 177, DOI 10.1007/978-3-319-27321-1